DEVELOPMENT OF AN INTEGRATED LAB-ON-A-CHIP (LOC) PLATFORM FOR MULTIDRUG EFFECT ANALYSIS

A THESIS SUBMITTED TO
THE GRADUATE SCHOOL OF NATURAL AND APPLIED SCIENCES
OF
MIDDLE EAST TECHNICAL UNIVERSITY

BY

ALİ CAN ATİK

IN PARTIAL FULFILLMENT OF THE REQUIREMENTS
FOR
THE DEGREE OF MASTER OF SCIENCE
IN
ELECTRICAL AND ELECTRONICS ENGINEERING

JANUARY 2019

Approval of the thesis:

DEVELOPMENT OF AN INTEGRATED LAB-ON-A-CHIP (LOC) PLATFORM FOR MULTIDRUG EFFECT ANALYSIS

submitted by **ALİ CAN ATİK** in partial fulfillment of the requirements for the degree of **Master of Science in Electrical and Electronics Engineering Department, Middle East Technical University** by,

Prof. Dr. Halil Kalıpçılar
Dean, Graduate School of **Natural and Applied Sciences** _____

Prof. Dr. Tolga Çiloğlu
Head of Department, **Electrical and Electronics Eng.** _____

Prof. Dr. Haluk Külah
Supervisor, **Electrical and Electronics Eng., METU** _____

Assoc. Prof. Dr. Ender Yıldırım
Co-Supervisor, **Mechanical Eng., Çankaya University** _____

Examining Committee Members:

Prof. Dr. Tayfun Akın
Electrical and Electronics Eng., METU _____

Prof. Dr. Haluk Külah
Electrical and Electronics Eng., METU _____

Prof. Dr. Nevzat Güneri Gençer
Electrical and Electronics Eng., METU _____

Assoc. Prof. Dr. Yeşim Serinağaoğlu Doğrusöz
Electrical and Electronics Eng., METU _____

Assoc. Prof. Dr. Ender Yıldırım
Mechanical Eng., Çankaya University _____

Date: 16.01.2019

I hereby declare that all information in this document has been obtained and presented in accordance with academic rules and ethical conduct. I also declare that, as required by these rules and conduct, I have fully cited and referenced all material and results that are not original to this work.

Name, Surname: Ali Can Atik

Signature:

ABSTRACT

DEVELOPMENT OF AN INTEGRATED LAB-ON-A-CHIP (LOC) PLATFORM FOR MULTIDRUG EFFECT ANALYSIS

Atik, Ali Can
Master of Science, Electrical and Electronics Engineering
Supervisor: Prof. Dr. Haluk Külah
Co-Supervisor: Assoc. Prof. Dr. Ender Yıldırım

January 2019, 158 pages

This thesis presents analysis, design, fabrication, and testing of microfluidic sub-units designed for a droplet-based multidrug analysis platform. The platform is integrated with normally closed electrostatically actuated microvalves to monitor cytotoxicity of anticancer drugs on single cancer cells encapsulated in microdroplets.

Here, elucidation of cancer heterogeneity requires precise functional analysis at single-cell levels which can assist to select effective drug regimens for personalized chemotherapy. One preeminent technique is to utilize droplet microfluidics which enable encapsulation of single cell in its isolated immediate environment in a high-throughput manner and allow to carry out cell-based assays in tiny volumes.

The lab-on-a-chip platform is designed to observe the effect of different combinations and dosages of chemotherapeutic agents on K562 leukemia cells and includes mixing, cell focusing, droplet formation and in vitro cytotoxicity screening all in a single chip. Integrated electrostatic microvalves permit the control of drug flow and routing of droplets within microfluidic device.

A review of theoretical concepts, corresponding Computational Fluid Dynamics (CFD) simulations and test results are presented separately for microfluidic sub-

systems: passive micromixer, droplet formation in a flow-focusing junction, inertial microfluidics for cell focusing. Then, they combined to compose a full droplet screening workflow. Evaluating both experimental results and numerical simulations regarding the contraction-expansion type micromixer structure indicates that it is possible to achieve a mixing efficiency over 80% for sample flows with a wide range of Reynolds numbers. Droplet size distribution controlled by the volumetric flow rates of dispersed and continuous phases is obtained both numerically and experimentally and the studies validate that droplets with an effective size around 50 μm can be generated by adjusting the flow rates of both phases at a high generation rate (>1000 kHz). Moreover, it is shown that the passive micromixer enhances the single-cell encapsulation ratio to a certain degree (up to %42) by hydrodynamically focusing the cells to the middle of the microchannel. The effectivity of doxorubicin on K-562 leukemia cancer cells confined in drug-media drops is measured at single-cell level based on the fluorescence intensity change over 2 hours and compared with a control group which is not exposed to the drug.

While modeling the electrostatically actuated microvalve, both analytical models and Finite Element Analysis (FEM) analysis regarding pull-in voltages and displacements are included. Fabricated prototypes are tested to characterize microvalve behavior for pull-in voltage, repeatability, response times and touch area during actuation. Pull-in voltage is measured around 122 ± 10.65 V. The experimental value of pull-in voltage is closely consistent with numerical and analytical studies. Response times for both opening and closing states observed between 1-3 seconds for different valves. Moreover, fabricated moving diaphragms which are sealed with PDMS microchannels are tested under flow to prove that the proposed channel integration allows fluid flow underneath the valve seat when the valve is actuated.

Keywords: Passive Micromixer, Droplet Microfluidics, Inertial Microfluidics, Microvalves, Electrostatic Actuation, BioMEMS

ÖZ

ÇOKLU İLAÇ ETKİSİ ANALİZİ İÇİN ENTEGRE BİR ÇİP ÜSTÜ LABORATUVAR PLATFORMUNUN GELİŞTİRİLMESİ

Atik, Ali Can
Yüksek Lisans, Elektrik ve Elektronik Mühendisliği
Tez Danışmanı: Prof. Dr. Haluk Külah
Ortak Tez Danışmanı: Doç. Dr. Ender Yıldırım

Ocak 2019, 158 sayfa

Bu tezde, tekil kanser hücreleri üzerindeki kemoterapi ilaçların sitotoksisitesini izlemek için normalde kapalı elektrostatik mikrovalfler ile entegre edilmiş, damlacık tabanlı çoklu ilaç analiz platformunun alt ünitelerinin analizi, tasarımı, üretimi ve testi sunulmaktadır.

Daha etkili ve kişiselleştirilmiş bir kemoterapi için, bir hastanın cevap vereceği uygun ilaç dozajının değerlendirilebileceği hücre canlılık oranını izleyen canlı dışı kemosensitivite deneyleri gereklidir. Kanser heterojenliğinin ortaya çıkarılması, tekil hücreler üzerinde hassas bir fonksiyonel analiz gerektirir; fakat, bir hasta için etkili olacak ilaç rejimlerinin seçilmesinde yardımcı olabilir. Bu konuda, en önemli tekniklerden biri, tekil hücrenin izole edilmiş ortamda, yüksek verimli bir şekilde kapsüllenmesini sağlayan ve küçük hacimlerde analizlerin gerçekleştirilmesine olanak tanıyan mikroakışkan damlacıkların kullanılmasıdır.

Sunulan çip üzerinde laboratuvar platformu, hücreler üzerinde kemoterapötik ajanların farklı kombinasyonlar ve dozajlarda etkisini gözlemlemek üzere tasarlanmıştır ve tek bir çip üzerinde karıştırma, hücre odaklama, damlacık oluşumu ve canlı dışı sitotoksisite taramasını içerir. Entegre elektrostatik mikrovalfler, ilaç

akışının kontrolüne ve damlacıkların mikroakışkan cihaz içinde yönlendirilmesine izin verir.

İlgili teorik kavramlar, CFD simülasyonları ve test sonuçları mikroakışkan yapının alt sistemleri olan pasif mikrokarıştırıcı, akış odaklayıcıda damlacık oluşumu ve hidrodinamik hücre odaklayıcı için ayrı olarak sunulmuştur. Mikrokarıştırıcı yapısına ilişkin simülasyonlar ve deneysel sonuçlar, geniş bir Reynolds sayısı aralığındaki numune akışları için %80'in üzerinde bir karışım verimliliği elde etmenin mümkün olabileceğini göstermektedir. Dağınık ve sürekli fazların akış hızlarına göre damlacık büyüklüğü dağılımının elde edilmesine yönelik simülasyonlar ve deneysel çalışmalar, 50 μm çapında damlacıkların yüksek bir üretim hızında (>1000 kHz) elde edilebileceğini göstermiştir. Ayrıca, pasif mikrokarıştırıcının hücreleri mikrokanalın ortasına hidrodinamik olarak odaklayarak, tek hücre hapsetme başarımını (%42'ye kadar) arttırdığı gösterilmiştir. Doksorubisinin damlacık içine hapsolmuş K-562 lösemi kanser hücreleri üzerindeki etkisi, 2 saat boyunca floresan yoğunluğu değişimi gözlemlenerek ölçülmüş ve ilaca maruz kalmayan bir kontrol grubu ile karşılaştırılmıştır.

Elektrostatik mikrovalfin modellenmesinde, bükülme miktarını ve çekme voltajını belirlemek için analitik modeller ve FEM analizi kullanılmıştır. Üretilen mikrovalf prototipleri çekme gerilimi ve tepki verme süresini karakterize etmek için test edilmiştir. Çekme gerilimi, 300 μm diyafram yarıçapı için 122 ± 10,65 V civarında ölçülmüştür. Çekme geriliminin deneysel olarak elde edilen değeri, sayısal ve analitik çalışmalarla tutarlıdır. Hem açılış hem de kapanma durumlarında tepki süreleri, farklı valfler için 1-3 saniye arasında olduğu gözlemlenmiştir. Ayrıca, PDMS mikrokanallar ile kapatılan diyaframlar, önerilen kanal entegrasyonunun, mikrovalf çalıştırıldığında, sıvı akışına izin verdiğini kanıtlamak üzere akış altında test edilmiştir.

Anahtar Sözcükler: Pasif Mikrokarıştırıcı, Damlacık Mikroakışkanları, Ataletsel Mikroakışkan Dinamiği, Mikrovalf, Elektrostatik Tahrik, BioMEMS

To my precious parents, and sister

ACKNOWLEDGEMENTS

I would like to express my deepest gratitude to my supervisor Prof. Dr. Haluk Külah for the support and guidance he gave me during my graduate study and also for giving me the opportunity to work on an exciting project. I am also grateful to my co-advisor Assoc. Prof. Ender Yıldırım for his valuable guidance, comments, support, and insightful perspective. For her invaluable remarks, opinions and motivations, I would like to thank to Assoc. Prof. Ebru Özgür. I would also like to thank Prof. Dr. Tayfun Akın for maintaining our METU-MEMS Center.

I especially thank my project partners Metin Dündar Özkan and Maryam Parsiyan for the valuable times to work with them and for their help in any respect. It was truly fun to have enjoyable times in daily life and at work and brainstorming with Metin and Maryam. I would like to also thank all members of BioMEMS research group for their collaborations and supports, but most importantly for their friendship. Moreover, I am indebted especially to Taylan Berkin Töral, Orhan Akar and all METU MEMS staff for sharing their knowledge on microfabrication, and for their help and support in the cleanroom.

I would like to, most importantly, express sincerest gratitude to my parents Şehnaz and Arif Atik and my sister Merve not only for keeping their unfailing support and continuous encouragement in the duration of this thesis but also for their love, motivation, faith, and advice during my entire life. By the way, I am deeply grateful to all my friends, especially to Günce Uzgören and my cousin Funda Atik, for being always there for me.

Moreover, I gratefully acknowledge the Scientific and Technological Research Council of Turkey (TÜBİTAK) for the financial support on the project with the grant number 114E098 and also for my graduate scholarship through BİDEB 2210-A programme.

TABLE OF CONTENTS

LIST OF TABLES

TABLES

LIST OF FIGURES

FIGURES

CHAPTER 1

INTRODUCTION

The microfluidic technology, also known as Lab-on-a-Chip (LOC), or Micro-Total-Analysis Systems (μTAS), has gradually advanced over the recent decades and became a major tool of research for biological and chemical analysis. Particularly for cell biology, this technology might supersede the conventional laboratory methods using well-plates and microscopy slides to monitor and analyze cell population behavior due to its considerable merits.

LOC devices provide several considerable and revolutionary advantages over traditional methods. For instance, miniaturization reduces required sample amount considerably so saves reagent cost and prevents unnecessary consumption which expands the use of rare samples such as stem cells, circulating tumor cells or biopsies. Additionally, LOC systems provide portability rendering point-of-care analysis possible and disposability avoiding cross-contamination, and automation of systems might diminish the errors due to active human involvement, and the need for trained personals. At microscale, due to the increase in the surface per volume ratio, faster molecular diffusion and heat transport permit considerable gain in throughput for biochemical reactions or DNA amplification using polymerase chain reaction (PCR) involving thermal cycling. Most importantly, LOC technology provides more biological relevance mainly because of its high resolution and sensitivity. Moreover, it provides completely novel and revolutionary applications and analysis methods such as single-cell analysis.

The fabrication of LOC devices mostly necessitates cleanroom facilities and specific equipment. A vast number of fabrication techniques and materials are applicable for manufacturing quite sophisticated microstructures with integrated modules. Several

microfluidic units such as micropumps, microvalves, micromixers, and other functional constituents that can assist the functionality of the chip have been miniaturized. Likewise, sensors, detectors, or even optical units can be fully integrated on the same chip.

Here, LOC systems are seen as a promising method for applications involving analysis of drug-cell interactions. Microfluidic systems can fulfill the demand of high-throughput experimentation, so can enhance or might ultimately supersede present technologies aiming essential issues of drug discovery such as synthesis and screening of drug molecules, and preclinical drug trials [1]. In traditional bulk techniques, the drug-cell interaction is observed by presenting a particular drug on a cell culture at certain concentrations. In this case, an average data about the cell population can be obtained, but information about the individual behavior of the cells is lost. However, awareness of cellular heterogeneity can yield new insights into current progress in cancer research. Essentially, the proper interpretation of individual cell behavior necessities quantitative analysis at single-cell levels. Figure 1.1 shows the differences between ensemble analysis of cell population and single-cell analysis.

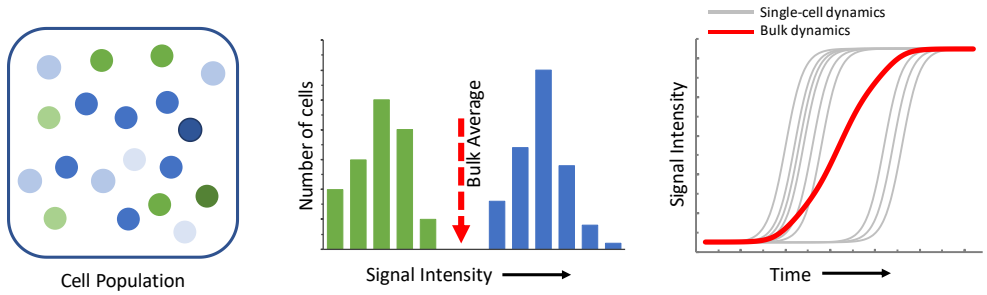

Figure 1.1. Schematic illustrations of the differences between conventional bulk and single cell analysis of cells.

For single cell analysis, LOC systems provides several microfluidic manipulation techniques for trapping and isolation of individual cells, including hydrodynamic methods [2]–[6], dielectrophoretic trapping [7]–[9], magnetic trapping [10]–[13], acoustic trapping [14], optical tweezers [15]–[18], microwells [19], [20], or droplet-based microfluidics [21]–[25]. Particularly, among these methods, hydrodynamic

methods and droplet-based methods offer capturing a high number of single-cells per unit time. In the method of hydrodynamic trapping, cells are captured by physical trapping structures placed in the microchannel and single-cell analysis such as drug toxicity are performed in these chambers. However, cross-contamination may engender misleading inferences regarding single-cell response because all are in the same medium. Here, utilization of droplet microfluidics enables encapsulation of single cell in its isolated immediate environment in a high-throughput manner and allow to carry out cell-based assays by consuming small volumes. Thus, droplet-based single cell-drug interaction systems are widely preferred, mainly because they allow miniaturization, compartmentalization, monodisperse and high-throughput generation in short amount of time. The need for high-throughput is particularly important in diseases such as cancer, where appropriate treatment is required in the shortest possible time.

1.1. Motivation

Cancer means uncontrolled proliferation of genetically altered cells. The current knowledge on cancer points out that different type of mutations in the same population engender heterogeneous behavior of cells; thus, consequently, this may induce drug resistance or relapse of the disease. As illustrated in Figure 1.2, cancer heterogeneity may arise at multiple levels which vary between different patients, between primary and metastatic tumors in a single patient, and between the individual cells of a single tumor [26].

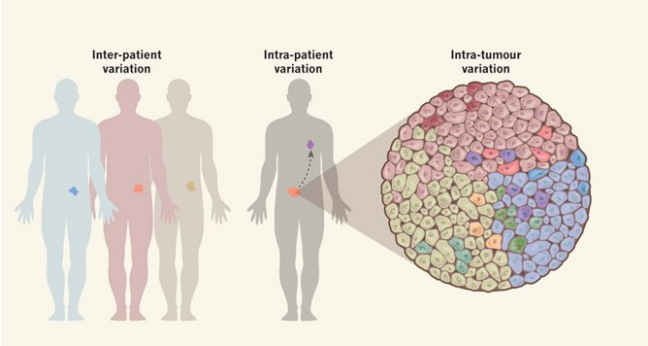

Figure 1.2. Multiple levels of cancer genetic heterogeneity [26].

Here, proper interpretation of heterogeneity at personal level is particularly significant for exposing personalized therapies which may induce less damage to healthy cells and lesser side effects by preventing unnecessary amount of drug doses. Consequently, the personalized therapy may increase the effectiveness of the treatment and potentially enhance life quality of patients during therapy. Figure 1.3 shows a schematic comparison of conventional and personalized cancer therapies.

The individualized therapy necessities in vitro drug tests to forecast the responsiveness to specific treatment. Existing technology to assess the effect of drugs is limited because conventional bulky assays exhibit an average response of thousands of cells by omitting heterogeneity. A droplet-based single-cell encapsulation can yield high quality information regarding individual cell responses to a specific drug.

For the treatment of cancer, often more than one drug is used at the same time. Therefore, a drug analysis system should be able to yield reliable quantitative information pertinent to cytotoxicity of different drug combinations simultaneously to decide an appropriate combinatorial drug therapy. This can be achieved by the addition of microvalves to the single-cell analysis system in order to control drug flow.

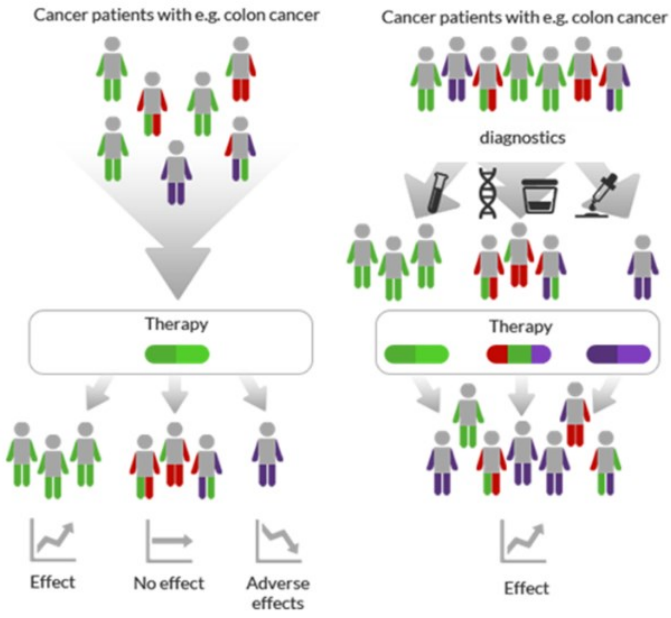

Figure 1.3. Personalized chemotherapy [27].

1.2. Objective of the Thesis

The aim of the thesis is development, implementation, and testing of microfluidic sub-units of a droplet based, integrated, high throughput, on-chip, multi-drug analysis system. These sub-units include a passive micromixer to facilitate the mixing of drugs and cell suspension, a flow-focusing microchannel to achieve high-throughput droplet formation confining individual cells to isolated tiny drug compartments, inertial ordering of cells to enhance single-cell encapsulation efficiency by circumventing stochastic cell loading, and a normally-closed electrostatically actuated microvalve to allow the flow of desired drug and control the routing of the droplets in microchannel network. The overall schematic of the multidrug analysis system is illustrated in Figure 1.4.

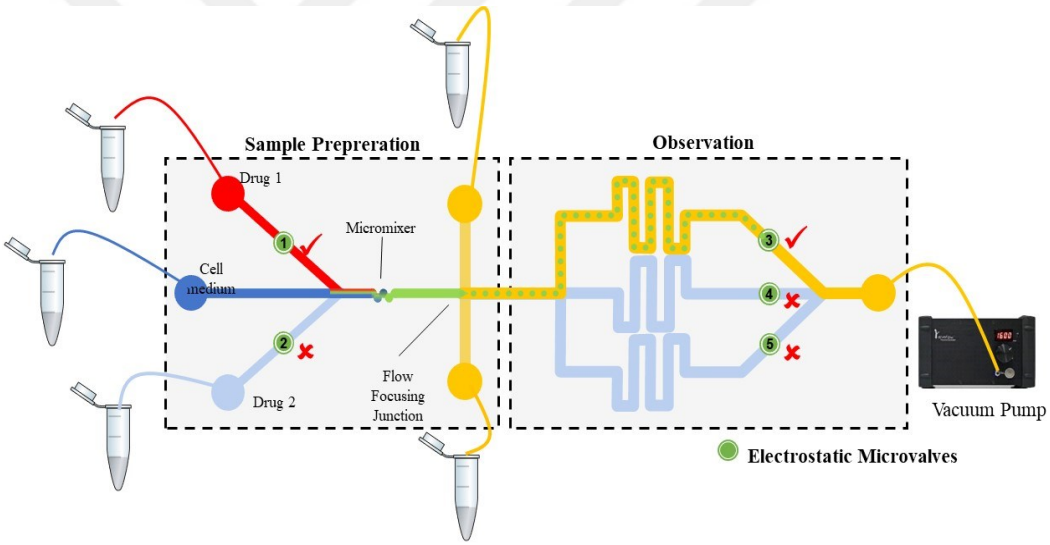

Figure 1.4. Overall schematic of proposed integrated multidrug effect analysis device.

Mixing is an important objective while realizing proposed LOC system because microscale interaction of desired drug composition and cells should be carried out on-chip to render multi-drug analysis possible. The homogeneity of the drug-cell medium composition is the most important parameter which ensures the success of sample preparation unit before arriving flow-focusing junction. Droplet generation unit includes a conventional flow-focusing junction to ensure formation of isolated tiny

compartments where drug-cell interaction can be observed at single-cell level. A major limitation in droplet-based single cell analysis systems is that the encapsulation of the cells is dictated by Poisson distribution due to stochastic cell loading. This intrinsic limitation can be overcome by hydrodynamic focusing of cells before generating the drops. Here, the passive micromixer included in the microchannel network also enhances the single-cell encapsulation ratio to a certain degree by hydrodynamically focusing the cells to the middle of the microchannel. Lastly, the design comprises multiple spiral-type observation areas to gather the drops for cytotoxicity screening. While operating the LOC system, if the microvalves #1 and #3 are actuated, a homogenous mixture of drug 1 and cell suspension will be prepared through passive micromixer. After flowing through the micromixer, the drug-cell composition encounters lateral oil flows at flow-focusing junction where droplets pinch-off and the generated droplets are collected at top spiral channel to be observed for cytotoxicity. Proper functioning of these subunits enables both preparation and analysis of the samples in a single device. The control of the system is ensured by the integration of the normally closed microvalves in order to manipulate the drug-cell combinations and gather them in different chambers for drug efficacy observation.

1.3. Organization of the Thesis

In the first chapter, the importance of quantitative analysis at single-cell levels is emphasized. Then, the motivation and objective of the thesis is presented.

Chapter 2, in general, discusses a wide spectrum for the for the phenomena of the mixing process in microscale. The fundamentals of transport physics in micromixers will be covered, and a short overview of available micromixers in literature will be highlighted in two categories as active micromixers where mixing is induced by external energy sources and passive micromixers where mixing relies on mainly on molecular diffusion or chaotic advection. After covering fundamental physics and available micromixer types in literature, the model geometry of a contraction-expansion array (CEA) microchannel will be described. Subsequently, the mixing

efficiency of the model for different number of array elements at low-to-intermediate Reynolds number range will be evaluated by CFD analysis using COMSOL Multiphysics® v5.3a to inspect the flow profile and mixing performance.

Chapter 3 delves deeply into the transport phenomena in multiphase flows and the mechanism of droplet formation in a flow-focusing microchannel. After covering the common strategies of on-chip droplet formation, numerical schemes for modeling multiphase flows by interface tracking will be discussed in detail. Subsequently, as a key tool to investigate the breakup behavior of water-in-oil droplets, phase-field method will be employed on a geometry of a flow-focusing junction by using COMSOL Multiphysics® v5.3a to obtain information pertaining to temporal and spatial dynamics of the flow.

In Chapter 4, initially, the current state of art aiming to overcome the stochastic cell loading into droplets will be introduced. After presenting a short literature review, to be able to present a robust and versatile solution to circumvent the Poisson distribution in single-cell encapsulation without the assistance of externally applied fields, the principles of microfluidic inertial focusing will be elaborated. Thus, the fundamentals of inertial microfluidics will be covered by defining several forces acting on a particle in a microfluidic channel to be able to understand the dynamics of particle ordering. Then, a direct numerical simulation (DNS) study will be implemented to accurately calculate the total lateral force on a particle in straight rectangular channels of different aspect ratios using COMSOL Multiphysics® v5.3a. The obtained lift force will be interpolated to several types of microchannels with the same rectangular cross-section to reveal the expected particle trajectories. Finally, the decision of a specific channel geometry which facilitates the self-ordering of the particles will be made to be inserted in the design of the full droplet workflow in order to enrich single cell encapsulation efficiency.

In chapter 5, the fabrication of microfluidic devices which is used in experimental characterization of micromixer, droplet formation and hydrodynamic cell ordering is

presented. Then, the experimental results regarding each phenomenon will be compared with the results of numerical analysis given in preceding sections. Eventually, the microfluidic sub-units are combined to compose a full droplet screening workflow, after deciding the joint operation range. As a proof of concept, the complete microfluidic device is tested to quantitively score cell viability within intact droplets and assess the response of K562 cells to the chemotherapy drug doxorubicin.

In Chapter 6, after giving a brief overview regarding the different types of active microvalves and their actuation schemes, an electrostatically actuated normally closed microvalve will be presented for internal control of the fluid flow. The analytical formulations and numerical analysis of the proposed electrostatic microvalve will be completed including several design considerations such as deflection of the membrane under an applied pressure, and pull-in voltage. Sequentially, Chapter 7 will cover MEMS fabrication of normally closed electrostatically actuated microvalves. Finally, the experimental characterization results of fabricated microvalve prototypes will be given.

The last chapter summarizes the overall work and highlights the essential points of the thesis. Also, the future works and suggestions related to research are presented at the very end.

CHAPTER 2

MICROMIXERS

Micromixers are essential and widespread components of microfluidic systems designed for many chemical, biological and biomedical applications such as sample preparation and analysis, drug delivery, protein folding, and development of enzymatic bioreactions [28]. All these applications demand a rapid mixing of two or more reagents or fluid samples before provoking any specific reaction or feeding any specific assay. In the design of the multidrug effect analysis system, the utilization of a micromixer is imperative to ensure a homogeneous mixing of drug solutions and cell medium before arriving droplet junction.

This chapter, in general, discusses a wide spectrum for the phenomena of the mixing process in microscale. The fundamentals of transport physics in micromixers will be covered, and a short overview of available micromixers in literature will be highlighted in two categories as active micromixers where mixing is induced by external energy sources and passive micromixers where mixing relies on mainly on molecular diffusion or chaotic advection. After covering fundamental physics and available micromixer types in literature, the model geometry of a contraction-expansion array (CEA) microchannel will be described. Subsequently, the mixing efficiency of the model for different numbers of array elements at low-to-intermediate Reynolds number range will be evaluated by CFD analysis using COMSOL Multiphysics to inspect the flow profile and mixing performance.

2.1. Fundamentals of Transport in Microscale

In macroscale where Reynolds numbers are large enough (typically >2300), the mixing of two fluids can already be achieved by the means of turbulence (Figure 2.1 (a)) in the dominance of convection [28]. Here, the Reynolds number (*Re*) is a

significant dimensionless quantity which defines the direct ratio between inertial forces to viscous forces (2.1) and helps to forecast whether the flow pattern is laminar or turbulent where ρ, u, μ, and D_h are the density (kg/m^3), fluid velocity (m/s), and dynamic viscosity (Pa·s) of the fluid, respectively and D_h is the characteristic length scale (m).

$$Re = \frac{\rho u D_h}{\mu} \tag{2.1}$$

However, for microchannels whose cross-sectional dimensions are less than one millimeter, turbulence regime is difficult to accomplish. In order to be more specific, for microdevices, since the expected Reynolds numbers is mostly smaller than 100; inertial effects are dominated by viscous effects; thus, a laminar flow profile (Figure 2.1 (b)) forms in the microchannel where streamlines of the flow are parallel to one another and convective mass transfer realizes merely in the flow direction [29]. Therefore, the mixing process in this regime is dominated only by molecular diffusion.

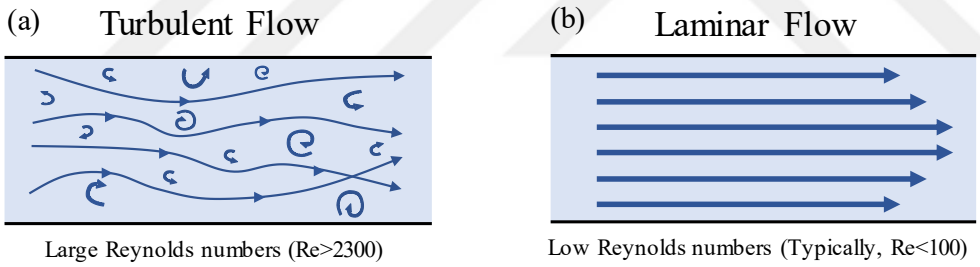

Figure 2.1. Schematic sketch of (a) turbulent and (b) laminar flow.

The short length scales of microchannels could lead to a simple misconstruction that the mixing occurs in a very short time. Achieving mixing in microscale is highly challenging in the absence of turbulent effects because low diffusivity of most species and macromolecules of interest causes very high Peclet numbers, so mixing process grows so slowly that requires long straight channel length. The Peclet number (Pe) is a dimensionless quantity representing the ratio of the contributions of mass transport by convection to mass transport by diffusion where D_h, U, and D are the

characteristic length (m), velocity (m^2/s), and diffusion constant (m^2/s), respectively. Usually, the liquids and macromolecules own a diffusion coefficient on the order of 10^{-9}-10^{-11} m^2/s [30].

$$Pe = \frac{D_h U}{D} \tag{2.2}$$

Here, it is apposite to confer the basic physics behind the mixing process in microchannels where the flow is completely laminar in order to reveal required time and length to achieve mixing. The transport of species carried along with an incompressible fluid flow, moves with the fluid, and does not affect that flow is governed by passive scaler convection-diffusion equation where D is the diffusion coefficient of concerned species (m^2/s), c is the concentration of species (mol/m^3), $\boldsymbol{u}$ is the velocity field of the flow (m/s):

$$\frac{\partial c}{\partial t} = D\nabla^2 c - \boldsymbol{u}\nabla c \tag{2.3}$$

If the flow is laminar, the convective effects are negligible, so the convection-diffusion equation can be directly reduced to Fick's second law for diffusion which can be denoted as:

$$\frac{\partial c}{\partial t} = D\nabla^2 c \tag{2.4}$$

First, the equation can be solved by considering a quiescent fluid for an infinite 1D domain where the initial domain concentration is given for $x < 0$ by $c = c_\infty$ and for all $x > 0$ by $c = 0$ at $t = 0$. Hence, the solution of the one-dimensional equation which is governed by a passive scalar diffusion problem is given by:

$$c(x,t) = \frac{1}{2} c_\infty erfc\left(\frac{x}{2\sqrt{Dt}}\right) \tag{2.5}$$

This solution approaches $c = c_\infty / 2$ after an infinite amount of time everywhere. Here, the distance $\sqrt{Dt}$ is the diffusion length where the system reaches a halfway to the

equilibrium and appraises how far distance the concentration at one side has propagated into the other in the corresponding direction in time t by diffusion, and so, serves as a scaling measure. At this point, this 1D solution can directly intertwine with the steady-state laminar flow case in a microchannel whose depth is shallow relative to its width. However, in this case, the distribution of concentration will change in the transverse direction with the time y/U where U is the average velocity of the flow in y-direction as illustrated in Figure 2.2.

For instance, in a microchannel whose width is 200 μm and depth is relatively shallow, it takes 400 s to reach a halfway equilibrium if diffusion coefficient D=10^{-9} m^2/s. This close affinity between the quiescent fluid and laminar flow is modelled from [31] to illuminate the fundamentals of mixing in microscale. Here, if one assumes a water flow of $\mathrm{Re} = 1$, the halfway equilibrium necessitates a channel length of several meters. The necessary channel length linearly elongates for flows with the magnitude of Reynolds number which results in clearly unacceptable microdevice dimensions. Thus, efficient and versatile designs for facilitating mixing mechanism over a short length are essential to exploit the potential of lab-on-a-chip technologies.

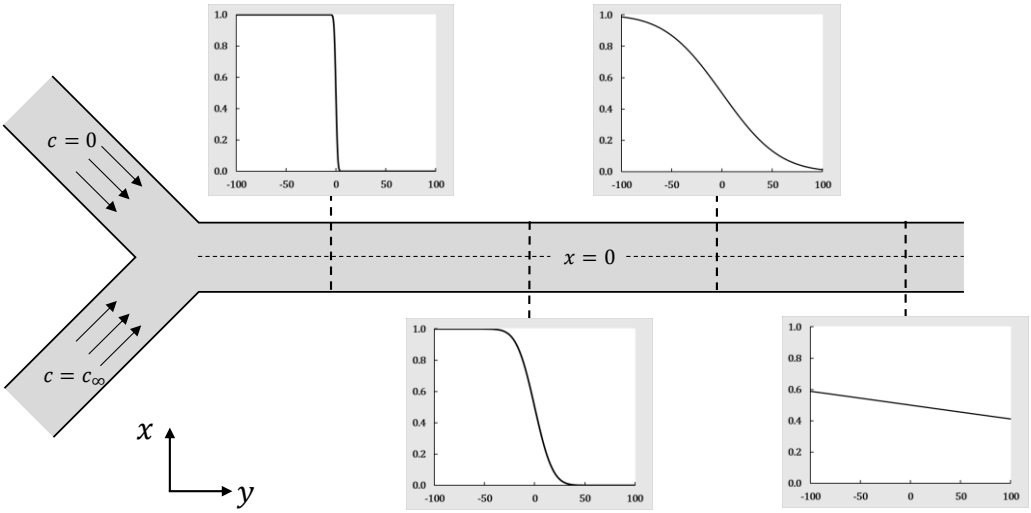

Figure 2.2. A microchannel that replicates the 1D pure diffusion solution. The channel depth is assumed to be shallow in comparison with its width.

2.2. Common Types of Micromixers in Literature

Numerous micromixer designs have been proposed to solve the problem of mixing in the microscale under primarily in two distinct classes: active and passive micromixers. The active mixing methods includes the acoustic waves [32]–[36], magnetic fields [37], [38], pulsating flows [39], [40], electrokinetics [41]–[46], thermal [47] or optical [48] principles. They generally yield superior performance in comparison with the passive micromixers in which the flow is only controlled by altering the channel geometry. Especially, their non-invasive nature and simple application mechanism which waves induce pressure fluctuations and disturb laminar flow attribute appreciable attention to acoustic wave based active micromixers [49]. On the contrary, although the mixing performance is usually higher, the utilization of active micromixers in microfluidic most systems may not be practical, since they need external energy for actuations. In this point, passive micromixers are widely preferred because they do not require utilization of any type of external energy and enhance mixing performance by benefitting from hydrodynamic forces to agitate or rotate the flow. There are different approaches to the passive mixing of liquids that have been largely investigated and previous reports on passive micromixers can be categorized in two which are lamination and chaotic advection.

For the lamination approach, the aim is to hydrodynamically shorten the diffusion length while increasing the total interfacial area between the fluids where the flow is laminar by nature. It utilizes split and recombine technique where the streams of flow are split into several channels, then redirect and recombine in order to create lamination of fluids yielding a significant decline in required diffusion length and time by an exponential increase in interfacial area between species [50]–[52]. However, this type of design necessitates 3D channel geometry which complicates the fabrication by using conventional methods.

Chaotic strategies are induced by geometric alterations such as obstacles of various shapes in the channel, ribs or grooves on channel walls, serpentine or zig-zag shaped

channels where flows in transverse plane passively generated to enhance mixing process [53]–[55]. The objective here, primarily by geometric modification in a channel, is to introduce convection to continuously stir the flow in laminar regime by disarranging the straight and parallel streamlines; hence, obviate the dominance of diffusion in mixing process thanks to bulk motion of samples thanks to shortening of the diffusion length scale. These designs are mostly planar which does not require three-dimensional channels and complex microfabrication approaches. Another passive planar micromixer which consists of consecutive contractions and expansions along the channel is reported by Lee et al [56]. In this design, the array induces transverse velocity components which are called Dean flow thanks to centrifugal forces. This secondary flow perturbs the laminar flow, thereby enhancing mixing by circulation at low or moderate Reynolds number flows. In another study, they propose an alternate version of their array structure where contraction regions purposely placed left and right in order to yield appreciable mixing performance even at high Reynolds numbers by inducing expansion vortices due to flow separation [57]. Several examples of passive micromixers proposed in the literature are shown in Figure 2.3.

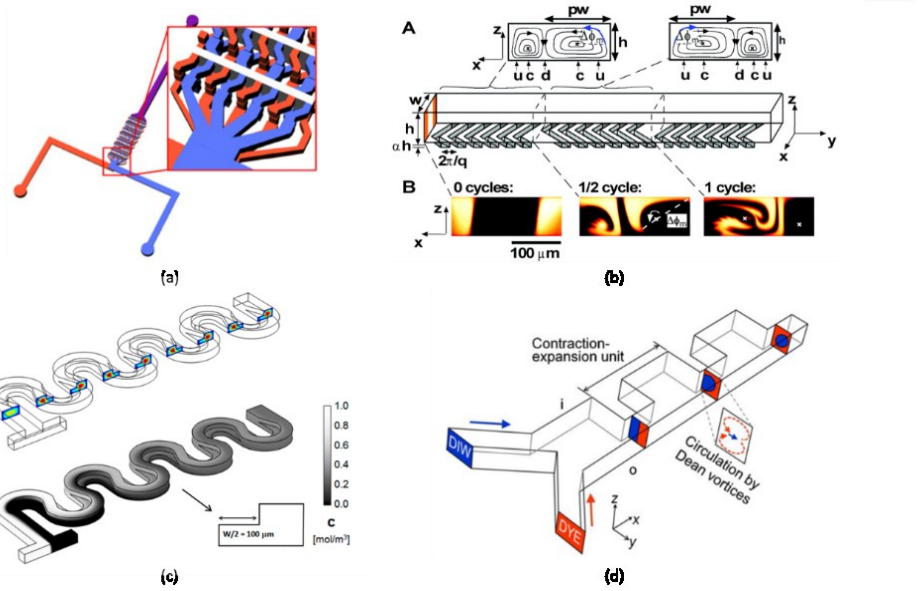

Figure 2.3. Examples of passive micromixers from literature. (a) A 3D lamination micromixer [52]. (b) A micromixer with grooves in the channel wall [58]. (c) An enhanced serpentine micromixer with non-rectangular cross-section [53]. (d) A contraction-expansion array type Dean micromixer [56].

2.3. Design and the Geometry of the Proposed CEA Micromixer

The proposed micro-mixer consists of sequential nodes in the form of zig-zag along the channel. As depicted in Figure 2.4, the passive micromixer comprises sequential throttles that are connecting several circular wells which follow a Y-type junction. First, the parameters which characterize the micro-mixer is determined. Accordingly, the throttle width (t), the number of throttles (N), the shifting angle (θ) are the basic parameters describing the micromixer. It should be averred that the throttle width (t) varies depending on the d/w ratio. Consequently, the major geometric parameters that affect the performance of the micromixer can be expressed as d/w, N and θ. The influence of these parameters to the mixing efficiency investigated individually in [59]. In this thesis, only the effect of the number of throttles (N) will be evaluated while keeping t and θ constant, 50 µm and 45° respectively.

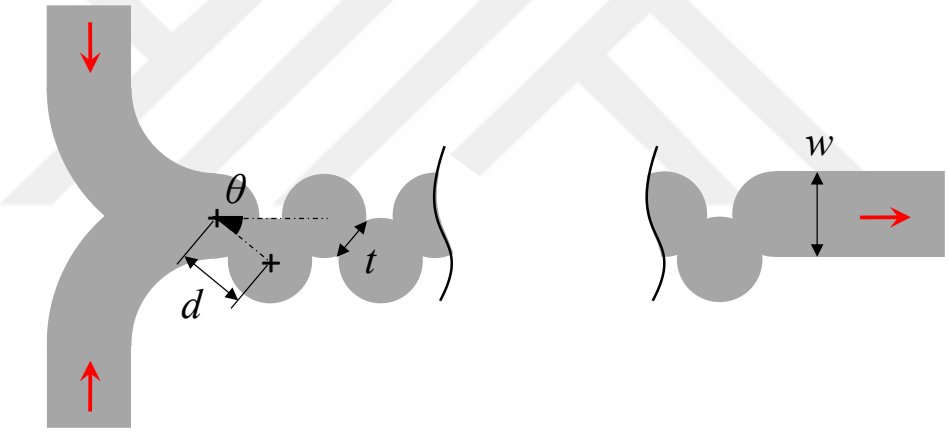

Figure 2.4. Schematic 2D view of the CEA type micromixer. Arrows represent the direction of the flow.

2.4. Numerical Model of Mixing in Microscale

For simulations of proposed CEA type passive, 3D models of the geometries were created and two different physics, namely laminar flow, and transport of diluted species, were used in COMSOL Multiphysics® v5.3a. Thus, velocity and pressure fields were computed by using the single-phase, steady-state and incompressible Navier-Stokes equation (2.6) and the continuity equation (2.7) where ρ is the fluid

density (kg/m^3), $\boldsymbol{u}$ is the velocity field (m/s), p is the pressure field (Pa), $\boldsymbol{I}$ is the unit diagonal matrix, μ is the fluid dynamic viscosity (Pa·s), and $\nabla\boldsymbol{u}+(\nabla\boldsymbol{u})^T$ denotes strain-rate tensor which viscous stress tensor directly depends on [60].

$$\rho(\boldsymbol{u}\cdot\nabla)\boldsymbol{u} = \nabla\cdot\left[-p\boldsymbol{I} + \mu\left(\nabla\boldsymbol{u} + (\nabla\boldsymbol{u})^T\right)\right] \tag{2.6}$$

$$\rho\nabla\cdot(\boldsymbol{u}) = 0 \tag{2.7}$$

After obtaining velocity and pressure fields, the species concentration field is assessed by using convection-diffusion equation (2.8) where c is the species concentration (mol/m^3), D is the diffusion constant (m^2/s), and R is the rate of reaction (mol/m^3·s) which is zero for the case assuming no chemical reaction.

$$\nabla\cdot(-D\nabla c) + \boldsymbol{u}\cdot\nabla c = R \tag{2.8}$$

2.5. Boundary Conditions and Simulation Setup

The boundary conditions of laminar flow model are as follows: no-slip at solid channel walls, laminar inflow defined by a constant flow rate which corresponds to a specific Reynolds number at the inlet, and zero pressure at the outlet. The entrance length, L_e, is calculated in order to ensure the flow is fully developed where Re and D_h are the Reynolds number and the characteristic length of the microchannel (m), respectively.

$$L_e = 0.06\,Re\,D_h \tag{2.9}$$

The stationary flow field equations were computed by using a direct solver in order to eschew possible numerical convergence issues during a parametric sweep study of a wide range of Reynolds numbers defining the inlet boundary condition. Although direct solvers are greedy in terms of memory usage, they generally tend to converge more easily without any problems. For 3D laminar flow model, P1+P1 discretization which defines first order elements for both pressure and velocity is used, and the mesh is refined to the point that solver does not switch to out of core mode. At this point, for denser meshes, an iterative solver, algebraic multigrid method (AMG) which

provides robust solutions for large Computational Fluid Dynamics (CFD) problems is utilized for calculation of flow fields [60]. Additionally, a solution that is obtained on a coarse mesh by using a direct solver is used to define an initial guess of the iterative solver; consequently, the solver commenced with a good starting point and tends to arrive convergence faster.

Since species concentration does not affect the flow field, a one-way coupling method is used. In one-way coupling, first, flow fields are computed until the desired convergence criterion is achieved; then, the solution is interpolated to the transport of diluted species model. Finally, the species concentration model is iterated up to the desired convergence.

For the transport of diluted species model, a step function is used to define the spatial distribution of species concentration at the inlet. The minimum and maximum species concentration values were presumed to be 0 and 1 mol/m^3 and stepped along the width of the fluid which flows through the inlet. To improve the accuracy of computed concentration field, quadratic discretization was implemented. For the transport model, the number of degrees of freedom is always much smaller than laminar flow model at same discretization; hence, a direct solver is always preferred to compute the steady-state species concentration field.

For meshing of the geometry, first, a 2D mesh is generated at the top wall boundary by using free triangular elements. The mesh is refined at the characteristic regions of mixer which are the throttle regions and curved external boundaries at the edges of wells by using corner refinement utility. Moreover, two layers of boundary mesh are defined to resolve the near-wall flow. Then, using the swept mesh functionality, triangular prismatic mesh elements are generated along the straight sections which defines the channel height, 200 μm. To preserve the density of boundary layers near the wall in the transverse direction, the swept mesh is geometrically distributed. In Figure 2.5, 3D mesh and boundary conditions of the passive CEA micromixer with 21 throttles is illustrated.

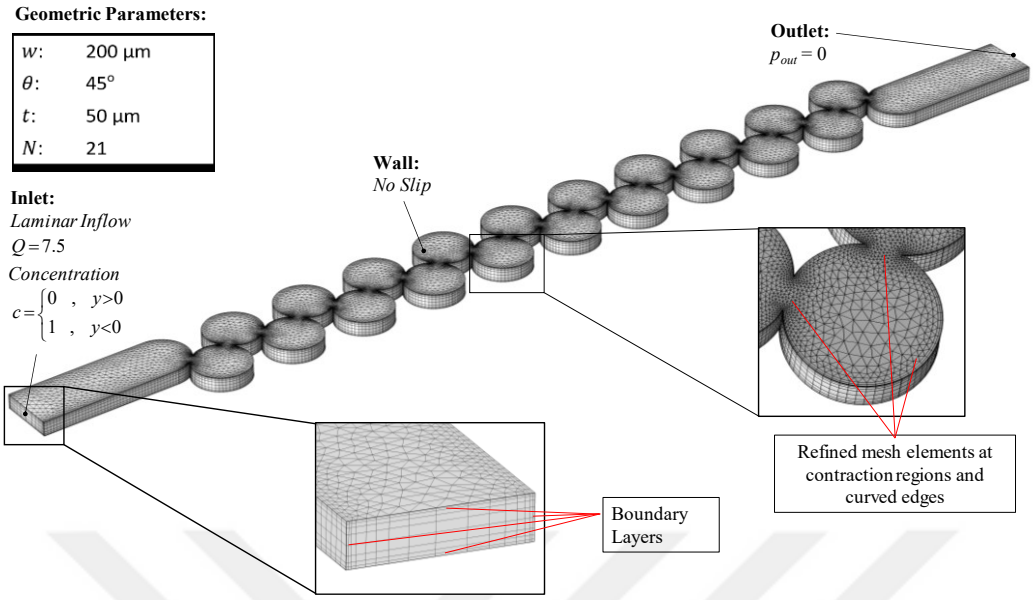

Figure 2.5. Mesh Details and boundary conditions used in COMSOL model of CEA micromixer.

During the simulations, the quantification of the extent of mixing process is significant to evaluate the performance and optimize the design parameters. Here, the standard deviation of species concentration (σ) was obtained by using (2.10) at the inlet and the outlet which are the cross-sections perpendicular to the flow direction. For the formulation, c_i is the species concentration of an element, $\bar{c}$ is the desired final concentration and N is the number of mesh elements. Following this, as a figure of merit, the mixing index (M) was calculated by (2.11) to appraise the mixing efficiency.

$$\sigma = \sqrt{\frac{1}{N}\sum_{i}^{N}\left(c_i - \bar{c}\right)^2} \tag{2.10}$$

$$M = 1 - \frac{\sigma_{outlet}}{\sigma_{inlet}} \tag{2.11}$$

As a recapitulation, during the simulations, the mixer performance is assessed with respect to a single geometrical parameter, namely number of throttles, at moderate Reynolds numbers. In order to avoid extremely long channels in one direction, a serpentine-like channel orientation is utilized for every series of 21 mixing units.

2.6. Simulation Results and Discussions

Simulation results give elaborated insights into parameter dependent mixing efficiencies and help to apprehend the results by revealing different mixing mechanism that emerges in the proposed CEA micromixer. First, as mentioned earlier, mesh independence study was first carried out to obtain suitable mesh number for further simulations. Thus, by refining the number of mesh, mixing index (M) was computed for a mixer model with N=21 and plotted in Figure 2.6 with respect to the number of degrees of freedom (DOFs) which numerical study utilizes to compute concentration field. This study is conducted for a Reynolds number of 7.5.

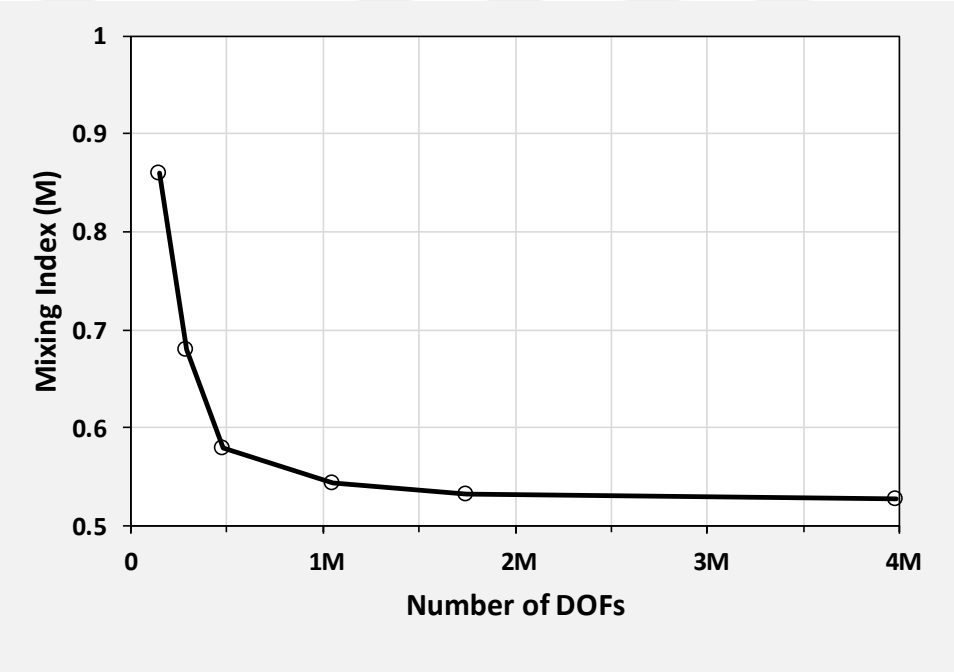

Figure 2.6. Mesh dependence of mixing index for a micromixer with N=21.

Representative results for species concentration and velocity magnitude profiles of proposed CEA model micromixer with N=63 and Q=45 µl/min is first presented in Figure 2.7. As can be seen from Figure 2.7 (a), at this configuration where Re=6, the complete mixing could not be obtained; however, it provides a mixing efficiency which is higher than %80.

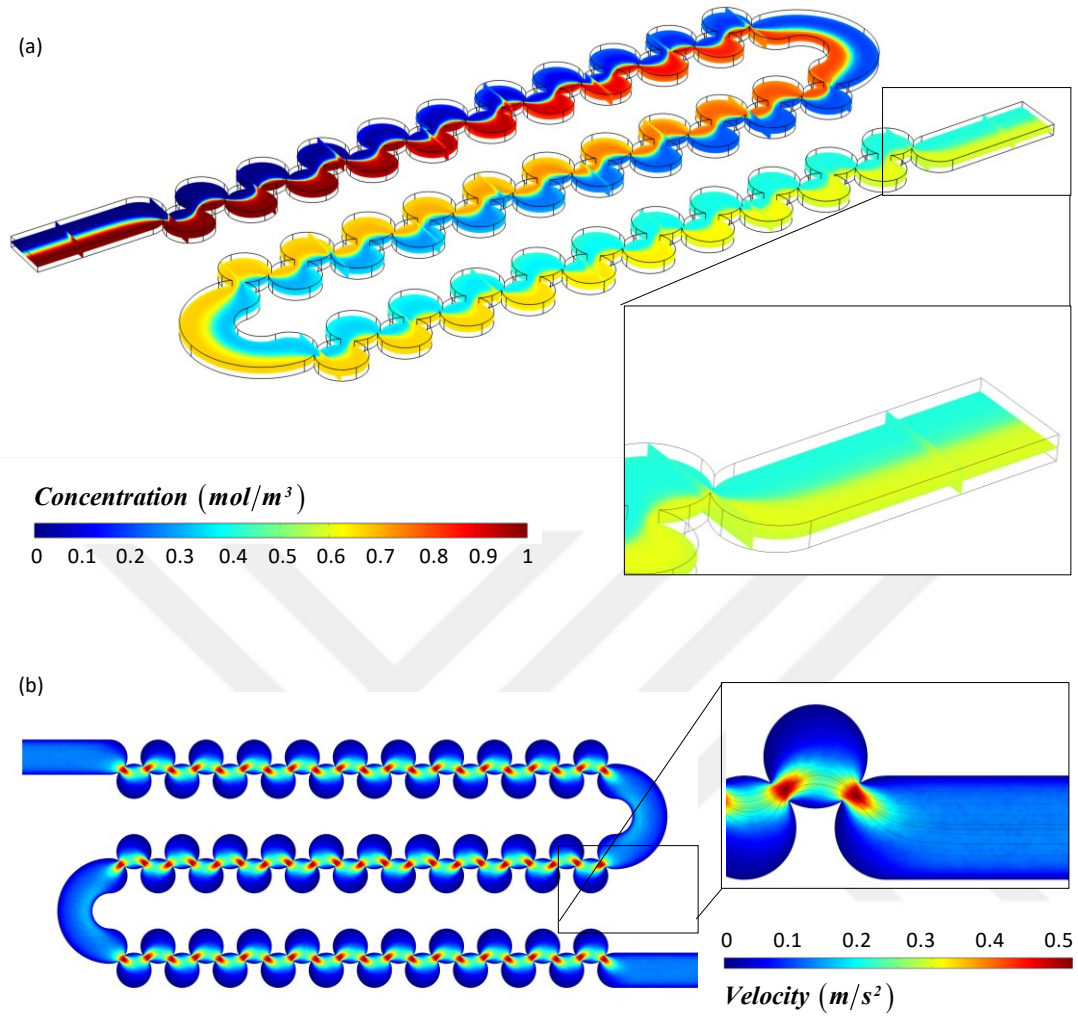

Figure 2.7. Species concentration and velocity profile of the mixer with 63 throttles. The flow rate is Q=45 µl/min (Re=6).

By increasing the flow rate at the inlet, higher mixing efficiency can be obtained. Figure 2.8 plots the simulation results indicating the mixing index with respect to the number throttles and different Reynolds numbers ranging from 0.25 to 40. As expected, the increase in the number of throttles enhances the mixing at all flow rates and its effect is linear at respectively low Reynolds numbers. In order to apprehend the mixing behavior with respect to flow rate, the fluid behaviors observed during the simulations should be delved deeply. Mainly, three different mixing mechanisms were observed.

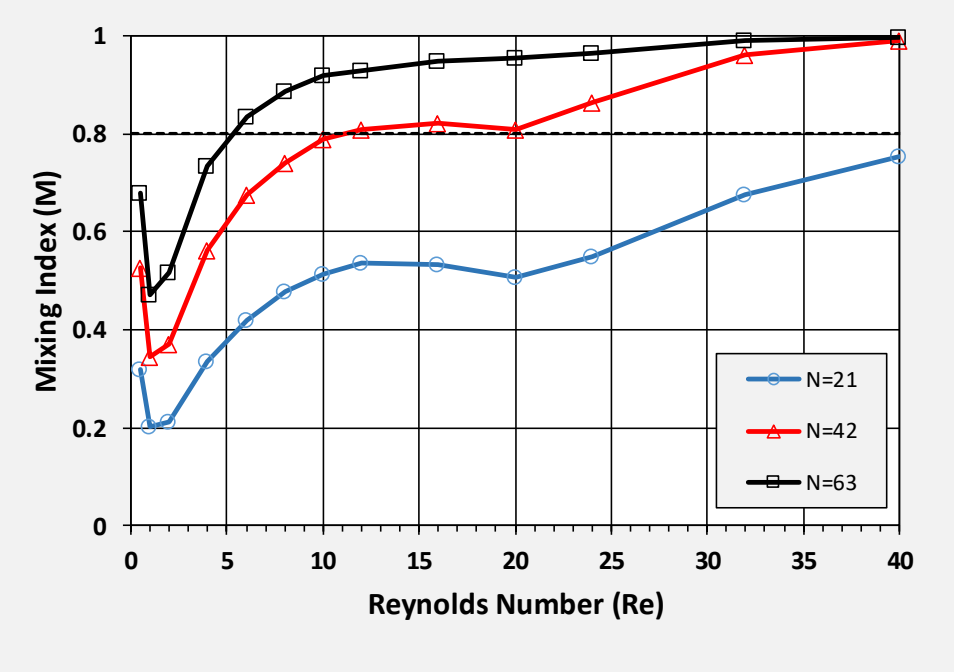

Figure 2.8. Mixing index with respect to the number of throttles and Reynolds numbers. The dashed line represents the mixing efficiency of %80.

First, the sudden successive contractions facilitate the mixing process by shortening the diffusion length. This behavior is dominant for flows at low Reynolds numbers (Re<4) where the mixing occurs only by molecular diffusion and as Reynold number increases, this effect attenuates due to the proportional increase in Peclet number. In this regime, mixing index abates while flow rate in the microchannels grows.

Second, consecutive expansion and contractions cause the flow to follow curved streamlines due to change in the cross-sectional area, thus form circulation vortices in the transverse direction like Dean vortices observed in curved channels [61] as illustrated in Figure 2.9 (b-c). The generation of these vortices leads to chaotic advection and enriches the molecular transport by convection. The zig-zag orientation causes the rotation direction to switch clock-wise to counter-clockwise and further enhances the mixing. This behavior emerges at a higher Reynolds number in comparison to first behavior (Re=4) because a significant rise in mixing efficiency is observed for all configurations at this flow rate. Here, the dimensionless Dean number, De, can be recalled as a measure of the Dean flow, which states the relative proportion

of inertial and centrifugal forces to viscous ones. The mixing unit is the same for all configurations, so the hydraulic diameter and radius of the curvature is constant and independent from the number of throttles. Therefore, *De* is directly proportional to *Re* and it is transparent that mixing efficiency is increases with respect to *Re*. Moreover, this geometry configuration allows extremely small radius of the curvature which is the radius of a single circular well in comparison with the spiral or serpentine channels and exploits higher De values for relatively lower Reynolds numbers; thus, significantly perturbs streams of laminar profile and enhance both mixing time and efficiency. However, it eventually begins to saturate as the intensity of the flow in the axial direction increases.

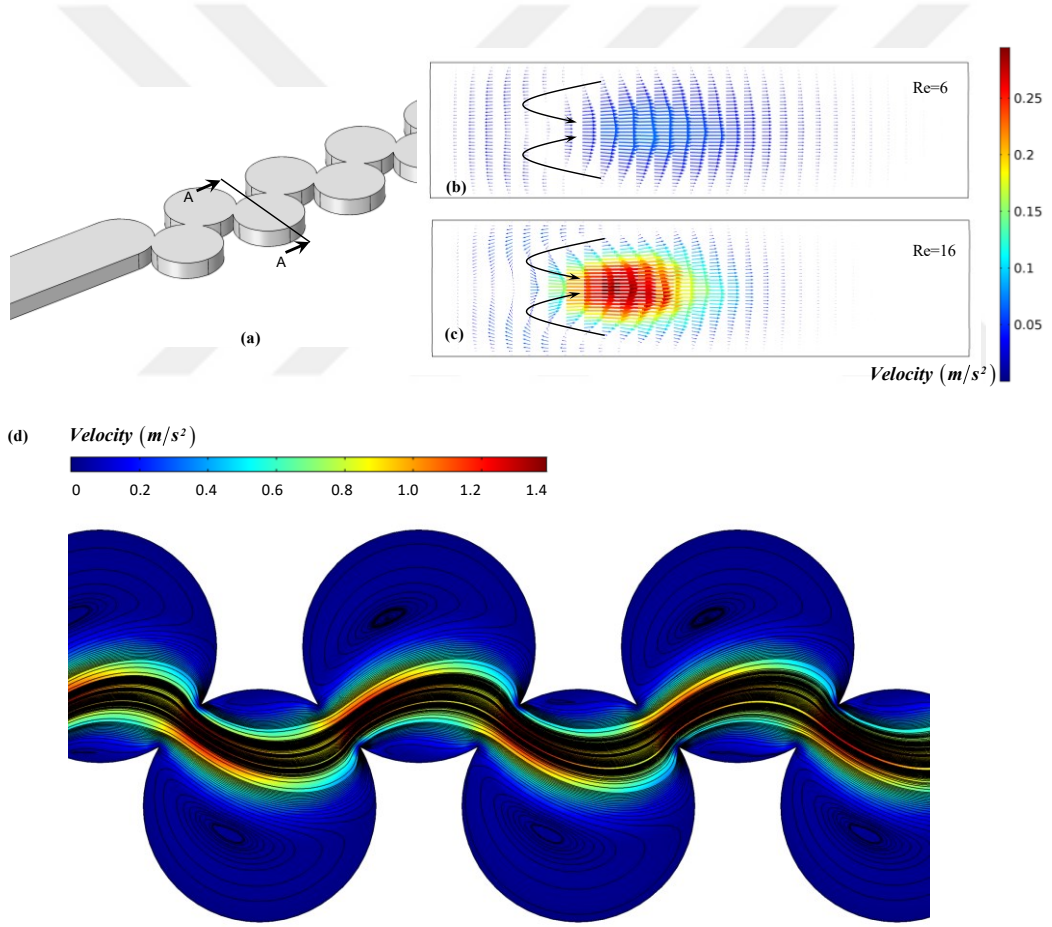

Figure 2.9. Formation of Dean vortices in the proposed CEA micromixer. (a) Cross-section. (b) and (c) Simulation results which are illustrated for *Re*=6 (45 µl/min) and *Re*=16 (120 µl/min). (d) Formation of expansion vortices at *Re*=20. The formation of these vortices facilitates mixing of species at respectively high Reynolds numbers.

Third, as Re further increases above a critical value (around *Re*=20), an expansion vortex begins to be formed due to flow separation (Figure 2.9 (d)). These vortices create a flow which recirculates adjacent to the channel walls at expansion regions when separated streamlines at the corners of contractions reattend to the wall downstream. Expansion vortices coupled with the Dean flow which circulates in the transverse direction enhance the mixing efficiency up to a further degree.

A chaotic-advection based contraction-expansion type passive micromixer with circular wells was presented in this chapter, and its mixing performance was evaluated numerically in COMSOL. Numerical simulations were carried out by using Navier–Stokes equations to obtain regarding velocity and pressure fields. Resulting velocity field was used to calculate the concentration field using the convection–diffusion equation. The effect of the number of throttles on the mixing efficiency of micromixer was considered at Reynolds numbers ranging from 0.25 to 40. Several mixing mechanisms which are observed in the micromixer was discussed elaborately and clearly visualized with simulation results. By increasing the number of the throttles, even in low Reynolds numbers (*Re*=6), a mixing efficiency above %80 can be obtained. Besides, thanks to planar geometry of the mixer structure, it can easily be adapted for conventional photolithography techniques. The passive micromixer structure will be included in the design of the multidrug analysis system to ensure an almost homogeneous mixing of drug solutions and cell medium.

CHAPTER 3

DROPLET FORMATION

Droplet microfluidics was exploited and rapidly progressed in recent years and offer new remarkable insights to diverse applications, especially in the areas of chemistry and biology. Microdroplet technology provides several distinctive features that can bolster a scope of various researches in a wide assortment of application fields, including nano- and microscale particle synthesis [62]–[65], single cell analysis [66], [67], drug discovery [68], [69], therapeutic agent delivery [70], medical diagnostics [71], [72], microbiological population analysis [73], and food industry [74]. Here, the main remarkable advantages of droplet microfluidics encompass the miniaturization, compartmentalization, monodisperse and high-throughput generation. By utilizing microfluidics technology, thousands of drops where every single one is a tiny compartment isolated from its surrounding environment by the stabilized liquid-liquid interface can be generated in seconds. Thus, any reaction occurs independently by forestalling any kind of undesired adsorption from reagents in this confined environment. This enables enhanced control over the process conditions during the analysis or reaction.

This chapter, concisely, delves deeply into the transport phenomena in multiphase flows and the mechanism of droplet generation in a flow-focusing microchannel. After covering common strategies pertaining to on-chip droplet formation, numerical schemes for modeling multiphase flows by interface tracking will be discussed in detail. Subsequently, as a key tool to investigate the breakup behavior of water-in-oil droplets, the phase-field method will be employed on a geometry of a flow-focusing junction by using COMSOL Multiphysics ® v5.3a to obtain information pertaining to temporal and spatial dynamics of the two-phase flow.

3.1. On-chip Droplet Formation

Essentially, a ubiquitous way to form an emulsion is to take two immiscible fluids (e.g., oil and water) together and rigorously agitate them to disperse one liquid into another by enormous shear; however, bulk emulsification is particularly prone to precipitate the formation of polydisperse droplets due primarily to viscous forces resulting from inhomogeneous turbulence flows. Polydispersity has been a constraint that discourages the digitalization of compartments due to the indefinite distribution of reagents. Recently, thanks to the advance in microfluidics, a multitude of different formation techniques offer a high degree of control on dispersity of droplets by enabling to tune their sizes and generation frequencies. Numerous techniques have been proposed to eradicate the problems of bulk emulsification in the microscale under primarily in two distinct classes: active methods that rely on actuation of interfacial instabilities induced by external fields and passive methods that depend on hydrodynamic forces. Although active generation provides important advantages over the latter, including allowance of independent alteration of size and frequency or prompt response time [75], in this thesis, as a subsystem of multi-drug analysis system, passive droplet generation strategy is preferred because they are also capable to allow formation of monodisperse drops often at higher frequencies despite their robust and undemanding operation mode.

The three most prevailing passive configurations are T-junction (cross-flow), flow-focusing and co-flow configurations (Figure 3.1). Concisely, for all passive configurations, the flow of an immiscible fluid to be dispersed (e.g., water) crosses with the flow of another immiscible fluid to be the carrier (e.g., oil) at a junction where droplets pinch off, largely because viscous stresses deform the interface by competing for the capillary pressure which arises from interfacial forces. The process is scaled and characterized by Capillary number (Ca) which expresses the dominance of viscous forces over surface tension forces at the interface where μ is the dynamic viscosity of one phase (Pa·s), U is the average velocity (m/s), and σ is the interfacial tension (N/m).

$$Ca = \frac{\mu U}{\sigma} \tag{3.1}$$

Moreover, even though the inertial forces are negligible in most of the time, for high-throughput applications operating at high flow rates, they might become significant. Here, Weber Number (*We*) represents the ratio of inertial force to surface tension force where ρ is the density of one phase (kg/m^3), U is the average velocity (m/s), D_h is the characteristic diameter (m) and σ is the interfacial tension (N/m).

$$We = \frac{\rho U^2 D_h}{\sigma} \tag{3.2}$$

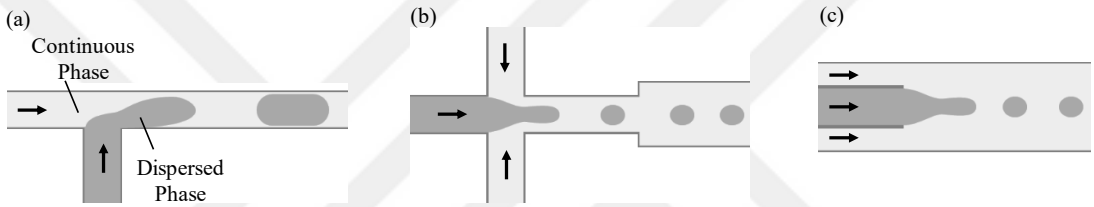

Figure 3.1. Typical passive droplet generation strategies. (a) T-junction microchannel. (b) Flow-focusing microchannel. (c) Co-flow type microchannel.

As first proposed in [76], in T-junction geometry where two phases are injected octagonally as illustrated in Figure 3.1 (a), the dispersed phase forms a thread permeating and elongating into the continuous phase to create a droplet when the pinch-off occurs due to viscous shear. In the second approach called co-flow configuration, the two immiscible phases meet and flows in parallel streams [77]. Drag forces which are generated by coflowing fluid, drops of the dispersed fluid are detached from the end of a smaller inner tube. Moreover, another passive geometry that both phases are compelled to flow through a narrow contraction region together where droplet generation occurs is called flow-focusing configuration and first presented by [78]. This configuration offers a high degree of control over drop size due to a higher number of parameters [79] and a more stable generation due to symmetric shearing [80].

In passive droplet generators, apart from the configuration, a multitude of parameters is involved in droplet formation, including channel dimensions, the viscosities and flow rates of two immiscible fluids, wetting characteristics of channel walls, the usage of the surfactants. As these parameters vary, several generation regimes can be observed, namely, squeezing, dripping, jetting, tip-streaming, and tip-multi-breaking. As mentioned before, the interfacial tension force acts to keep the surface intact and minimize the interfacial energy, while viscous stress attempts to deform the interface. The complex interplay between surface forces and viscous forces establishes the active operation mode of the device.

In squeezing mode, usually referred as the geometry-controlled mode, the dispersed phase protrudes and blocks the flow of continuous phase; thus, this leads to an abrupt increase in the pressure gradient of outer phase while dispersed phase enlarges and squeezes the neck. Once sufficient pressure is built-up, the droplet pinches off. This regime is observed at low Capillary numbers ($Ca_c < 10^{-2}$) where the interfacial tension dominates the viscous effects [81]. The droplet size is larger than the orifice since the principle necessitates its confinement by the channel walls to trigger a pressure build-up on compressed continuous phase.

While dispersed phase inertia is negligible ($We_d < 1$), as the Capillary number of continuous fluid increases ($10^{-2} < Ca_c < 1$), squeezing to dripping transition occurs where the viscous stress surpasses the surface tension [75]. Thanks to large viscous force, in contrast with the squeezing, droplet adopts a spherical shape because the break-up of the neck occurs before the dispersed phase grows in the junction.

By further increasing the flow rates of either phase, the dripping regime can transform into the jetting regime which characterized by an elongated protrusion of the dispersed phase into the carrier phase that its pinched areas ultimately rupture to form droplets due to Plateau-Rayleigh instability because the liquid acts to minimize its surface energy. However, the droplets are prone to variate in size due to capillary perturbation [75]. For instance, in co-flow geometry, two types of jets can be generated with respect

to the force balance argument. If capillary number of continuous fluid is sufficiently high ($Ca_c \geq 1$), the viscous shear stress overwhelms the surface tension force and leads dispersed phase to jetting with a thinner diameter, while widening jet is occurs when inertial forces of the inner phase dominates the capillary forces at the interface ($We_d \geq 1$) so causes a jet formation which widens as it decelerates in carrier fluid. The jetting transition occurs when either or sum of the viscous forces and inertial forces exerted on the interface overcome the interfacial tension forces; thus, namely $Ca_c \geq 1$, $We_d \geq 1$ or $Ca_c + We_d \geq 1$ [82].

An additional mode of break-up called tip-streaming occurs where dispersed phase forms a conical shape and apart from detaching immediately, it pulls a thin liquid thread which ultimately breaks into several tiny monodisperse droplets. This mode arises between squeezing and dripping, and both surfactant-mediated and surfactant-free mechanisms are reported in the literature [75], [83]. In the final regime that has recently been demonstrated, called as tip-multi-breaking, droplets are generated similar to tip-streaming, except in intermittently periodic manner. Moreover, unlike tip-streaming, the drops are polydisperse due to the formation mechanism arises as a result of Rayleigh–Plateau instability [84].

Only squeezing, dripping and jetting modes are present in T-channel geometry, while all others can be observed in co-flow and flow-focusing configurations [75]. Squeezing, dripping and tip-streaming modes enable monodisperse droplet formation, while polydisperse droplets are observed in jetting and multi-tip-breaking modes due to capillary perturbation. All these regimes are illustrated in Figure 3.2. As it is summarized in this section, the problem of droplet formation involves several parameters; thus, the optimal design for the operation of droplet systems necessitates an insightful understanding of the fundamental physics of microscale multiphase flows. In the next chapter, these numerical methods will be discussed.

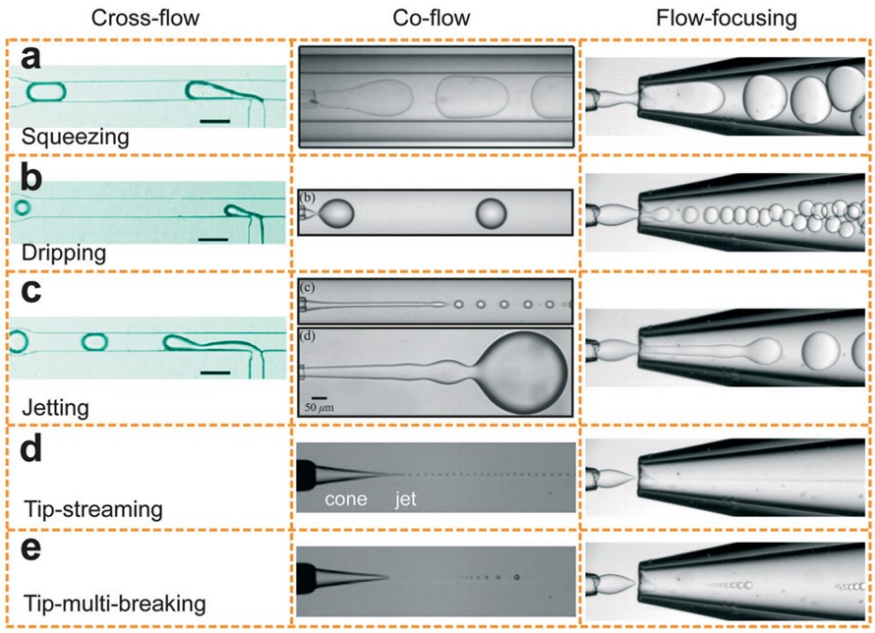

Figure 3.2. Droplet Formation modes in different passive configurations [75]. (a) Squeezing. (b) Dripping. (c) Jetting. (d) Tip-streaming. (e) Tip-multi-breaking.

3.2. Numerical Methods for Multiphase Flows

Modelling and simulation corroborate complimentary insights to apprehend droplet formation dynamics and optimize the design and operation of microfluidic devices. Typically, the Navier-Stokes equations are computed first to acquire spatial pressure and velocity fields; however, in multiphase flow, a serious challenge arises to explicitly treat the interface between the liquid phases which evolves over time and determine its precise location. Several methods have been implemented to model the complex dynamics of multiphase systems that might be categorized into two groups, namely interface capturing and interface tracking. In the tracking method where the interface is assumed to have an infinitely thin sharp thickness, the interfacial surface conditions are treated as a boundary condition. These methods are very powerful and explicitly track the interface because they account for mass transport across the interface. However, for the cases in which severe topological changes occur such as droplet break-up or droplet coalescence, the approach encounters with a singularity problem due to infinite deformation on the grids which significantly limits the

application area of the approach [85]. To be able to handle topological changes, in a natural way, interface capturing methods utilize an indicator function to implicitly differentiate two phases which might represent the volume or mass fraction of the phases or the signed distance to the interface. Rather than formulating the flow of two phases which are split by a boundary representing the interface, capturing methods formulate the surface tension force as a body force spreading over a thin region around the interface. Since the use of interface capturing methods is widespread for multiphase flow simulations which involves topological changes such as droplet dynamics in the literature [86]–[91], these methods, including the volume of fluid method (VOF), the level-set method (LS), and the phase-field method (PF), will be briefly discussed here.

VOF method utilizes the volume fraction of phases which varies between zero to unity to depict the interface according to the fraction of liquid inside each cell. In the VOF method, at every time step, the interface reconstruction algorithm implicitly defines the interface in each cell of the grid based on the volume fraction of two phases. Then, the advection algorithm calculates the new distribution of the volume fraction by solving the transport equation (3.3) purely depending on velocity field where α is the volume fraction and $\boldsymbol{u}$ is the velocity field (m/s).

$$\frac{\partial \alpha}{\partial t} + \boldsymbol{u} \cdot \nabla \alpha = 0 \tag{3.3}$$

Moreover, the continuum surface force (CSF) model (3.4) is incorporated into the incompressible momentum Navier–Stokes equation as a body force accounts the influence of the interfacial tension force at the interface where α is the volume fraction, σ is the interfacial tension (N/m) and κ is the curvature of the local interface (1/m).

$$F_s = \sigma \kappa \nabla C \tag{3.4}$$

In the level-set method, a function of a purely geometrical variable defining the signed distance to the interface initially defined in the entire domain to indicate the interface. The indicator function varies smoothly over the interface; thus, it eliminates the

discontinuity issue of the interface reconstruction algorithms used in VOF [92]. However, in comparison with the VOF, the indicator, namely level set function (ϕ), has no physical equivalent, so the method may violate mass conservation of either phases [93]. Moreover, the method demands a re-initialization parameter to avoid numerical deterioration and restore the level-set function if the topology changes considerably around the interface. The advection of the level-set function is dictated by the same transport equation (3.3) with VOF, and additionally, also the CSF model (3.4) is used to account interfacial forces.

Another numerical scheme for simulating two-phase complex flows is the phase-field method. The phase-field method, also called the diffuse-interface method, is derived from the Ginzburg-Landau form of free energy functional to handle morphological changes of the interfaces based on Cahn-Hillard theory [94]. Therefore, PF method can be construed as physically motivated interface capturing technique in which the evaluation of the indicator, namely phase-field variable, is governed by an advection-diffusion equation and introduces a pressure tensor term that accounts for the surface tension force induced from excess free energy to Navier–Stokes equation. The phase-field parameter is represented by the Cahn-Hillard equation (3.5) where ϕ is the phase-field variable, γ is the mobility ($m^3 \cdot s/kg$) and G is the chemical potential (J/m^3) which can be defined as the functional derivative of the free energy.

$$\frac{\partial \phi}{\partial t} + \boldsymbol{u} \cdot \nabla \phi = \nabla \cdot \left(\gamma \nabla^2 G \right) \tag{3.5}$$

The diffuse-interface model eliminates significant numerical impediments which are encountered in other methods. In VOF, the labeling function undergoes smoothing to prevent discontinuities and needs additional efforts for interface reconstruction. The level-set method, if necessary, redefines the distance function and requires an additional mathematical scheme to ensure mass conservation. However, in the phase-field method, the interface can be continuously maintained without introducing any additional mathematical conditions by the merit of its energy-based formalism [95]. Additionally, the energy conservation of the phase-model method assures solution

existence [95]. Since the phase-field method embodies rich physics governed by free energy formulation which is not present in the VOF and the level set methods, it has some decent advantages that enable sophisticated simulations to explore the evolution of dynamic contact angle or the surfactant-laden interfaces [96], [97]. Apart from all these advantages, the phase-field method embodies a phenomenological mobility parameter whose selection has no explicit criterion to justify the correctness and reliability of simulations, thus it is often corrected after comparing with experimental results [87].

3.3. Description of the Model Geometry

In the design of multidrug analysis system, flow focusing geometry was preferred because it provides a high degree of control over drop size by offering a higher number of parameters and a more stable generation due to symmetric shearing in comparison with the other passive configurations. The schematic of flow focusing geometry that will be used in the simulations is illustrated in Figure 3.3 by highlighting the relevant system parameters.

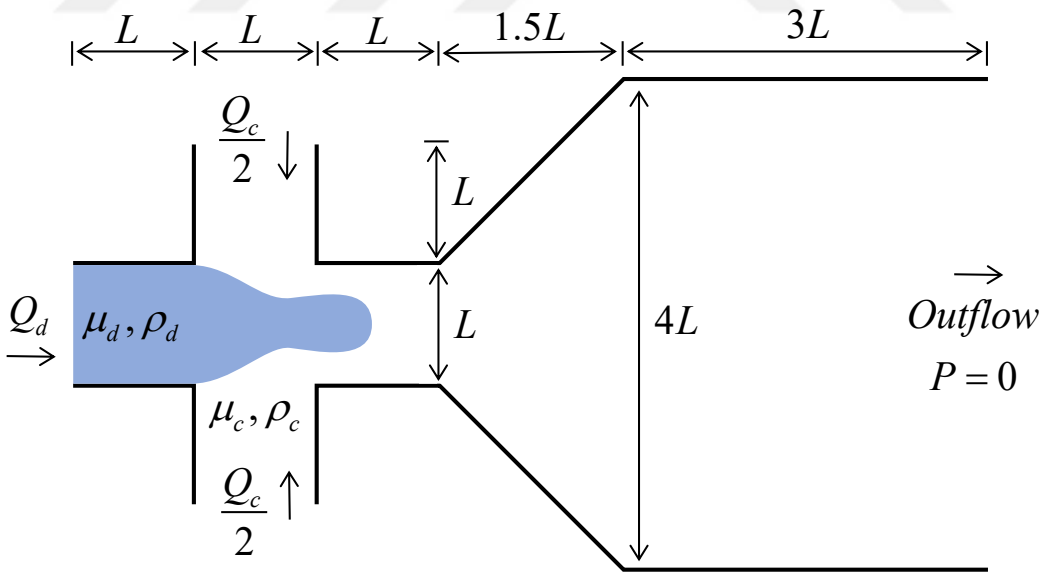

Figure 3.3. The 2D schematic of the flow focusing geometry underlining relevant model parameters. The length, L=50 µm, is used to express the size of the geometry.

There are a single middle inlet and two side inlets whose widths are specified as L=50 μm. The height of the outlet in the downstream is 4L. The thickness of the microchannel is again L=50 μm. The dispersed phase is fed through the middle inlet, while the continuous phase is given into the channel through the side inlets.

The properties pertaining to the system are dynamic viscosities μ_c and μ_d, densities ρ_c and ρ_d of both phases, and the interfacial tension between the phases σ. The formation process can be characterized by the dimensionless numbers, namely the Capillary number of the continuous phase $Ca_c = \mu_c Q_c / L^2 \sigma$ and the ratio of the flow rates $Q_r = Q_c/Q_d$. The Weber number is ignored because it is intended to analyze the emulsification process at squeezing and dripping modes where one might safely shrug the effect of fluid inertia to the interface off.

3.4. Numerical Model of Droplet Formation

For the numerical implementation of droplet break-up, the phase-field formulation is employed to capture the evolution of the interface between two phases by coupling it with the equations describing the transport of mass and momentum in COMSOL Multiphysics ® v5.3a.

If the equation (2.4) is recalled, Fick's second law describes the movement of species in the direction of concentration gradient over time by combining the first law of diffusion and continuity equation. In spite of its general applicability, the physics of diffusion remains insufficient to elucidate a certain common phenomenon where the components of a uniform immiscible mixture evolve into two distinct water-rich and oil-rich layers while Fickian description of diffusion extrapolates a stable system. Thus, for the case of negative diffusion where liquid-liquid phase separation occurs against the concentration gradient, another driving force must be dominant. The explanation of phase separation can be construed from the minimum energy principle for close systems. Here, for the phase separation case, Cahn and Hillard proposed and validated an isothermal system which the diffusion is dictated by the gradient of the chemical potential [94]. Thus, diffusion flux (J) can be defined by equation (3.6)

where G is the chemical potential (Pa) which is defined as the derivative of total Gibbs free energy density in regard to the concentration ($\partial f/\partial \phi$) and γ is the mobility ($m^3 \cdot s/kg$) analogous to diffusion coefficient.

$$J = -\gamma \nabla G \tag{3.6}$$

In combination with the continuity equation, as an alternate and more general form of Fick's second law, Cahn-Hillard equation (3.7) can be described where the driving force of diffusion is the gradient of chemical potential (∇G) and phase-field parameter $\phi = \pm 1$ represents the concentration of the two components as $(1+\phi)/2$ and $(1-\phi)/2$, respectively.

$$\frac{\partial \phi}{\partial t} = \gamma \nabla^2 G \tag{3.7}$$

The free energy density of a two-phase system can be derived as a function of the concentration (3.8) by neglecting bulk distortion energy and anchoring energy and retaining only Ginzburg-Landau form of the mixing energy for simplicity where λ and f_0 are the mixing energy density (N) and double-well potential (Pa), respectively [95].

$$f_{mix} = \frac{1}{2}\lambda |\nabla \phi|^2 + f_0(\phi) \tag{3.8}$$

In the equation (3.8), first gradient term in the right side represents the interfacial energy due to the local composition at the interface while the second term is the bulk free energy arising the contributions of both homogeneous components. The double well potential which expresses the form of interfacial energy can be written as follows [95] where ε defines the width that scales interfacial thickness (m):

$$f_0 = \frac{\lambda}{4\varepsilon^2}(\phi^2 - 1)^2 \tag{3.9}$$

Hence, the meaning of the equation (3.8) become immediately conspicuous. While f_0 induces a phobic effect and prefers a total separation of bulk components, the interfacial energy describing the weak interactions between the components engenders

a philic effect in the system and prefers a complete mixing. The profile of ϕ arises as a result of the competition between these effects.

Moreover, free energy concept embodies interfacial tension concept naturally and relates the mixing energy density parameter (λ) and the capillary width scaling interface thickness (ε) to surface tension (σ) through the following equation [95]:

$$\sigma = \frac{2\sqrt{2}}{3}\frac{\lambda}{\varepsilon} \tag{3.10}$$

Additionally, the surface tension force can be evolved from the divergence theorem in the form of a body force as follows [98]:

$$\boldsymbol{F}_{st} = G\nabla\phi \tag{3.11}$$

Finally, by taking convective flux density into account and substituting the equation (3.8) into (3.7), the final form of Cahn-Hillard equation can be described in the following form:

$$\frac{\partial\phi}{\partial t} + \boldsymbol{u}\cdot\nabla\phi = \frac{\gamma\lambda}{\varepsilon^2}\nabla^2\left[-\varepsilon^2\nabla^2\phi + \phi\left(\phi^2 - 1\right)\right] \tag{3.12}$$

As can be seen in the equation above, the Cahn-Hilliard equation is a 4th-order nonlinear partial differential equation (PDE). In COMSOL Multiphysics, the phase field interface implementation decomposes the Cahn-Hilliard equation into two coupled second-order PDEs in order to eliminate the difficulties with representation of high-order spatial derivatives which discontinuities occur across element boundaries [99]. These two PDEs can be written as follows where ψ is the phase field help variable:

$$\frac{\partial\phi}{\partial t} + \boldsymbol{u}\cdot\nabla\phi = \nabla\cdot\frac{\gamma\lambda}{\varepsilon^2}\nabla\psi \tag{3.13}$$

$$\psi = -\nabla\cdot\varepsilon^2\nabla\phi + \phi\left(\phi^2 - 1\right) \tag{3.14}$$

The mobility parameter γ establishes the time scale of the Cahn-Hillard equation and the relaxation time of the interface [95]. In this equation, the mobility is a phenomenological parameter that describes the empirical relationship consistently with fundamental theory; however, it should be predicted during calculations because it cannot be derived numerically. The mobility must be selected appropriately large to retain a constant interface thickness but appropriately small to circumvent overly damped convective terms [60]. In COMSOL Multiphysics, the mobility is proportional to the square of interfacial width and scaled with the mobility tuning parameter χ (m·s/kg).

$$\gamma = \chi\varepsilon^2 \tag{3.15}$$

Moreover, velocity and pressure fields is computed by using incompressible Navier-Stokes equation (3.16) and the continuity equation (3.17) where ρ is the fluid density (kg/m^3), $\boldsymbol{u}$ is the velocity vector (m/s), p is the pressure (Pa), $\boldsymbol{I}$ is the unit diagonal matrix, μ is the fluid dynamic viscosity (Pa·s), $\boldsymbol{F}_{st}$ is the surface tension force per unit volume (N/m^3), and $\nabla\boldsymbol{u}+(\nabla\boldsymbol{u})^T$ denotes strain-rate tensor.

$$\rho\frac{\partial \boldsymbol{u}}{\partial t} + \rho(\boldsymbol{u}\cdot\nabla)\boldsymbol{u} = \nabla\cdot\left[-p\boldsymbol{I} + \mu\left(\nabla\boldsymbol{u} + (\nabla\boldsymbol{u})^T\right)\right] + \boldsymbol{F}_{st} \tag{3.16}$$

$$\rho\nabla\cdot\boldsymbol{u} = 0 \tag{3.17}$$

The density and the dynamic viscosity of the two components at any grid can be computed by employing the two equations given below where ρ_c and ρ_d are densities (kg/m^3) of the continuous phase and dispersed phase and μ_c and μ_d are dynamic viscosities (Pa·s) of the continuous phase and dispersed phase, respectively. Assume $\phi = -1$ corresponds to dispersed phase and $\phi = +1$ corresponds to continuous phase.

$$\rho = \frac{1}{2}\left[(1-\phi)\rho_d + (1+\phi)\rho_c\right] \tag{3.18}$$

$$\mu = \frac{1}{2}\left[(1-\phi)\mu_d + (1+\phi)\mu_c\right] \tag{3.19}$$

Due mainly to high computational demand which appears in 3D models, droplet break-up is examined quantitatively by 2D junctions using the phase-field method for segmented flows as well. Simple 2D models are lacking in presenting correct flow results because the top and bottom wall boundaries are excluded despite their significant effect on the flow construction. To account for these effects, in COMSOL, shallow channel approximation can be used when the thickness of the rectangular channel is much smaller than the channels' width ($w \gg h$). The approximation directly adds an extra drag term representing the pressure drop due to the resistance of parallel wall boundaries to the Navier-Stokes equation in the form of equation (3.20) where μ is the dynamic viscosity, $\boldsymbol{u}$ is the flow velocity and h is the thickness of the channel [100].

$$F_{\mu} = -12\frac{\mu \boldsymbol{u}}{h^2} \tag{3.20}$$

The term can be included in the model by using the presented automatic utility or be manually incorporated into the model as a volume force. The approximation corresponds to a hydraulic channel resistance scaled by the channel length (L) for an infinite parallel plate channel. Thus, by implementing manually, the term can be reformulated in accordance with hydraulic channel resistance [101] at different aspect ratios $(AR = w/h)$ by using the equation (3.21). For instance, for AR=1 and AR=4, the approximation term evolves to -28.4542$\mu\boldsymbol{u}/h^2$ and -14.2444$\mu\boldsymbol{u}/h^2$.

$$R_H = \frac{12\mu L}{wh^3\left[1-\frac{h}{w}\left(\frac{192}{\pi^5}\sum_{n=1}^{\infty}\frac{1}{(2n-1)^5}\tanh\left(\frac{(2n-1)\pi w}{2h}\right)\right)\right]} \tag{3.21}$$

The accuracy of 2D case which is implemented according to shallow channel approximation will be evaluated by the results of 3D simulations of segmented flows.

3.5. Boundary Conditions and Simulation Setup

To study the droplet formation, the properties of the fluids which are used in simulations were set to the values of distilled water as dispersed phase and fluorinated oil (HFE-7500, 3M) with %2 (w/w) fluorosurfactant (PicoSurf ®, Dolomite) as continuous phase. The dynamic viscosity and the density are assumed as 1 mPa·s and 1000 kg/m^3 for distilled water, and 1.24 mPa·s and 1614 kg/m^3 for the fluorinated oil respectively. Moreover, the interfacial tension between the oil and the distilled water was assumed as $\sigma = 5$ mN/m for numerical simulations in the presence of surfactant molecules [102].

The boundary conditions are defined as laminar inflow at the inlets with the flow rates of Q_d and Q_c for dispersed and continuous phases respectively and zero pressure at the outlet. The entrance length, L_e, is calculated with respect to equation (2.7) in order to ensure the flow is fully developed.

For channel walls being in contact with fluid-fluid interface, wetted wall condition is implemented to move the interface along the wall. COMSOL adopts a geometric formulation of wetting condition to simulate contact line dynamics which mathematically equals to the surface energy formulation; however, it is more efficient and reliable as the surface energy formulation might precipitate an inconsistency between the prescribed (θ_w) and computed contact angle [103]. The equation (3.22) determines the contact line and contact angle while the equation (3.23) species the mass flow as zero across the wetted wall. The equilibrium contact angle is defined as $\theta_w = 45^o$ for all simulations.

$$\boldsymbol{n} \cdot \varepsilon^2 \nabla \phi = \varepsilon^2 \cos\theta_w \left| \nabla \phi \right| \tag{3.22}$$

$$\boldsymbol{n} \cdot \frac{\gamma \lambda}{\varepsilon^2} \nabla \psi = 0 \tag{3.23}$$

Apart from defining boundary conditions, the parameter controlling interface thickness (ε) and mobility tuning parameter (χ) should be selected wisely to obtain

accurate solution of the interface. In order to allow the phase-field variable evolving smoothly, the value of interfacial thickness should be defined at least equal to or greater than half of the upper limit of the element size. In the simulations, the mesh size is defined as $0.05L$, and correspondingly, the value of ε is selected equal to this. Moreover, the value of mobility tuning parameter can be determined according to the principal criterion for the sharp-interface limit that ensures the numerical convergence both in the bulk components and on the wall surface [104] after defining the interfacial thickness parameter by using (3.24). The Cahn number (Cn) and S represent the dimensionless interfacial thickness and bulk diffusion of the fluids at the interface. Cn_c is the critical Cahn number that denotes the lower limit of the mobility for numerical convergence. According to this criterion, for ε=$0.05L$, the corresponding value of mobility tuning parameter (χ) is approximately 57 m·s/kg. It is important to remark that this value only indicates the lower limit; however, the real value of the mobility parameter leans on the actual physical system.

$$Cn = \frac{\varepsilon}{L}, \qquad Cn_c = 4S, \quad \text{and} \quad S = \frac{\sqrt{M\mu_c\mu_d}}{L} \tag{3.24}$$

For 2D case, the model geometry is meshed by regular grids apart from the triangular elements that define sloping edges after the orifice (Figure 3.4). The same mesh is defined at the top boundary of the 3D model geometry, and using the swept mesh functionality, cubic mesh elements were generated along the straight sections which defines the channel height, 50 μm. To reduce the computational demand, only a quarter of the entire 3D domain is simulated because both the microchannel geometry and flow patterns are completely symmetric with respect to these sliced boundaries. Thus, the symmetry boundary condition is defined for both symmetric faces in the 3D domain. Initial mesh size which will be used on the comparison study between 2D and 3D models is selected in accordance with COMSOL guideline which the mesh size should be at least ten times lower than the expected droplet size [105]. However, after the comparison study, a detailed mesh independence study is conducted for 2D model.

Default study settings of COMSOL is used for both 2D and 3D models. Here, as a piece of complementary information, the evolution of the interface always depends on its history; thus, a time-dependent study is defined with a phase initialization study. Moreover, since both physics, namely laminar flow and the phase field are closely intertwined, two-way coupling with a fully coupled solver which considers all variable couplings at the same time is preferred.

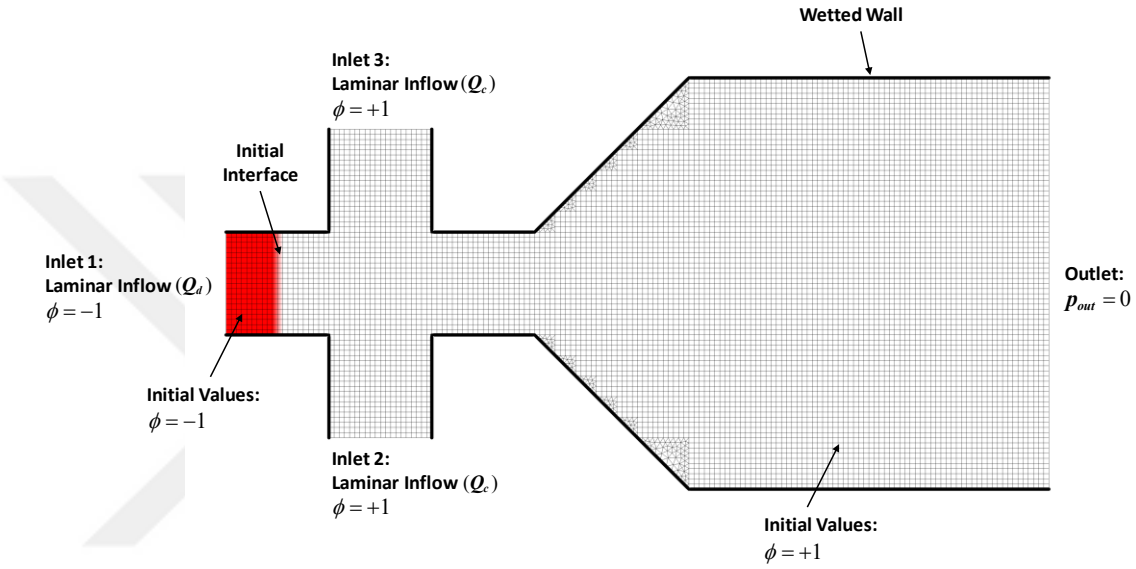

Figure 3.4. Mesh details and boundary conditions used in 2D COMSOL model.

During the simulations, the quantification of droplet diameter is appreciable to determine the operation range of the device. Thus, the effective droplet diameter which based on the area on a virtual surface that longitudinally slices the geometry in the middle is denoted by the equation (3.25). As a figure of merit in the 3D models, apart from a volume correlation, the area which can be seen from top-view is preferred in order to be able to draw a comparison between the laboratory experiments and 2D simulation results more conveniently. Moreover, the formation frequency arises from the ratio of average drop velocity to distance between two consecutive droplets.

$$d_{eff} = 2\sqrt{\frac{1}{\pi}\int_{\Omega}(\phi < 0.5)d\Omega} \tag{3.25}$$

3.6. Simulation Results and Discussions

The intention is to study the emulsification process to accurately describe and eventually elucidate the droplet diameter and the formation frequency for a wide range of dispersed and continuous flow rates at several ratios.

A representative result for 3D model is illustrated in Figure 3.5. Here, flow rates of dispersed and continuous phases are defined as 5 µl/min and 30 µl/min, respectively. For this parameter set, droplets with an effective diameter of 42.507 µm is generated at ~1 kHz in dripping mode.

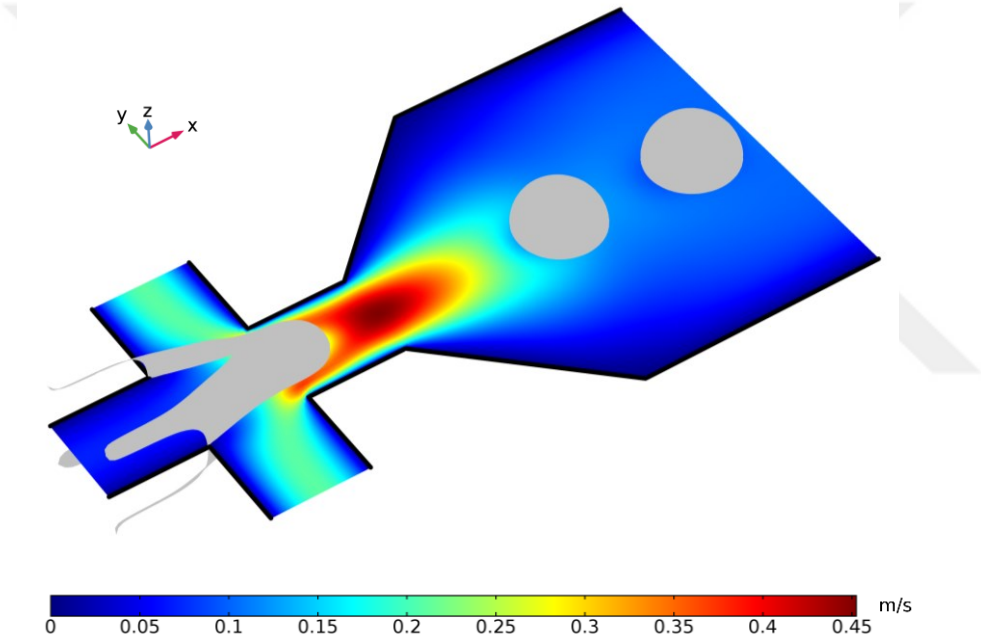

Figure 3.5. COMSOL Simulation of droplet generation in a 3D flow-focusing junction. The flow rates of dispersed and continuous phases are 5 µl/min and 30 µl/min, respectively. Surface plot represents the velocity field and the contour plot depicts the interfacial film.

However, as mentioned in the previous section, capturing the interface and resolving the flow fields in a 3D model is computationally demanding and necessitates several hours for only a single parameter set, although linear elements are used for all relevant variables. Therefore, a 2D simulation model is implemented for the same parameter set by keeping the mesh size and discretization settings unchanged. The computation

time is substantially declined from days to a few hours. The result of 2D droplet break-up is depicted in Figure 3.6. The obtained flow velocity in 2D model corresponds to an averaged flow velocity of 3D model along the z-direction. 2D break-up model shows remarkable consistency with 3D results pertaining to droplet size and formation frequency. In 2D case, the effective droplet diameter and generation frequency are calculated as 42.728 µm and ~1 kHz. The relative error for effective droplet size is obtained as 0.52%. Thus, for succeeding simulations pertaining to emulsification, 2D simulation setup is preferred, because the influence of a wide range of flow values to the break-up can be investigated in an acceptable amount of time thanks to its relatively low computational load. Moreover, it also enables the utilization of quadratic elements and denser mesh structures.

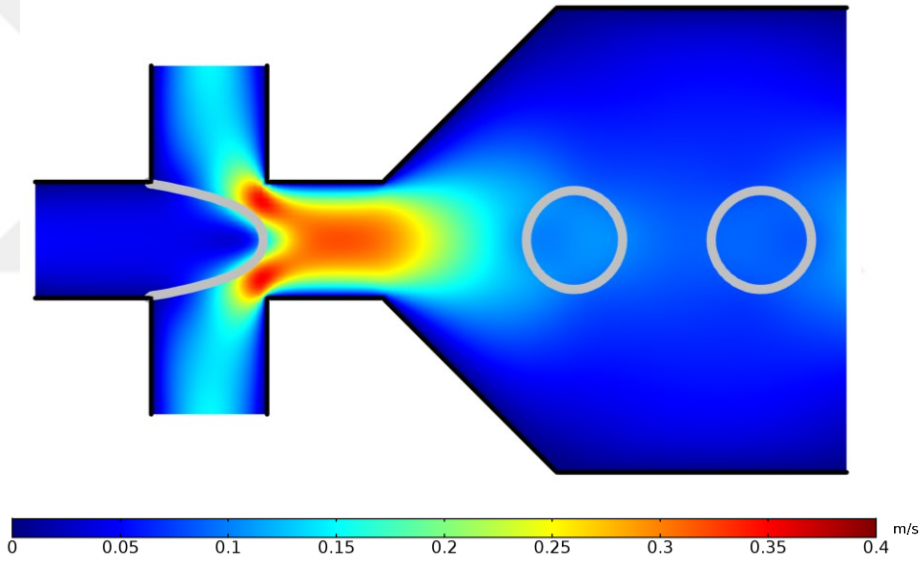

Figure 3.6. COMSOL Simulation of droplet generation in a 2D flow-focusing junction. The flow rates of dispersed and continuous phases are 5 µl/min and 30 µl/min, respectively. Surface plot represents the velocity field and the contour plot depicts the interfacial film.

Prior to parametric analysis pertaining to both phases flow rates, a mesh convergence study is conducted to evaluate mesh independence of 2D problem where $Q_d = 5$ µl/min and $Q_c = 30$ µl/min. The influence of the grid size is investigated by increasing it from $h = 0.2L$ (coarsest) to $h = 0.025L$ (finest). Table 3.1 summarizes the results of the convergence study based on the mesh dependency of effective droplet

diameter. The relative error is measured from the deviation between current and subsequent mesh resolutions. A reasonable error value which is calculated as 0.67% is obtained at $h = 0.05L$. Thus, the grid size of $0.05L$ is decided as the optimal resolution and used in the following studies.

Table 3.1. *Mesh convergence analysis based on the grid size dependency of effective droplet diameter.*

Grid Size (µm)	**Number of Elements**	**Effective Droplet Diameter (µm)**	**Relative Error%**
$0.2L$	800	75.36	40.56
$0.1L$	2446	53.62	27.28
$0.05L$	8712	42.12	**0.670**
$0.025L$	32484	41.84	

Moreover, several simulations are performed to explore the effect of phenomenological mobility by varying mobility tuning parameter (χ) which all satisfy the numerical convergence criterion presented in equation (3.24) while keeping parameter controlling interface thickness constant (ε=$0.05L$). Figure 3.7 shows the droplet formation results for different mobility values. It can be observed that droplets become larger while increasing the mobility tuning parameter; thus, the value of mobility is very critical for the evolution of the system.

However, there is no explicit way to reveal the real physical value of the mobility numerically as mentioned earlier. Here, the value of this phenomenological parameter can be rationalized by comparing with the experimental findings. Once settled, this value can be used in the simulations with different flow conditions. The diameter of the droplets is measured approximately 43 µm in the initial experiments regarding same flow conditions; consequently, the characteristic value of the tuning parameter (χ) reflecting the real process is determined roughly as 570 m·s/kg.

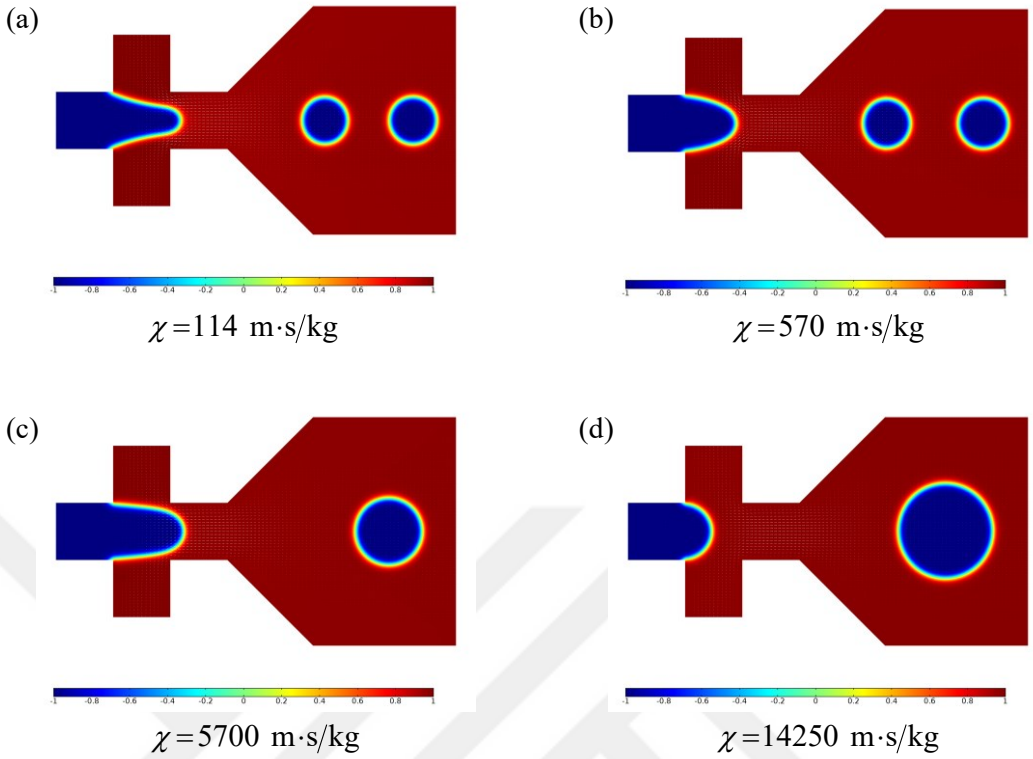

Figure 3.7. The 2D schematics of droplet break-up numerically calculated for four different values of mobility (a-d). The interfacial parameter is fixed to 0.05*L*. The flow rates of dispersed and continuous phases are 5 µl/min and 30 µl/min, respectively. The white arrows indicate the direction of the flow.

After completing preceding studies pertaining to mesh size and phenomenological mobility, several simulations are conducted to analyze the effect of the flow rates of dispersed and continuous phases to the emulsification process. Figure 3.8 graphically shows the effective droplet diameter and generation frequency with respect to the Capillary number of the continuous phase for different flow ratios.

Concisely, according to simulation results, almost spherical monodispersed droplets with an effective size around 40-60 µm can be obtained at a high formation rate (>1 kHz) for several parameter couples. Since expected droplets incorporate a volume of more than 33 pl, it is expected that they will contain a sufficient amount of media content to support cell cultivation for at least 2 days or more [106].

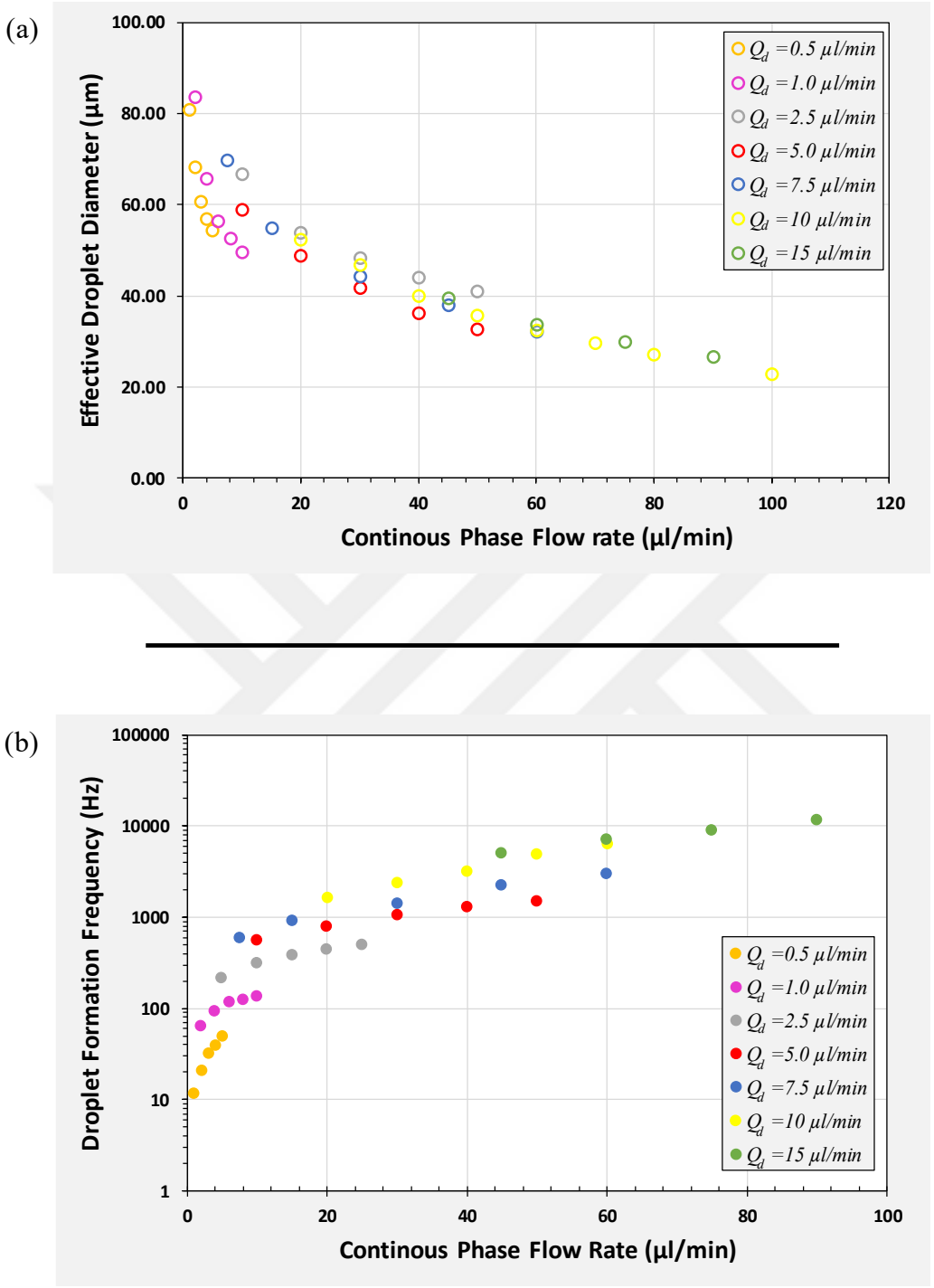

Figure 3.8. Numerical results regarding droplet break-up process. (a) Effective droplet diameter as a function of the continuous phase Capillary number. (b) Droplet formation frequency as a function of the continuous phase Capillary number. The marker colors correspond different flow rate values of the dispersed phase (Q_d).

CHAPTER 4

INERTIAL CELL ORDERING FOR ENRICHMENT OF SINGLE CELL ENCAPSULATION

The necessity to study single cells arises from the heterogeneous behaviors of genetically identical cells; thus, bulk experimentations only produce an average population behavior and remains insufficient to reveal cell-to-cell variability which holds a paramount significance in cancer research. Referring to the previous chapter, droplet-based systems have been utilized in several biological and chemical research applications. Moreover, the encapsulation of cells in droplets also facilitates many quantitative studies by allowing high-throughput single-cell experimentation and analysis. While the droplet microfluidics serves a great potential by enabling the confinement of cells in chemically isolated tiny vessels in a high-throughput manner, the technology is confronted with an intrinsic barrier that the process of loading cells into droplets is completely stochastic whose distribution is dictated by the Poisson statistics. Therefore, the occurrence of a droplet containing k cells can be determined by the following equation where λ is the average number of cells per drop.

$$P(\lambda;k)=\frac{\lambda^{k}e^{-\lambda}}{k!} \tag{4.1}$$

The value of λ can be adjusted by altering the cell density in the suspension medium. The important aspect here is the prevention of the occurrence of the drops which has more than one cell because they will corrupt the desired single cell information and result in misleading results. To minimize the number of droplets which encapsulates more than a single cell necessitates a considerable reduction in cell loading density. For instance, if droplets containing more than one cell are constricted to occupy no more than one in ten of all droplets, the expected ratio of drops containing a single cell

is around 31%. If the occurrence of droplets which has more than one cell is further reduced to one in a hundred, the ratio of usable droplets decreases to approximately 13%. Although the probability of drops holding two or more cells can be minimized by relying on only the Poisson distribution, the majority of the obtained droplets are empty which again restricts the number of usable drops, so the efficiency of high-throughput encapsulation is substantially diminished due to this randomness. Here, efficient and versatile methods for enrichment of the single cell encapsulation are necessary to render Poisson statistics an inconsiderable issue.

In this chapter, initially, the current state of art aiming to overcome this intrinsic impediment will be introduced. After presenting a short literature review, to be able to present a robust and versatile solution to circumvent the Poisson distribution in single-cell encapsulation without the assistance of externally applied fields, the principles of microfluidic inertial focusing will be elaborated. Thus, the fundamentals of inertial microfluidics will be covered by defining several forces acting on a particle in a microfluidic channel to be able to understand the dynamics of particle ordering. Then, a direct numerical simulation (DNS) study will be implemented to accurately calculate the total lateral force on a particle in straight rectangular channels of different aspect ratios using COMSOL Multiphysics ® v5.3a. The obtained lift force will be interpolated to several types of microchannels with the same rectangular cross-section to reveal the expected particle trajectories. Finally, the decision of a specific channel geometry which facilitates the self-ordering of the particles will be made to be inserted in the design of the full droplet workflow in order to enhance single cell encapsulation efficiency.

4.1. A Short Literature Review of the Current State of Art

In order to circumvent this serious hindrance to efficient cell encapsulation, several approaches have been presented in literature, mainly including sorting after generating the drops and inertial ordering of the cells before generating the drops.

One common way to acquiring high purity droplets containing single-cells is to separate them from the vast majority of which are containing no cells after realizing the drops with a cell loading density. Post-encapsulation sorting can be achieved by active methods including sorting by dielectrophoresis [25], [107], [108], acoustic fields [109], magnetic [13] or optical forces [110], and purely hydrodynamic passive methods such as deterministic lateral displacement (DLD) [111] and shear-induced migration [112]. Active forces such as dielectrophoretic or acoustic forces provide flexibility where any kind of measurable quantity such as fluorescence activation or droplet density can be used for post-encapsulation sorting of the drops. As illustrated in Figure 4.1 (a), droplets can be sorted by dielectrophoresis by measuring the fluorescence activation representing the enzymatic activity inside them [108]. Moreover, by utilizing continuous standing surface acoustic waves (Figure 4.1 (b)), Nam et al. are achieved to sort the alginate droplets with respect to the encapsulated quantity of cells, where the drops encapsulating more cells migrates more quickly thanks mainly to their respective higher densities [109]. Hydrodynamic approaches such as DLD or shear-induced migration relies on the obtained droplet size where the size of droplets containing one or more cell is respectively larger while operating in jetting mode (Figure 4.1 (c)-(d)).

Despite increasing the efficacy by increasing the purity, the post-encapsulation sorting methods are restricted by the randomness where cells initially are encapsulated, so the volume of the majority of the drops which contain no cell is being wasted; thus, the throughput is reduced by at least one order of magnitude [113]. Additionally, active approaches need sophisticated equipment and mostly extensive input from the user. One way of beating the Poisson distribution is to use a double junction configuration where the first junction adds spaces between close-packed particles before arriving at the second junction introducing oil to generate droplets [114]. However, the close packing might cause a blockage in the channels and increases the operating pressure of the device.

Additionally, a preeminent solution is to order cells by using the principles of inertial microfluidics before arriving in droplet junction. In microchannels, mainly, the balance between shear gradient lift force repelling particles away from the centerline due to the parabolic velocity field and wall-induced lift force pushing particles away from the wall causes self-organization of the particles in specific equilibrium positions. By using this principles Edd et al. achieve the ordering of the cells in a high aspect ratio straight microchannel laterally in either side of the microchannel circumvent the Poisson distribution with about 80% single-cell encapsulation ratio by precisely tuning the cell loading.

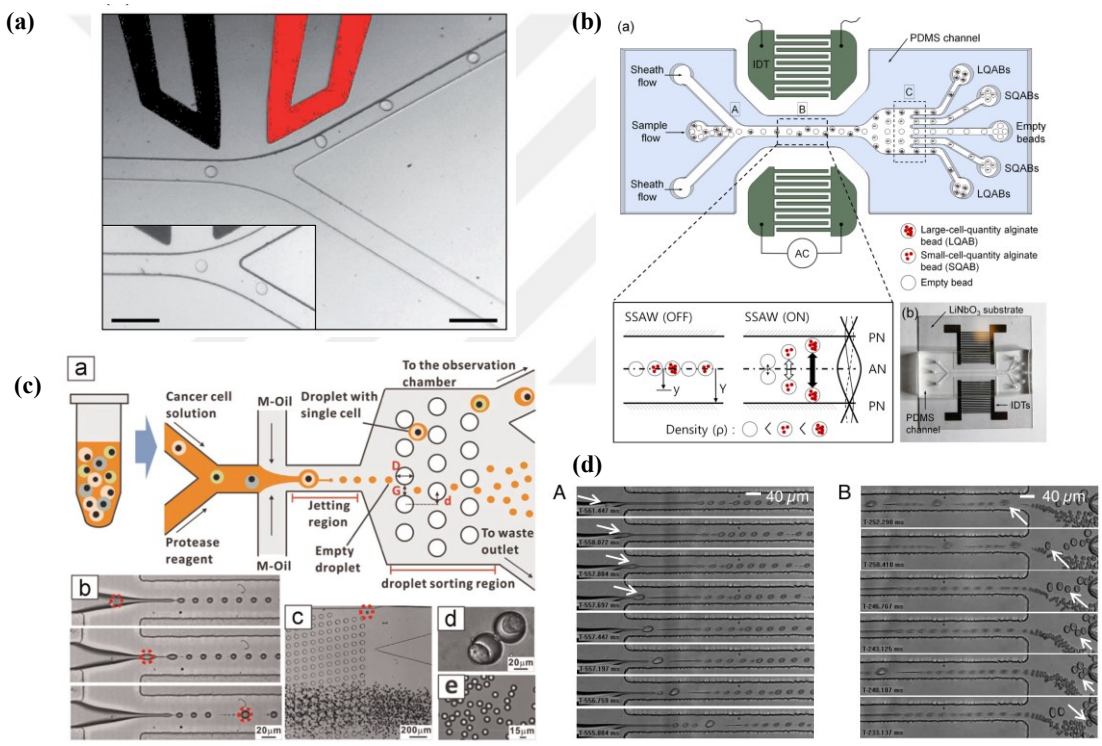

Figure 4.1. Droplet sorting methods presented in the literature. (a) Dielectrophoretic separation triggered on droplet fluorescence [25]. (b) Size-based sorting of drops by the DLD micropillar channel [111]. (c) Density-based droplet sorting by surface acoustic wave based acoustophoresis [109]. (d) Hydrodynamic sorting of droplets by shear-induced migration [112].

Moreover, a more robust approach for deterministic cell encapsulation is to ensure focusing of cells into a single line by introducing an additional inertial effect, namely Dean flow, resulting from the curved channel geometry [115].

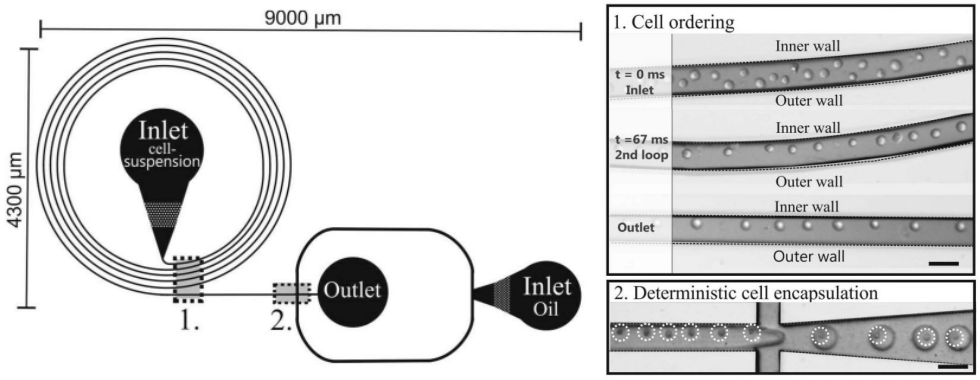

Figure 4.2. Inertial ordering using curved channels for deterministic single cell encapsulation [115].

Apart from the easy implementation and robustness, due mainly to providing a more pre-eminent way to handling the stochastic encapsulation process by increasing the throughput, the inertial ordering of cells will be the focus of this chapter to eventually design a microchannel geometry facilitating deterministic single cell encapsulation. In the next, the essential forces acting on particles in microchannels will be covered to illuminate the theory behind the inertial focusing phenomenon.

4.2. Forces Acting on Particles in Microchannels Flows

The motion of a particle in a flow is managed by the force exerted by the fluid integrating the pressure and viscous stress. This nonlinear total force might be divided into two distinct contributors, including viscous drag that is parallel to the direction of the flow and lift force that is perpendicular to the direction of the flow.

4.2.1. Viscous Drag Force

The primary viscous drag force compels an acceleration on particles to follow the streamlines along mainstream direction until they reach the same velocity with the fluid (Figure 4.3). The viscous drag on a moving small spherical particle in a flow can be expressed at low particle Reynolds numbers using the Stokes' drag equation (4.2) where μ is the fluid dynamic viscosity (Pa·s), a is the particle diameter (m), $\boldsymbol{u}$ is the mainstream fluid velocity and $\boldsymbol{u_p}$ is the particle velocity in mainstream direction (m/s). However, the viscous drag force shows a significant correlation with the associated

relative Reynolds number (Re_r), so the force formula might be corrected if it is necessary [116].

$$F_D = 3\pi\mu a\left(\boldsymbol{u} - \boldsymbol{u}_p\right) \tag{4.2}$$

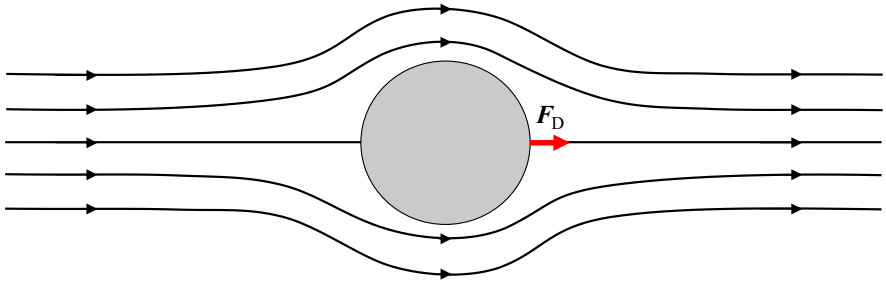

Figure 4.3. Schematic illustration of viscous drag force.

Moreover, apart from the drag force in the mainstream, there is a secondary drag force dictated by the secondary flow, namely Dean flow, set up perpendicular to the main direction of the flow due to the curvature of microchannel path. More elaborately, the reason behind the formation of Dean flow originates from conservation of momentum where recirculation of fluid occurs when excess momentum of faster-moving fluid in the center moves it towards to outer wall of curvature [117]. Stokes' drag equation can also be used for the calculation of secondary drag force for appropriate Reynolds numbers. Dean flow is a practical tool for controlling and restricting the number of equilibrium particle positions within the cross-section of the microchannel.

4.2.2. Lift Force

Moreover, the lift force leads the particles to laterally migrate toward the specific positions which have a considerably complicated dependence on particle size, flow conditions, and channel geometry [117]. Thus, in order to be able to design microfluidic devices for inertially manipulate particles, the lift force exerted on the particles should be accurately estimated to extrapolate the equilibrium particle positions in the channel cross-sections. The inertial lift force embodies four distinctive terms, namely wall-induced lift ($\boldsymbol{F}_{WI}$), shear-gradient lift ($\boldsymbol{F}_{SG}$), slip-shear lift ($\boldsymbol{F}_{SS}$), and the Magnus force ($\boldsymbol{F}_{\Omega}$). In addition to four components of lift force, there is

another viscous drag force observed in transverse direction due to secondary flows induced by the curvature of the channel, which is known as Dean flow. The secondary drag force is also a significant tool for manipulation of equilibrium particle positions in microchannels.

4.2.2.1. Magnus Force

In a laminar flow, if the particle is travelling in the upper half of the channel, it is clear that the velocity at the lower part of the particle will be higher than the velocity at the upper part due to the parabolic form of velocity field; thus, this will induce a rotation effect to the particle. Being consistent with the Bernoulli's theorem, this will create a pressure imbalance at the sides of the particle, because the rotation induces a reduction in pressure where the rotation is inclined to raise the velocity of the fluid. Hence, this indeed induces a lift force acting to move the particle towards to channel center which is called as rotation induced lift force or Magnus force (Figure 4.4).

The rotation induced lift force exerted on a spherical particle in a microchannel can be calculated by using the following formula where a is the particle diameter (m), ω is the angular velocity (rad/s), $\boldsymbol{u}$ and $\boldsymbol{u}_p$ are the fluid velocity (m/s) and particle velocity (m/s), respectively.

$$\boldsymbol{F}_\Omega = \frac{1}{8}\pi a^3 \left(\boldsymbol{u} - \boldsymbol{u}_p\right) \times \boldsymbol{\omega} \tag{4.3}$$

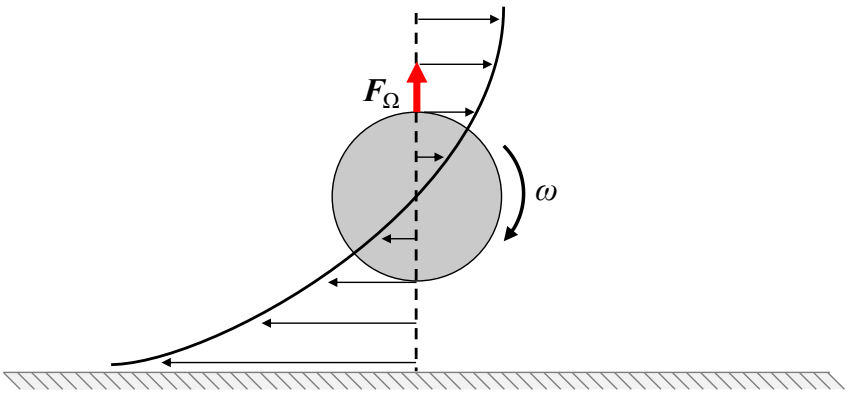

Figure 4.4. Schematic illustration of Magnus force.

4.2.2.2. Slip-Shear Force

In a bounded flow, the occurrence of channel walls generates a velocity gradient, so a shear rate. The extra drag created by the walls causes the particles to lag behind the fluid or lead the fluid according to the lateral position of the particle. This slip-shear motion will create a lateral force on the particles named as Saffman force or slip-shear force due to velocity difference between either side of the particle and also depends on the relative velocity between the particle and the fluid which sometimes can be called as lag or slip velocity.

It should be noted that this force emerges from the interplay between Stokeslet velocity field created by the neutrally non-buoyant particles and simple shear velocity is totally independent of the rotational motion at relatively low Reynolds number (Re<6600) because slip-shear component of the lift force is at least one order of magnitude more than the rotation induced lift force [118]. Unless the rotation velocity of the particle is much higher than the shear rate, these two components can be considered separately and straightforward superposition of these two components remains valid.

For a shear flow, if the particles are heavier than the fluid, they lag the flow and migrate towards the centerline of the channel; conversely, if they are lighter than the fluid, they lead the flow and migrate toward to walls (Figure 4.5).

Saffman calculated the magnitude of this component of lift force on a spherical particle flowing in a simple unbounded shear flow according to the following formulation where K is numerical constant (~81.2 kg/m·s), a is the particle diameter (m), γ is the shear rate (1/s), v is the kinematic viscosity (m^2/s), $\boldsymbol{u}$ and $\boldsymbol{u}_p$ is the velocity of fluid and the particle (m/s), respectively [119].

$$\boldsymbol{F}_{SS} = \frac{K}{4}\left\|\boldsymbol{u}_p - \boldsymbol{u}\right\| a^2 \sqrt{\gamma / \nu} \tag{4.4}$$

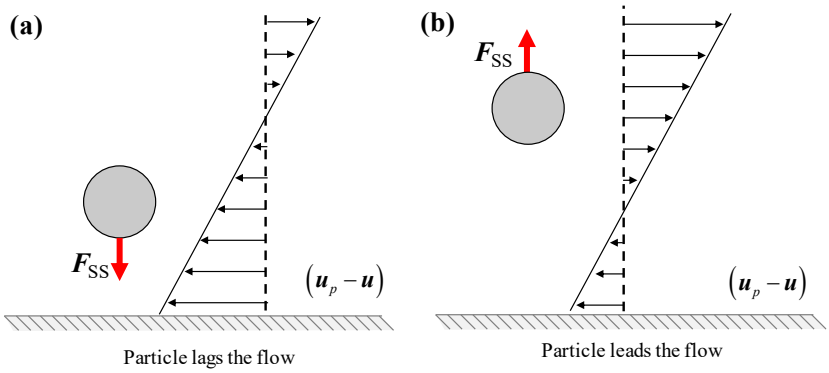

Figure 4.5. Saffman force exerted on a rigid sphere in a simple shear flow. The fluid velocity is zero for the streamline going through the center of the particle. The arrow lines represent to the relative velocity of particles to the flow. (a) The case which is pertinent to heavier particle. (b) The case which is pertinent to lighter particle.

4.2.2.3. Wall-induced Lift Force

If a particle flows in a microchannel, it interacts with the walls, unless it is extremely small. This interaction exerts a force component on the particle which causing them to migrate away from the microchannel walls because of the lagging impact of the walls on particle and the pressure building on the constriction between the particle and the walls (Figure 4.6). As expected, wall-induced force is inversely proportional with the normalized length between the particle and the wall [120]. Particularly, when a particle approaches to the wall, the streamlines of the fluids are diverted in the direction of the side away from the channel wall and leads to lower pressure on this side in comparison with the wall side, which eventually creates the lift force. The regarding schematic of the streamlines when the particle is close to the wall is depicted in Figure 4.6.

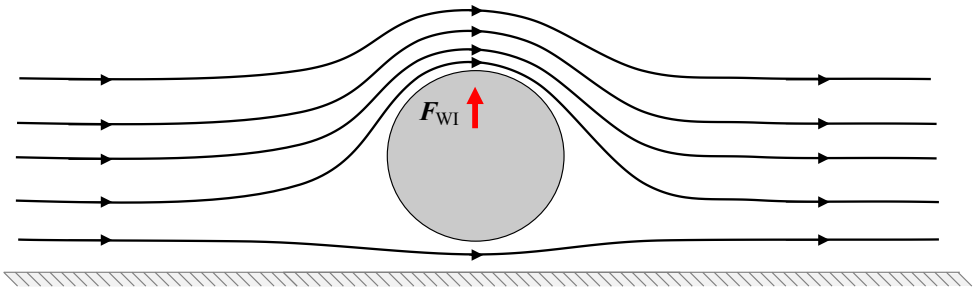

Figure 4.6. Schematic illustration of wall-induced lift force.

The following equation denotes the scaling of the wall-induced lift force where ρ is the fluid density (kg/m^3), U_m is the maximum fluid velocity (m/s), a is the particle diameter (m), D_h is the characteristic channel length, and C_{WI} is the lift coefficient that depends on position and Reynolds number [121].

$$\boldsymbol{F}_{WI} = C_{WI}\rho U_m^2 \frac{a^6}{D_h^4} \tag{4.5}$$

4.2.2.4. Shear-Gradient Lift Force

If a particle flows through a microchannel, it will also be subjected to a force arises from the curvature of the parabolic profile of the velocity (Figure 4.7). The relative velocity of fluid with respect to the particle is substantially larger in magnitude at the bottom of the particle due to the parabolic nature of the flow. Thus, to compensate this difference or shear gradient, the flow induces a lift force on the particle which migrates them in the direction of the particle side with higher velocity, so towards to the wall where dissymmetry in the relative velocity is minimized. This force is opposite to Saffman Force and arises purely from a non-zero gradient in shear due to nature of the Poiseuille flow, not from shear rate due to stokeslets which particles create due to lagging or leading the flow. The following formulation scales the shear-gradient lift force where C_{SG} represents the lift coefficient which highly depends on the lateral position of the particle and Reynolds number [121].

$$F_{SG} = C_{SG}\rho U_m^2 \frac{a^3}{D_h} \tag{4.6}$$

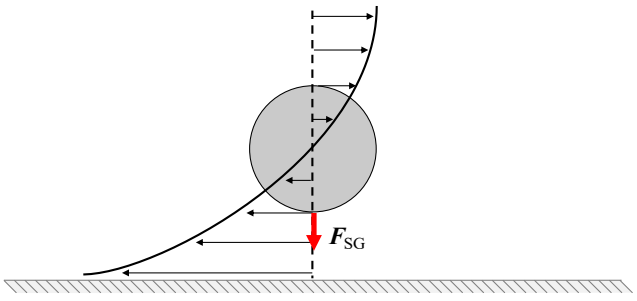

Figure 4.7. Schematic illustration of shear-gradient lift force.

4.2.2.5. Net Lateral Force in Microchannels

In addition to viscous drag force along the mainstream, several lift forces acts on a solid particle flowing through a straight channel or tube, including wall-induced lift force, shear-gradient lift force, rotation-induced lift force, and slip-shear lift force as described in the previous sections. Among them, shear-gradient lift force together with wall-induced lift force is far dominant where it is one order of magnitude higher than slip-shear force and three orders of magnitude higher than rotation-induced lift force [122]. Thus, both slip-shear and rotation-induced lift forces are often negligible for most cases because while wall-induced lift force and shear-gradient lift force scale with the velocity of flow, the latter ones depend on the relative velocity of fluid with respect to the particle. The balance between wall-induced lift force which repels particle away from the walls and shear-gradient lift force which causes particle migrates toward walls determines the equilibrium particle positions and reasonably explains the observations of Segre and Silberberg where particles focus on an annulus with a size of approximately 0.6 times of the radius of the pipe [123].

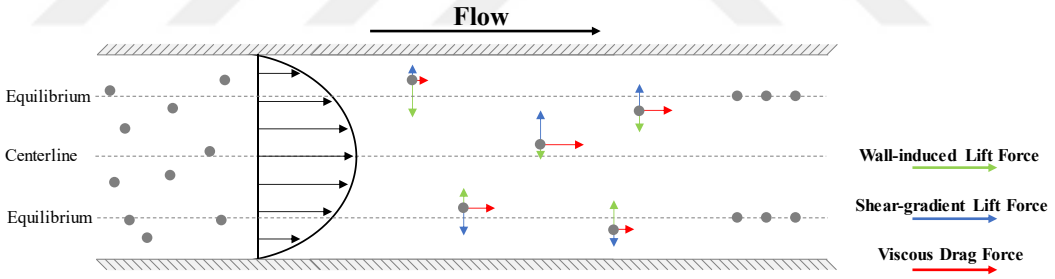

Figure 4.8. Schematic illustration of balance between shear-gradient and wall-induced lift force in a Poiseuille flow.

If a particle moves close to the center of the channel, the shear-gradient-induced lift force dominates the effect of channel walls. However, when a particle drifts close to the channel wall, the wall-induced lift force become stronger. The equilibrium takes place where two forces become equal in magnitude and cancel each other. The schematic regarding mechanism is illustrated in Figure 4.8.

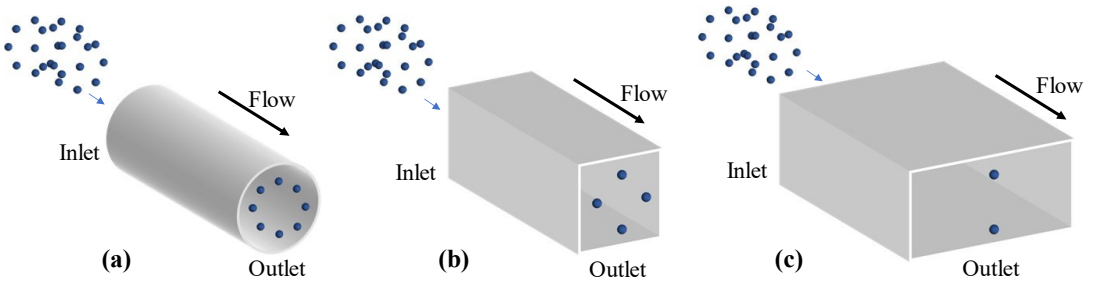

Figure 4.9. Schematics of the stable focusing positions of particles moving through microchannels of different cross-sections [124]. (a) Circular channel. (b) Square channel. (c) Rectangular channel.

In a straight channel, different channel cross-sections engender different final particle equilibrium locations. Figure 4.9 depicts the final equilibrium locations for a circular tube, a square, and a rectangular channel. The balance between wall-induced force and shear-gradient force can nicely explain the final equilibrium positions in a circular channel. Due to axial symmetry, particle accumulates on several equilibrium positions over an annulus where these two force components cancel each other. However, for square and rectangular channels, the ordering becomes more complex. For instance, four distinct positions facing the center of each wall are observed in square channels, while an additional reduction to two particle positions takes place in rectangular channels of low aspect ratio. This formation cannot be explained only by the balance between wall-induced force and shear-gradient force, so there should be additional forces realizing the reduction in the final equilibrium position. For straight channels with square and rectangular cross-sections, actually, the focusing of the particles occurs in two stages (Figure 4.10). In the first stage, the particles form a ring parallel to iso-contours of velocity profile similar to circular channels thanks to the balance between wall-induced force and shear-gradient force. In the second stage, since these forces cancel each other, other lift components, namely slip-shear and rotation-induced lift forces, become predominant in the wall region and force particles to slowly migrate toward the wall-centered locations on this ring where the fluid velocity is maximum [124]–[126]. The second stage of migration takes more time to be realized, because the active force components are at least one order of magnitude smaller than wall-induced force and shear-gradient force. On this point, due to

symmetric shear on two sides of the particle, the component of both slip-shear force and Magnus force which is parallel to the wall will be set to zero while the other component perpendicular to the wall will be further balanced by shear-gradient lift force. Thus, two-stage focusing can reasonably explain the further reduction in equilibrium points seen in square and rectangular channels.

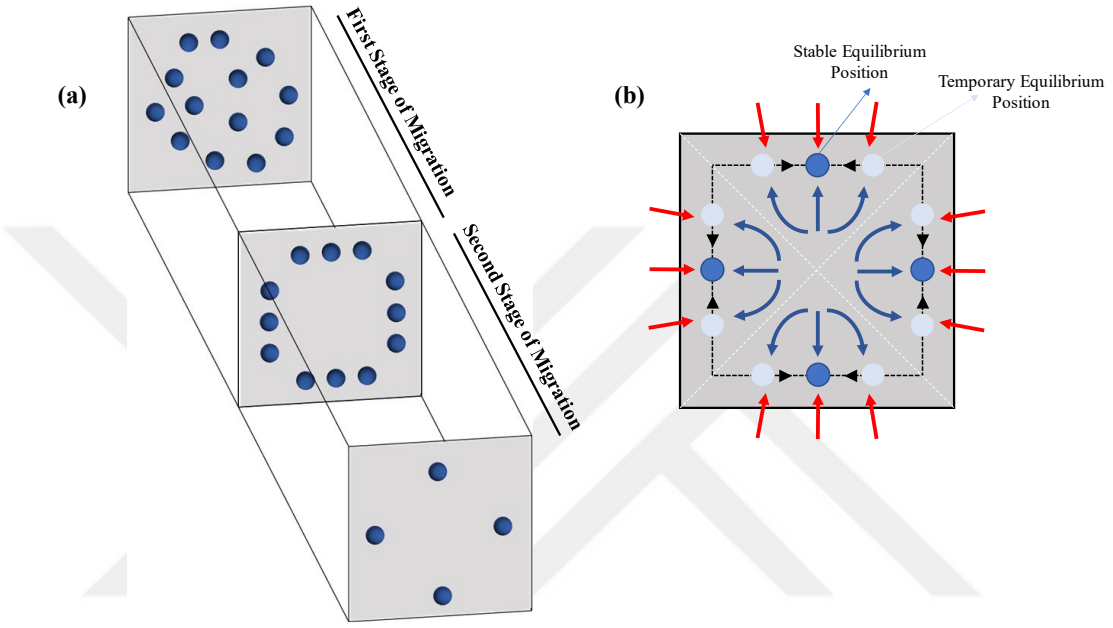

Figure 4.10. Inertial focusing in a square microchannel. (a) Two stages of lateral migration. (b) Stable and temporary equilibrium locations obtained under the effect of lift forces.

The magnitude of the lift force is strongly dependent on the Reynolds number. Inertial microfluidics, in general, operates in a moderate regime corresponds to range ~1<Re<~100 where both the viscous and inertial forces are finite [116]. It also shows a strong correlation with the particle diameter since it will directly influence to total stress on the particle which induced by the fluid. Thus, sometimes, a different number which is called as particle Reynolds number (Re_p) is utilized to scale the inertial flows where Re_c is the Reynolds number of fluid flow, ρ is the fluid density (kg/m^3), U is the mean velocity of fluid (m/s), μ is the dynamic viscosity (Pa·s), D_h is the characteristic diameter (m), and a is the particle diameter (m). In order to provide appropriate inertia on particles, the following definition should be greater than one [117].

$$Re_p = Re_c\left(\frac{a}{D_h}\right)^2 = \frac{\rho U a^2}{\mu D_h} \tag{4.7}$$

Moreover, as mentioned earlier, if a curvature is introduced to the microchannel path, the formation of secondary flows induces another lateral force to the particle, namely secondary drag force. This force is also helpful for controlling and further restricting the number of equilibrium particle positions in microchannels. A schematic illustrating the superposition of secondary drag flow with inertial lift forces in curved channels is illustrated in Figure 4.11. By using curved channels, the number of stable equilibrium locations can be reduced to two locations for a square channel [127]. Moreover, by further controlling the flow condition and the curvature ratio, a single stable equilibrium position can also be obtained [128].

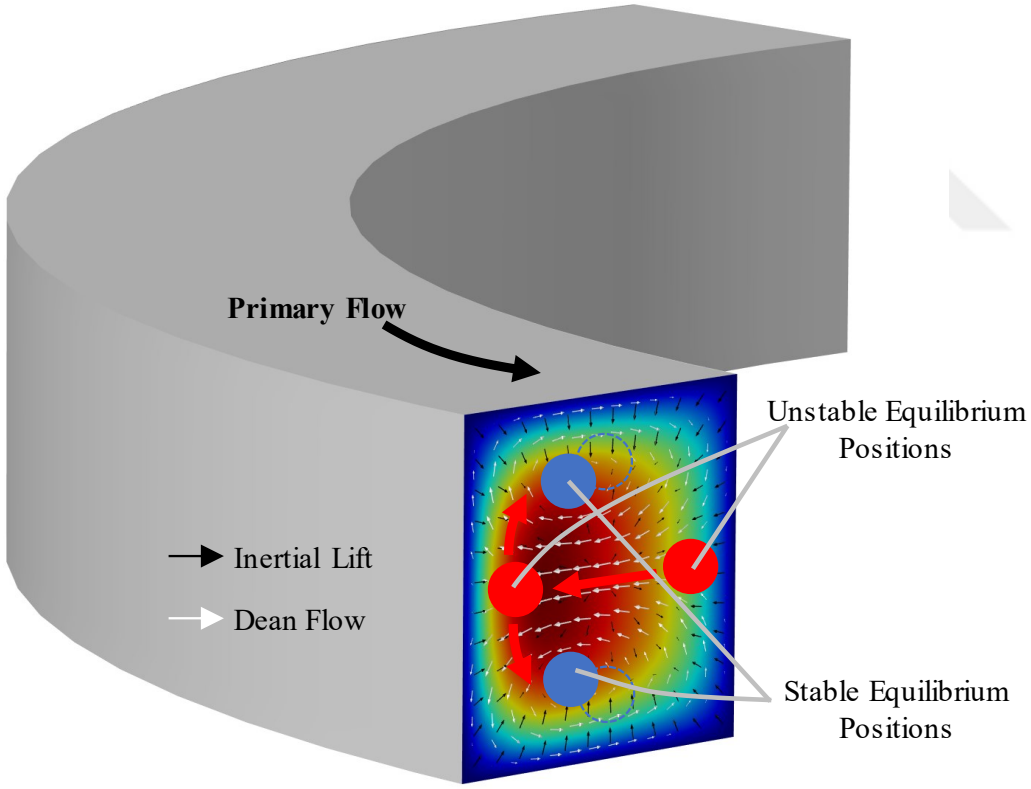

Figure 4.11. Superposition of inertial lift force and Dean vortices illustrated in a curved channel. The flow fields and inertial lift force are computed in COMSOL Multiphysics ® v5.3a.

4.3. Direct Numerical Simulation and Calculation of Spatial Lift Force Field

The mechanism of inertial focusing is elaborated in the previous sections and analytical formulations which estimates relevant forces are presented. With regard to these formulations, the lateral migration of particles complexly depends on the flow conditions, particle size, channel cross-section, and path.

Here, Ho & Leal presented an explicit formula (4.8) which clearly embodies the coupled effect of wall-induced lift and shear-gradient lift force on spherical particles in a two dimensional Poiseuille flow as follows where β is dimensionless shear rate, γ is the dimensionless shear gradient, H is the tube diameter (m), a is the particle diameter (m), ρ is the fluid density (kg/m^3), U_m is the maximum fluid velocity (m/s), G_1 and G_2 are functions of lateral position [122], [126]:

$$F_L = F_{WI} + F_{SG} = \left(\beta^2 G_1 + \beta\gamma G_2\right)\rho U_m^2 \frac{a^4}{H^2} \tag{4.8}$$

Apart from being valid for tube and 2D Poiseuille flows, this formulation imposes the limitation of $Re \ll 1$ and $a/D_h \ll 1$, so cannot be applicable in particle situations where Reynolds number is finite. Later, Asmolov extended the applicable flow range up to Re exceeding 1000 with the prerequisite of $Re_p \ll 1$ by using the method of matched asymptotic expansions, and discover that the equilibrium locations shift closer to the wall while increasing Re [129]. However, both formulations fail to estimate the lateral migration completely for realistic cases where the particle size is finite and induces considerable nonlinearity to the flow. Moreover, the formulations only render results for 2D Poiseuille flows and tube flows, so cannot be used for square or rectangular channels with a low aspect ratio.

Here, direct numerical simulation (DNS) can be utilized to estimate forces acting on particles and the migration of the particles without these restrictions [126], [130]. In DNS, the total hydrodynamic force acting on a particle is computed by integrating the total stress induced by the fluid. It directly encompasses all components of the hydrodynamic force and yields more direct and realistic results for migration.

With regard to analytical explanations presented in previous sections, the lift forces acting on a particle is controlled by a group of dimensionless parameters, so the function which represents the lift force can be written as follows where AR is the aspect ratio of channel which is the proportional relationship of channel width (w) and channel depth (h), κ is the dimensionless particle diameter which is the proportional relationship of particle diameter (a) and characteristic diameter of the channel (D_h), Re_c is Reynolds number of the flow, y' and z' are the relative lateral distances of the particle to the center of channel when the flow direction is aligned with x-axis:

$$\boldsymbol{F}_L = F\left(AR, Re_c, \kappa, y', z'\right); \qquad AR = w/h; \qquad \kappa = a/D_h \tag{4.9}$$

4.4. Model Geometry

In order to extract the lift force, a DNS study is conducted for straight channels with circular, square and rectangular channel cross-sections which are depicted in Figure 4.9 for a wide range of flow conditions. In a straight channel, since there is no secondary flow, the only contribution to the lateral force which migrates particles into specific locations is made by lift force.

The particle diameter is selected as a=10 μm, so κ is held constant during simulations. The diameter of the circular channel and the size of the square channel (h) is determined as 50 μm. For rectangular channels, the aspect ratio means the ratio of width to height. Thus, for rectangular channels with AR=2 and AR=4, the channel widths are defined as 100 and 200 μm, respectively.

The magnitude of the force will differ according to the location where a particle is present at the time. Thus, a series of simulation studies were conducted by changing the lateral particle location to interpolate the lift force spatially by updating the location of the particle in the model geometry. The main flow direction is selected as the x-axis, so the y- and z-components of the extracting force correspond to lift force while x-component defines the viscous drag force.

In previous chapters, both micromixer and the droplet formation model are studied in the microchannels with rectangular cross-sections, thus, the main intention here is again investigating the particle migration in channels with rectangular or square cross-sections. However, the study is initially implemented for a circular channel geometry because extracting the complete spatial lift force field is far practical and faster due to axial symmetry. The lift force can be sampled spatially over a single line segment which corresponds to the radius; then, interpolated to the entire channel by rotating the calculated sample force data. After collecting lift force by covering the entire cross-section, the resulting force field can be inserted into any channel with the same cross-section regardless of channel path to ultimately evaluate the particle migration.

The geometry model is drawn in a way which allows easy and reasonable meshing afterward. First, the particle is created at the origin. Then, a square cross-sectional face which represents the inlet of the channel is defined in a work plane half of the channel length away from the particle. For responding to different particle locations on the channel, apart from sliding particle laterally, the center of the inlet is shifted relative to the particle while keeping particle fixed. Thus, the center of the mass always will be the origin during further calculations. On this plane, also a smaller square whose center is aligned with the particle is defined and overlaps with the larger channel cross-section.

The smaller square never crosses with the channel edges to prevent any problem which can arise during the automatic meshing after re-building the model geometry while doing a parametric sweep evaluating the lateral location of the particle. The work plane is extruded to construct the square microchannel and the particle is subtracted from the resulting square prism.

Moreover, two other work planes are defined on the left and right sides of particle and partitioned with the channel to enclose the particle in a compact way. Finally, unnecessary faces are ignored for physics, but kept for the mesh control. Final geometry of the microchannel for square and circular cross-sections is illustrated in

Figure 4.12 when the particle is located at different lateral positions. The inner prism will be benefitted during defining the mesh. The model geometries of the circular and rectangular channels are created by using the exact same procedure.

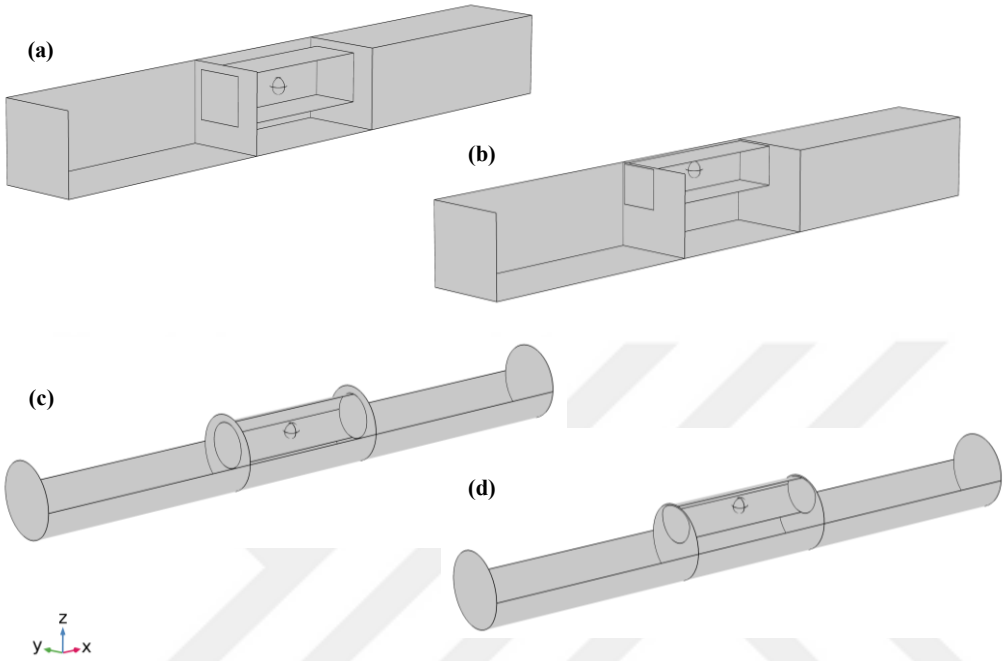

Figure 4.12. Square and circular channel geometry which is created in COMSOL Multiphysics to extract the lift force data. (a) The spherical particle is placed at (y,z)=(0.2h,0.2h). (b) The spherical particle is placed at (y,z)=(0.6h,0.6h). (c) The spherical particle is placed at (y,z)=(0,0.2h). (d) The spherical particle is placed at (y,z)=(0,0.6h). 2h represents the side length of the square channel and the diameter of the circular channel. The centerline of channels (x-axis) passes through the origin. Some of the faces are visually hidden to clearly illustrate the model geometry.

4.5. Numerical Model of Particle Motion

The velocity and pressure fields are computed by using the single-phase, and incompressible Navier-Stokes equation (2.6) and the continuity equation (2.7). After integrating the total stress exerted on the particle by the flow across the particle surface, the translational and rotational motion of the particle under a flow is predicted by directly incorporating Newton's second law in the following forms:

$$m_p \frac{d\boldsymbol{u}_p}{dt} = \int_S \left(-p\mathbf{1} + \boldsymbol{\tau}\right) \cdot \boldsymbol{n} d\boldsymbol{S} \tag{4.10}$$

$$I_p \frac{d\left(\boldsymbol{\Omega}_p\right)}{dt} = \int_S \left(\boldsymbol{r} - \boldsymbol{r}_p\right) \times \left[\left(-p\mathbf{1} + \boldsymbol{\tau}\right) \cdot \boldsymbol{n}\right] \boldsymbol{dS} \tag{4.11}$$

where m_p (kg) and I_p (kg·m^2) are the mass and moment of inertia of the particle, $\boldsymbol{u}_p$ (m/s) and $\boldsymbol{\Omega}_p$ (rad/s) are the translational and rotational velocity of the particle, p is the pressure (Pa), $\mathbf{1}$ is the unit tensor, $\boldsymbol{\tau}$ is the viscous stress tensor acting on the particle (Pa), $\boldsymbol{r}$ and $\boldsymbol{r}_p$ are the position vectors of a point on the particle surface and the center of particle (m), respectively. The moment of inertia of the spherical particle is given as $I_p = m_p a^2/10$ where a is the particle diameter (m).

The equations 4:10-11 are solved by using Laminar Flow Interface in COMSOL Multiphysics ® v5.3a and all axial components of total hydrodynamic force and torque exerted on the particle is computed by using built-in stress variables which corresponds the right sides in the equations 4:12-13, respectively. Since the equations 4:12-13 are ordinary differential equations, they are computed by using Global ODEs and DAEs Interface.

4.6. Boundary Conditions and Simulation Setup

The particle is allowed to rotate freely in all directions but only move along x-axis which is the main direction of the flow. Normally, the stress on the particle results in a net lateral force on the particle which will cause particle to migrate. However, since obtaining this force at a specific location is the primary interest of the simulation study, the motion of the particle is restricted to the main flow direction. Once both translational motion in the x-direction and the rotational motion in all directions are arrived in steady-state, the lift force is determined as the composition of lateral components of the total force on the particle ($\boldsymbol{F}_y$ and $\boldsymbol{F}_z$). Hence, a time-dependent study was defined, and simulation time is selected to assure the system to reach the steady-state.

As boundary conditions of laminar flow model, laminar inflow is defined at the inlet with a constant flow rate which corresponds to a specific Reynolds number, and

laminar outflow with zero pressure condition is defined at the outlet. The entrance length, L_e, is calculated with respect to (2:7) in order to ensure the flow is fully developed. A sliding wall boundary condition is imposed on the particle surface to define the rotation of the particle in correlations with the affecting torques as follows in all three axes:

$$\boldsymbol{u}_r = \Omega_y z - \Omega_z y; \qquad \boldsymbol{v}_r = \Omega_z x - \Omega_x z; \qquad \boldsymbol{w}_r = \Omega_x y - \Omega_y x \tag{4.12}$$

Moreover, a moving wall boundary condition is defined at the channel walls with the velocity $-\boldsymbol{u}$, where $\boldsymbol{u}$ is the particle velocity computed using equation (4.10). By imposing the relative velocity of the wall with respect to the spherical particle, mesh deformation is avoided; thus, the computational load of the model is significantly reduced [131].

First, the inlet boundary is meshed with free triangular elements and copied to other parallel faces. Then, using the swept mesh functionality, triangular prismatic mesh elements are generated along the straight channel. The face of the spherical particle also meshed with free triangular elements. The resulting grid mesh at the faces of the inner square prism is converted to triangular elements and this interior domain meshed with the free tetrahedral elements. The mesh is finalized by defining two boundary layers at the channel walls and also around the particle. Figure 4.13 demonstrates the finalized mesh of the model geometry.

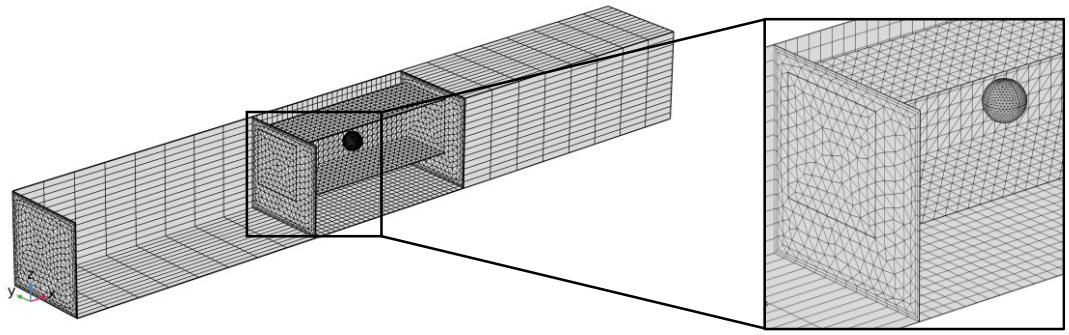

Figure 4.13. Mesh details of model geometry.

Furthermore, in order to sample the spatial lift force distribution in channel cross-section, while the spherical particle accepts as a frame of reference, the channel is slipped around the particle. Due to symmetry property, both square and rectangle can be folded in half horizontally or vertically and square can be further folded in half over either diagonal. As a result, the rectangle has two lines of symmetry while the square has four. For a circular geometry, there is an infinite number of symmetry lines all passing through the origin. Thus, while generating position-dependent data samples, the symmetric properties of channel cross-sections are benefitted. DNS is performed to calculate the force at any position in the symmetric region in the channel cross-section; then, force samples can be expanded to entire cross-section by mirroring around symmetry planes as illustrated in Figure 4.14.

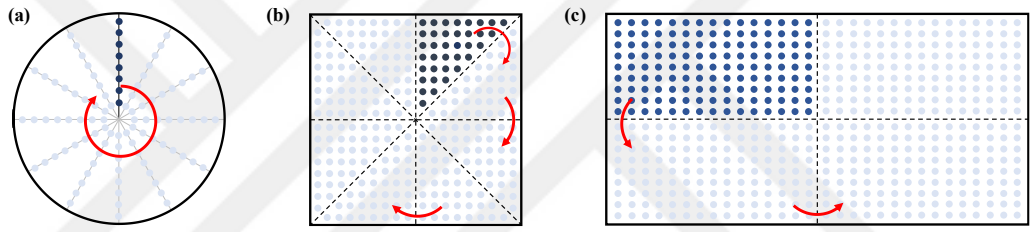

Figure 4.14. The sampling of spatial lift force data and symmetry properties of different channel cross-sections. (a) Circular. (b) Square. (c) Rectangular (AR=2).

4.7. DNS Results and Discussions

DNS simulations are completed for straight microchannels of different cross-sections, including circular, square (AR=1) and rectangular (AR=2 and AR=4) to obtain spatial lift force fields which arises in the direction perpendicular to the main flow due to combined effects of pressure and viscous forces. In Figure 4.15, distribution of total stress comprising pressure and viscous components on the particle surface is depicted in the z-direction for a channel with square cross-section under a water flow of 75 µl/min. It is observed that the pressure component is dominant to the viscous component of the stress on the particle induced by the flow. Moreover, the effect of shear increases if the particle is close to wall region as can be observed from the normalized arrow fields which represent the rotation of particles.

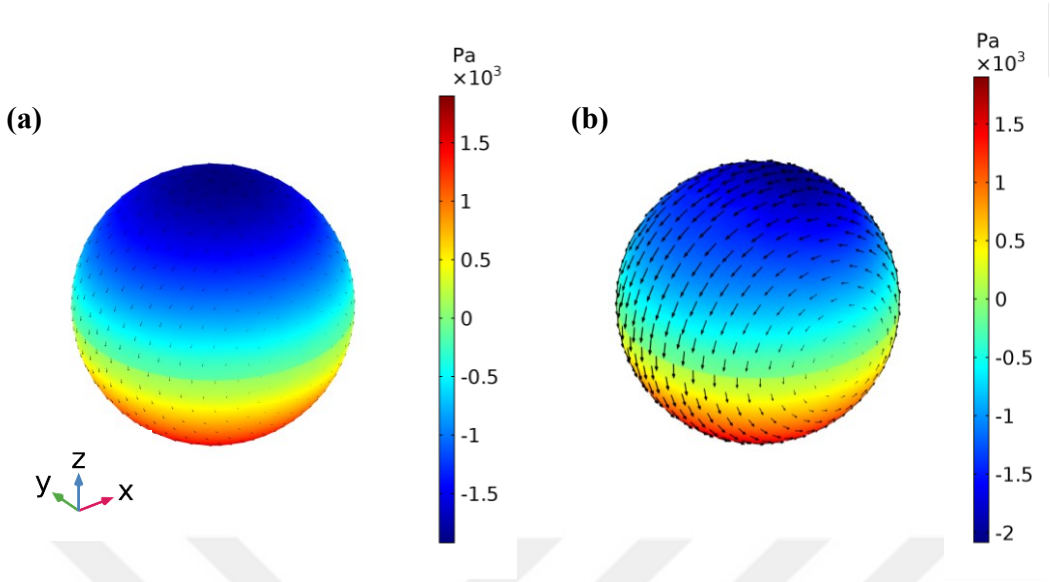

Figure 4.15. z-components of stress distribution on the spherical particle travelling at different lateral positions in a circular channel. (a) The stress distribution at a position (0,0.1h). (b) The stress distribution at (0,0.7h).

The forces can be calculated by integrating the stresses over the particle surface. In order to sample the spatial lift force distribution in channel cross-section, during the simulations, the particle is located at several positions visually illustrated in Figure 4.14 and the lift force is calculated at a specific location by integrating the total stress on the particle through y- and z-directions where x-axis is the direction of the main flow. Then, location-dependent force values obtained by the simulations are extracted into an excel datasheet and the force field is arranged in MATLAB by benefitting the symmetry properties of channel cross-sections.

The obtained spatial lift force maps at a water flow of 75 µl/min are given for different channel cross-section in Figure 4.16. These force fields are obtained for a wide range of flows between 7.5 µl/min to 300 µl/min. The magnitude of the inertial forces is directly proportional to the magnitude of the flow field. Thus, at low fields, meaningful particle equilibrium locations might not be achieved, or it necessitates excessively long channels for particles to reach these locations.

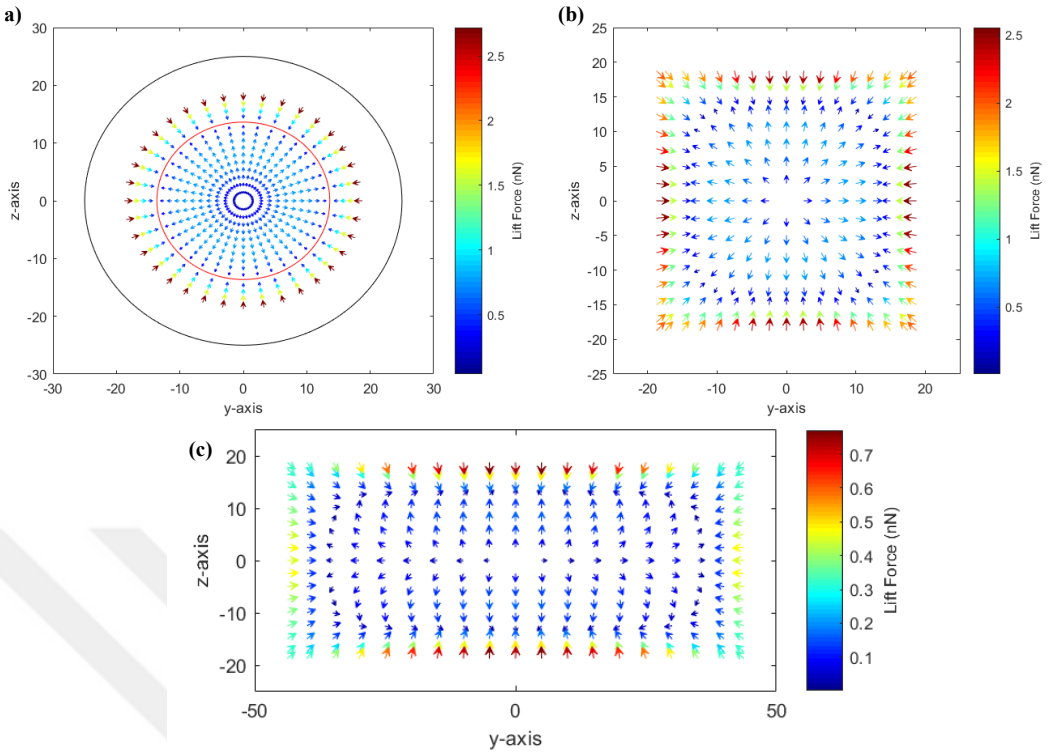

Figure 4.16. Obtained spatial lift force fields in MATLAB for different channel cross-sections at Q=75 µl/min. (a) circular (Re=25). (b) Square (Re=25). (c) Rectangular (AR=2, Re=16.67). The arrows represent the direction and magnetite of the force (in log-scale).

4.8. Particle Tracing Simulations

In order to visualize hydrodynamic focusing at straight channels and curved channels, these calculated force fields will be substituted into COMSOL as an interpolation function. These external force field will be included in Particle Tracing Interface together with built-in drag force formulation.

Figure 4.17 indicates that the formation of the ring in a circular channel around r/R=0.6 where r is the axial location of the particle can be observed even for the low flow values (with a condition of Re>1), since the magnitudes of shear-gradient and wall-induced lift force are appropriate. However, due to axial symmetry, even if the flow rate increases, the particles will continue to form a ring, but arrive the equilibrium locations faster and become closer to the wall regions.

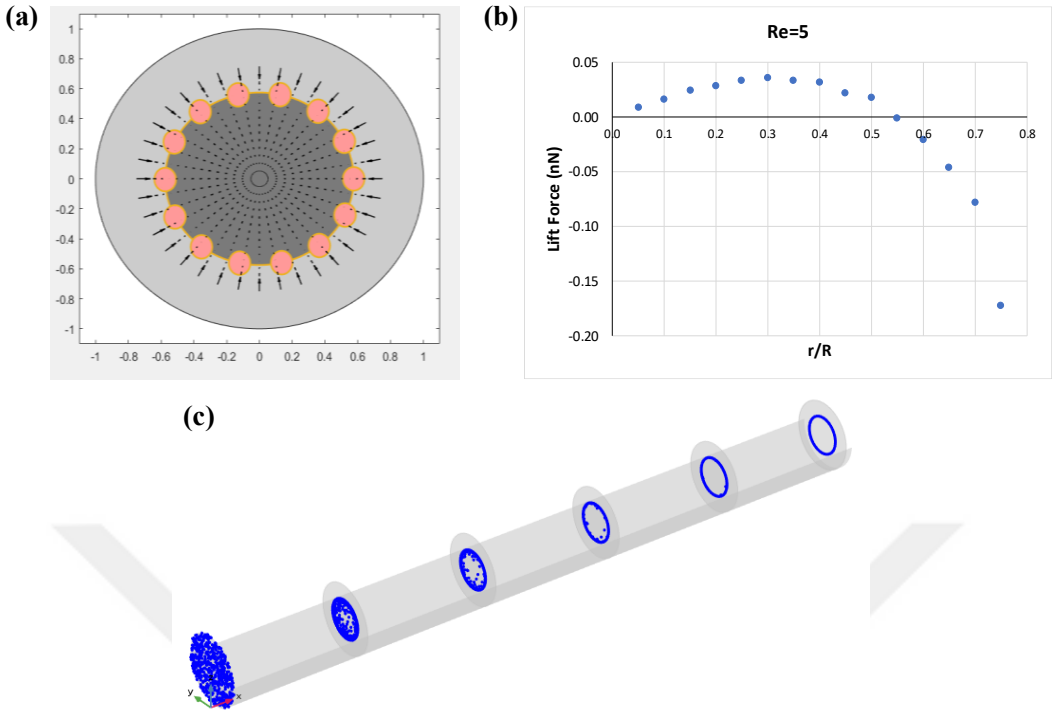

Figure 4.17. Hydrodynamic focusing in a circular channel. (a) Equilibrium locations initially extracted in MATLAB. (b) Lift force with respect to the axial position. (c) Particle focusing result obtained in COMSOL. The flow rate is Q=0.033 µl/min. The length of the channel is 10 cm.

Similar behavior is observed for the rectangular channels of different aspect ratios. The particles initially form a ring parallel to iso-contours of velocity profile similar to circular channels thanks to the balance between wall-induced force and shear-gradient force. However, after these forces cancel each other, the shear forces become dominant since the particles are close to the wall and particle migrates toward a stable equilibrium location. The active force components during the second stage of migration are at least one order of magnitude smaller, so it takes more time to particles to reach these stable equilibrium locations, thus very long channels might be necessary in accordance with the magnitude of the flow field. For instance, at a square channel with edges of 50 µm, the particles could reach to the stable equilibrium location by travelling through a channel length of 10 cm if the flow rate is smaller than 75 µl/min (Re=25). The obtained equilibrium position for square and rectangular straight channels is shown in Figure 4.18 where the flow rate is 300 µl/min.

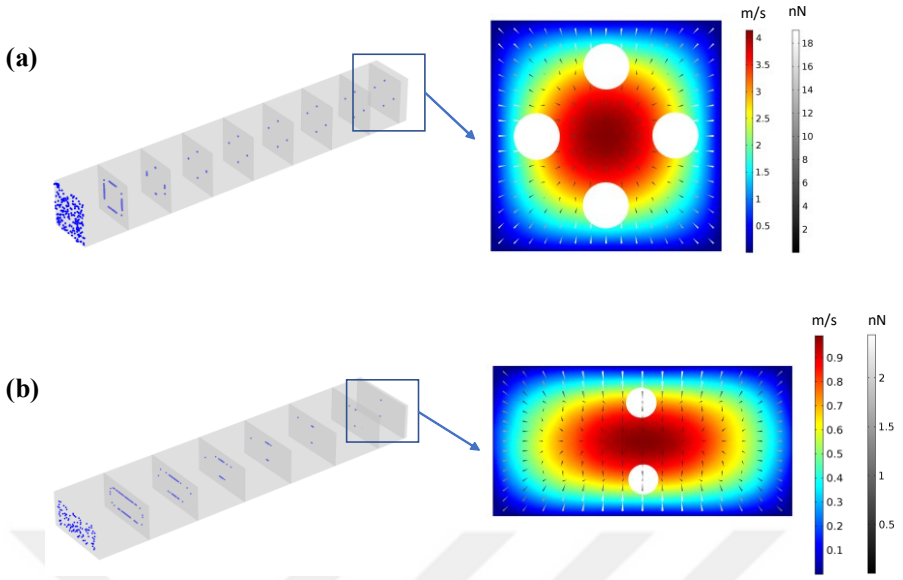

Figure 4.18. Particle equilibrium positions at the straight square and rectangular channels observed in COMSOL particle tracing simulations. The arrow field represents the magnitude and direction of the lift force. The flow rate is 300 µl/min. The length of the channel is 10 cm.

After evaluating the particle focusing at straight channels, the particle focusing at curved channels which give rise to the formation of secondary drag flows was also observed by particle tracing simulations for a spiral channel used widely in the literature. It was observed that apart from forming a ring around walls, the particles eventually focus on two stable equilibrium positions while travelling through the curved channel (Figure 4.19). By adjusting the dean number by modifying the flow rate or curvature of the channel, even a single equilibrium position might be achieved.

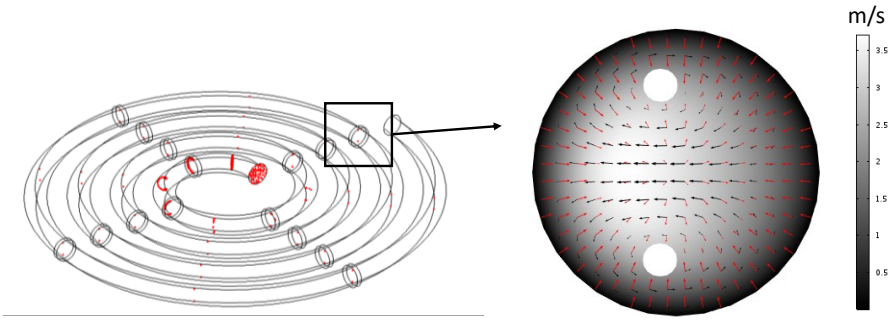

Figure 4.19. Particle focusing obtained in a spiral channel with circular cross-section. The flow rate is 300 µl/min. The black arrows indicate the secondary flow while the red arrows indicate lift force.

Finally, the hydrodynamic focusing on the passive CEA micromixer is also evaluated by the particle tracing simulations. For this purpose, to be able to define lift force in the channel cross-sections, the circular wells are sampled by rectangular channels of different aspect ratios which the lift force distribution is obtained beforehand by DNS study. As it can be observed clearly from Figure 4.20, although the initial distribution of the particles at the channel inlet is random, at the outlet, they tend to focus on a single streamline. Thus, any additional sub-unit will not be added to the microchannel network for enhancing the single-cell encapsulation ratio. The effect of micromixer structure on the single-cell encapsulation rate will be investigated experimentally.

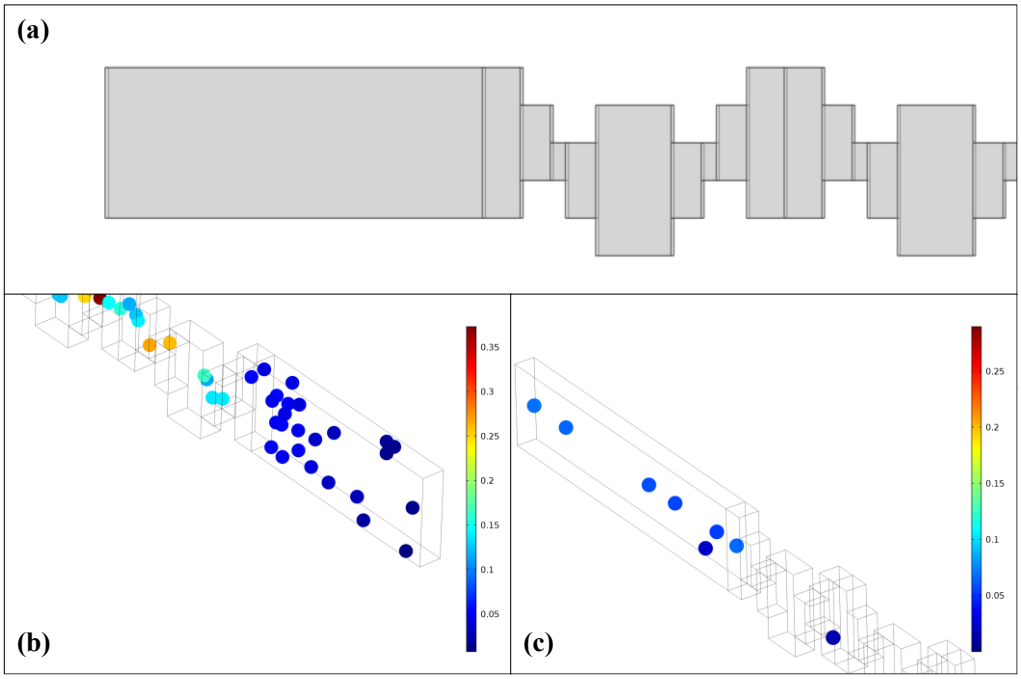

Figure 4.20. Hydrodynamic focusing in passive CEA micromixer. (a) Sampling of circular wells by rectangular microchannels. (b) Particle distribution at the inlet. (c) Particle distribution at the outlet. The flow rate is 30 µl/min.

CHAPTER 5

FABRICATION AND EXPERIMENTAL VALIDATION OF DROPLET SCREENING WORKFLOW

In this chapter, the fabrication and the experimental characterization of microfluidic sub-units, including micromixer, droplet formation, and hydrodynamic cell ordering are presented. Then, the experimental results regarding each phenomenon will be compared with the results of numerical analysis given in preceding sections. Eventually, the microfluidic sub-units are combined to compose a full droplet screening workflow, after deciding the joint operation range. As a proof of concept, the complete microfluidic device is tested to quantitively score cell viability within intact droplets and assess the response of K562 cells to the chemotherapy drug doxorubicin.

5.1. Microfluidic Device Fabrication

For the fabrication of the microfluidic devices, soft-lithography is applied which is a technique for replicating structures embedded into molds using elastomeric materials, most notably PDMS. Polydimethylsiloxane (PDMS) is the most widespread material used in microfluidic device fabrication thanks to its considerable advantages. Apart from the fabrication ease and being comparatively inexpensive, it is optically transparent, biocompatible, chemically inert, gas permeable, allows molding of structures at high-resolutions down to the nanoscale, has a low autofluorescence, and tightly bonds to glass surfaces through simple plasma treatment.

The mold for casting PDMS is prepared by photolithography on a silicon wafer. On the same wafer, multiple designs and their duplications can be included to maximize the occupancy of the available area. Thus, several prototypes of microfluidic sub-units and a combined PDMS device are fabricated by using a single wafer as a master for

PDMS molding. The layout of these structures is drawn using Tanner L-Edit software, and a chrome mask is printed to be used in patterning photoresist during photolithography. It should be noted that after completing the drawing of the mask, the final layout was enlarged with respect to the center of the mask by 1.9% to account for shrinkage during temperature assisted curing [132]. The corresponding layout of the mold is illustrated in Figure 5.1.

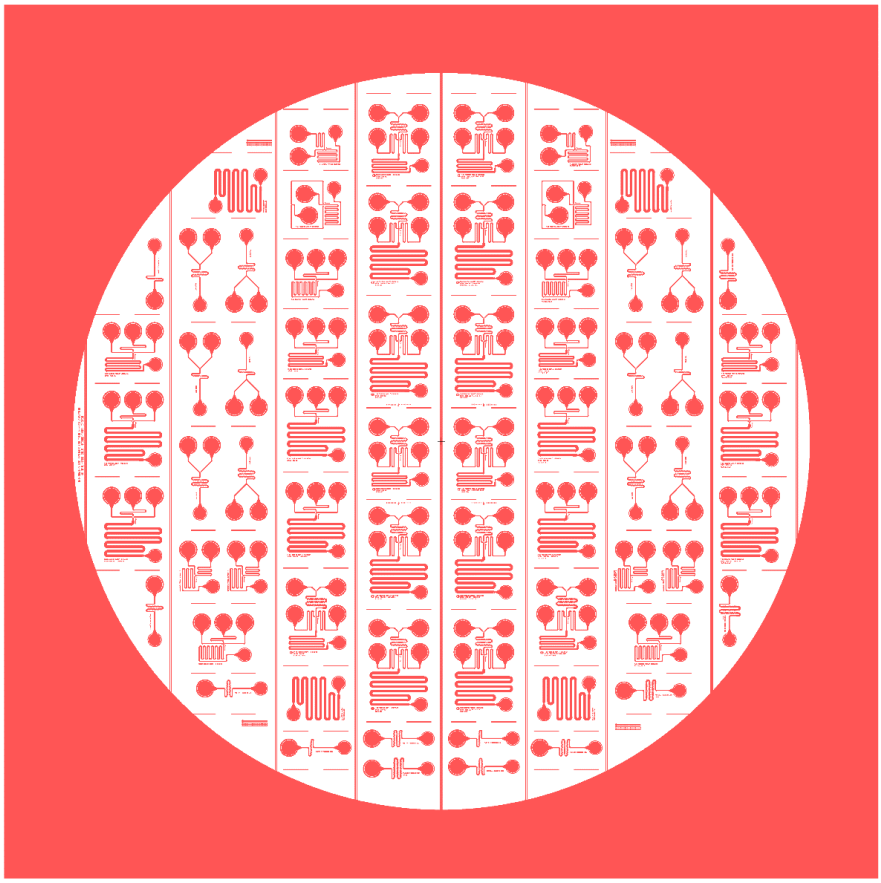

Figure 5.1. The mask layout of the mold which is used for PDMS device fabrication for experimental characterization of microfluidic sub-units.

The silicon master is made by AZ® 40 XT photoresist by using the recipe that results in 50 µm thickness. In order to achieve easy peeling of PDMS from silicon mold by lowering the surface energy, silanization of the mold is completed by keeping the wafer in a vacuum desiccator together with a few drops of Trichloro(1H,1H,2H,2H-perfluorooctyl)silane, 97% (PFOTS, Sigma Aldrich) for a couple of hours. Thus, a

hydrophobic anti-adhesive self-assembled silane monolayer is formed on the surface of the master mold thanks to functional groups of PFOTS. Then, PDMS prepolymer is mixed with the curing agent in a ratio of 10:1. The mixture is degassed in a desiccator, poured on the mold, and cured at 80 ºC for 90 minutes. After peeling of PDMS, the individual devices are cut by a razor blade, and inlet/outlet ports are opened using a biopsy punch. Finally, devices are irreversibly sealed with glass slides by using oxygen plasma-assisted bonding at 100 W for 90 sec. The whole procedure is illustrated in Figure 5.2.

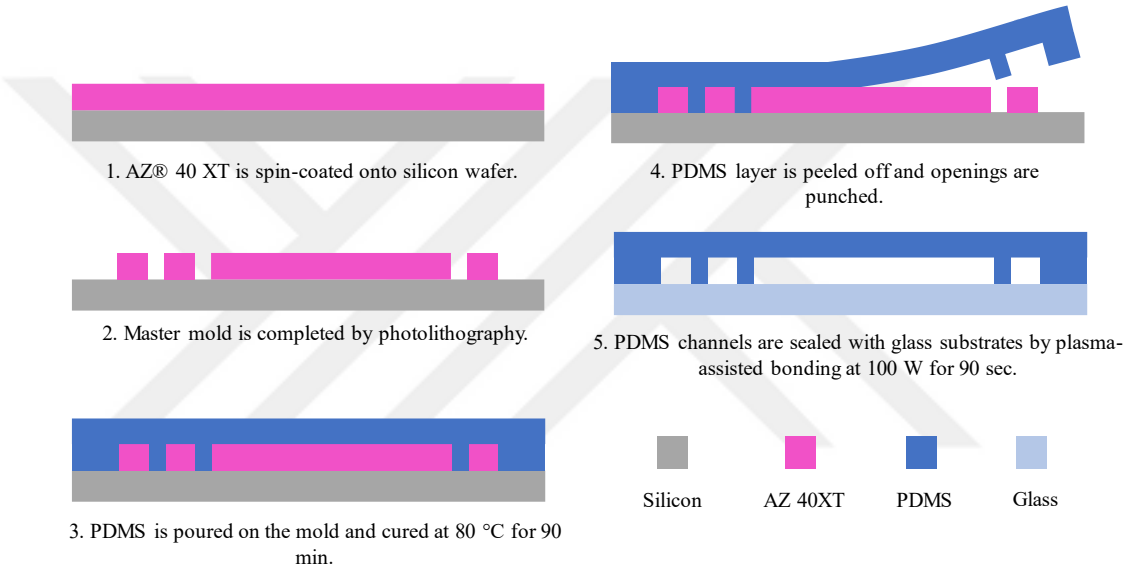

Figure 5.2. Schematic showing fabrication steps of PDMS devices actualized by soft lithography.

5.2. Experimental Characterization of Proposed CEA Passive Micromixer

The experiments which investigate the mixing performance of passive micromixer proposed in Chapter 2 was completed with PDMS devices fabricated by soft-lithography. The schematic of the passive micromixer used in performance tests is illustrated in Figure 5.3. The fabricated micromixer has 63 sequential throttles whose width is 50 μm because it is expected to achieve higher mixing performance in comparison with a lower number of throttles according to numerical results.

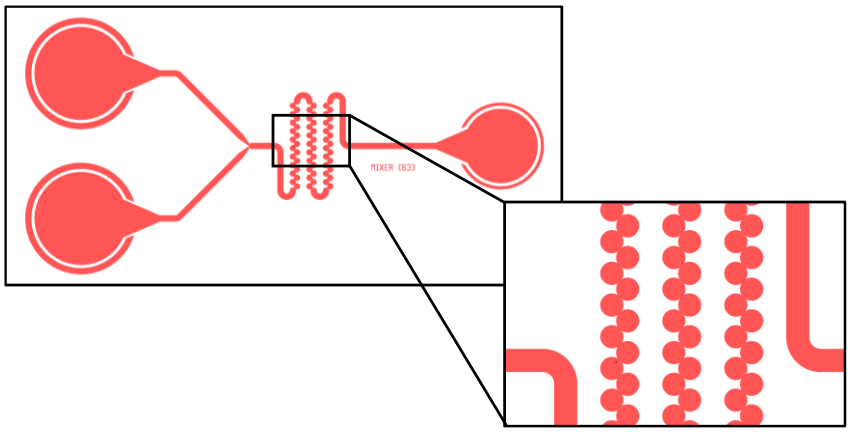

Figure 5.3. Layout drawing of contraction-expansion type passive micromixer which is fabricated by PDMS soft-lithography.

During the tests, the flow was fed by utilizing a double pressure pump. Thus, the inlet pressure values corresponding to the flow rates used in the simulations is determined in MATLAB by using the analogy between electric and fluid circuits where the pressure is analogous to the potential difference and the flow rate is analogous to the electrical current. The hydraulic resistance is calculated by the equation 3.21. One inlet was filled with DI water colored by adding Ponceau 4R red food dye while the other is dispensed through DI water only. Throughout the tests, the exit of the micromixer structure is observed under a microscope and given in Figure 5.4 for different flow rates.

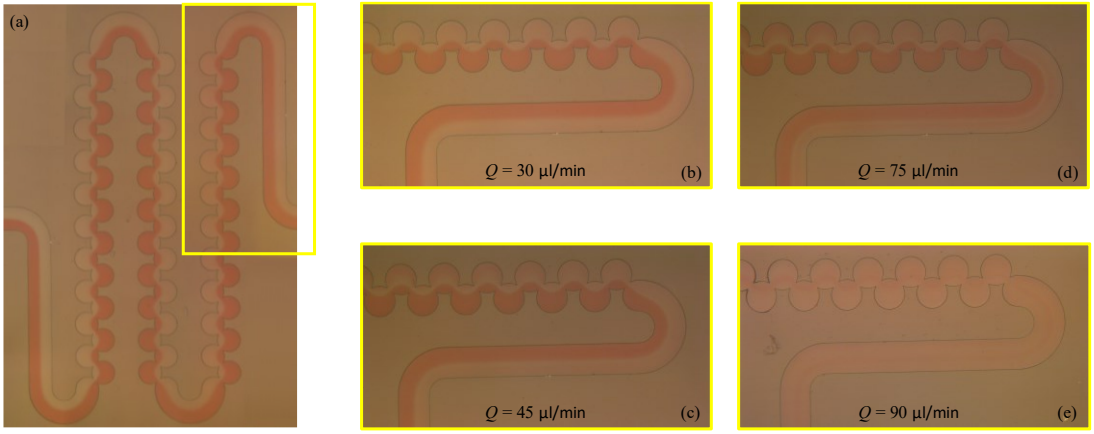

Figure 5.4. Microscopic images which are taken during micromixer characterization experiments. (a) Composite microscope image exhibiting the whole micromixer operating at Q=7.5 µl/min. (b-e) Outlet profiles indicating mixing of two species for different flow rates.

To measure the mixing efficiency, the same figure of merit for an area of interest which is used in the simulations is calculated by assuming the grayscale intensities as a direct indicator of species concentration (Equation 2.9). Grayscale intensity profiles across the width of the microchannel for captured RGB images were analyzed by using MATLAB to obtain measured mixing efficiency. First, the images obtained by digital microscopy generally suffers from uneven illumination and shading. Moreover, due to dimensions of the device, the outlet and inlet profiles could not be obtained in the same image which further worsens the problem. Thus, to correct the intensity values of the images, the histogram of the image representing the outlet is adjusted to match the histogram of the image indicating micromixer entrance at the inlet side. This method matches the intensities of the images, also corrects the backgrounds to a certain extent. Then, the electronic noise arising from random variation of brightness or color information is reduced by applying a Gaussian smoothing filter with a low standard deviation to prevent excessive blurring. Apart from the uneven illumination and noise problem, the measured intensity values of the food dye do not linearly change with its concentration. For instance, even for complete mixing at the outlet side, the resulting average intensity value is so close to the average intensity of food dye solution at the inlet before mixing. Hence, to take the minimum and maximum intensities corresponding to unmixed liquids at the inlet side directly as a reference for the limits of species concentration might precipitate misleading results for mixing efficiency.

Here, to be able to extract meaningful information from the experiments, first intensity distribution matrices at the inlet and the outlet are obtained for a rectangular region of interest. These matrices are column averaged to achieve the longitudinal intensity distribution along the width of the channel. Before matching two intensity peaks measured at the inlet to reference concentration limits (c_{min}=0 mol/m^3 and c_{max}=1 mol/m^3), the mean value of the intensity distribution along the channel width is matched independently with the desired average concentration at both the inlet and the outlet; then, matched with the peaks to achieve normalized intensity values

between 0 and 1. Finally, obtained normalized intensity profiles for inlet and channel exit are illustrated in Figure 5.5.

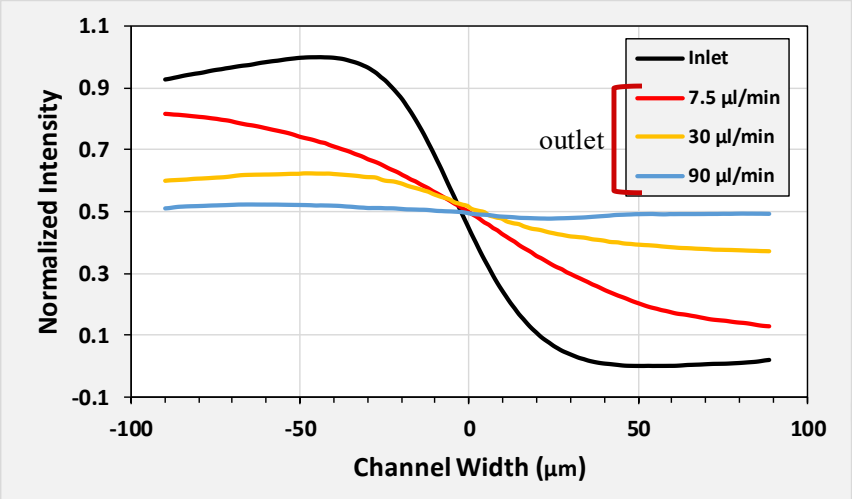

Figure 5.5. Normalized intensity values indicating species concentration at the entrance and the exit of the micromixer based on the fluidic experiments.

Moreover, for each of the experimental results given in Figure 5.4, mixing indexes corresponding to the flow rates of the samples is computed. The experimental results obtained by the above methodology shows good consistency with numerical results obtained in COMSOL (Figure 5.6).

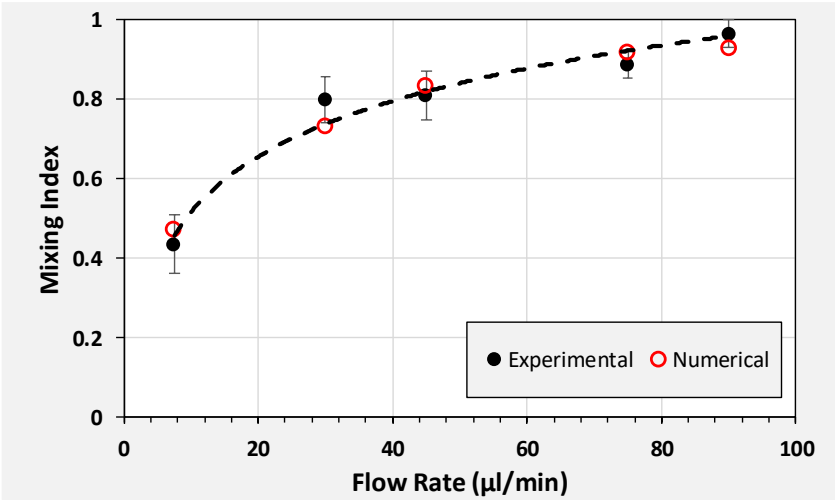

Figure 5.6. Experimentally measured mixing index in comparison with the numerical results for the passive CEA micromixer with 63 throttles with regard to sample flow rate.

5.3. Experimental Characterization of Droplet Formation

For the experimental characterization of the flow focuser, at the beginning of the study before being able to use microfabrication techniques, initial tests regarding droplet formation in a flow-focusing junction was commenced by manufacturing microchannel networks on Poly(methyl methacrylate) (PMMA) substrates using CNC micromilling because the droplet formation process employs complex dynamics due to involvement of several parameters such channel dimensions, flow rates, densities and viscosities of both phases, and unpredictive behaviors of the surfactants. More importantly, it was significant to initiate microfluidic tests to become familiar with the usage of the flow generators such as syringe pumps, pressure or vacuum pumps, fluidic connectors, sealing and plugging of devices and priming methods to prevent blockage of channels due to air bubbles.

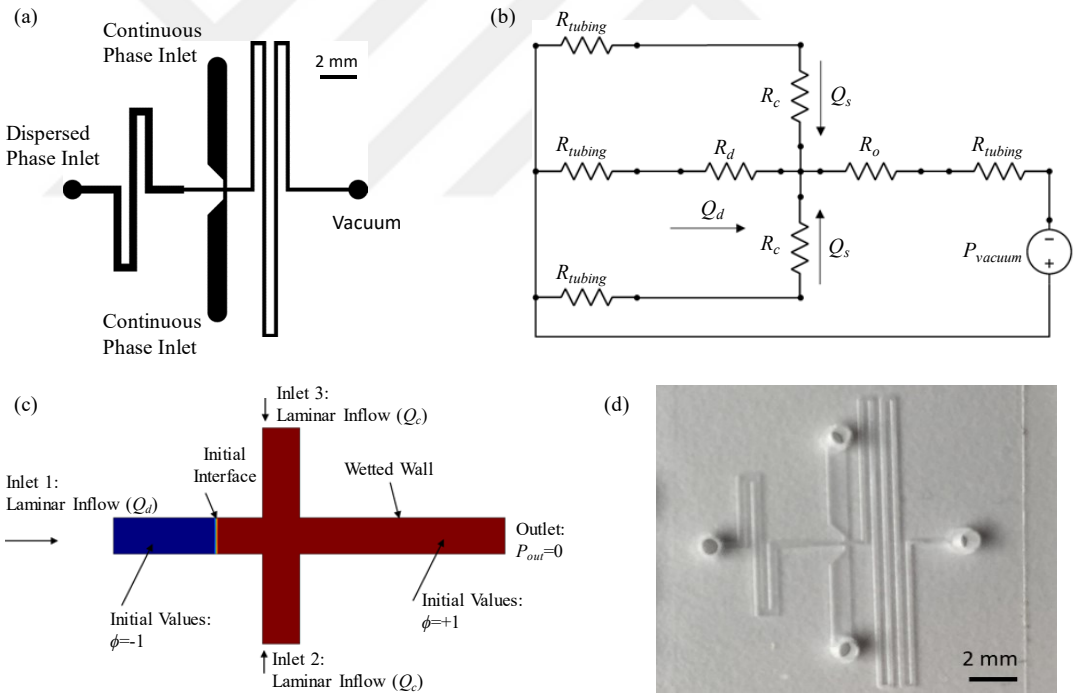

Figure 5.7. (a) Schematic of the flow-focusing junction used in initial droplet formation experiments. (b) Hydraulic circuit model to find out vacuum pressure at the outlet with respect to desired flow rates. (c) Simulation geometry and regarding boundary conditions of the junction. (d) Final PMMA test device manufactured by CNC micromilling.

Due to manufacturing limits of micromilling, the minimum achievable channel width and depth are 200 μm and 100 μm, respectively; thus, the proposed microchannel for droplet formation illustrated in Figure 3.3 could not be achieved due to capabilities of CNC machining. As expected, this expansion in the channel width causes an increase in achievable droplet diameter for similar flow parameters. Thus, the results of this study are correlated with simulations by repeating them for the geometric parameters presented in Figure 5.7 (a) is manufactured by micromilling method. The channels are sealed with using a tape (3M Scotch transparent tape 600). Figure 5.7 (d) shows the final prototype microfluidic chip. The microfluidic device is tested by applying different vacuum pressures from the outlet port using silicone oil (10 cSt) and water as continuous and dispersed phases, respectively, without the addition of the surfactants.

Droplets formation during the experiments is recorded using a high-speed camera. Figure 5.8 illustrates the droplets formed under different vacuum pressures. The images were analyzed using an image processing code prepared using MATLAB. For this purpose, first, a single frame is extracted from the recorded high-speed video. During calibration, the length of a known channel dimension in pixels is measured, and this known dimension is divided by the measured length in pixels, so the length of each pixel is determined in micrometers. Then, on the same frame, the position of the droplets was obtained using the circle search command (imfindcircles) which is a built-in function of MATLAB. This function gives the position of the droplets as well as their diameter in pixels accurately. Droplet diameters in pixels were converted to μm using the calibration ratio. In order to determine the droplet formation frequency, the next frame in the sequence is also extracted. The amount of displacement of the droplets between these two frames was measured in micrometers. The value of droplet velocity is calculated by dividing this measured distance by the time interval between consecutive frames. Additionally, this velocity was divided by the distance between two consecutive droplets in the first frame to eventually acquire the droplet formation

frequency in Hz. Hence, the droplet diameter and droplet formation frequency are obtained for each pressure value.

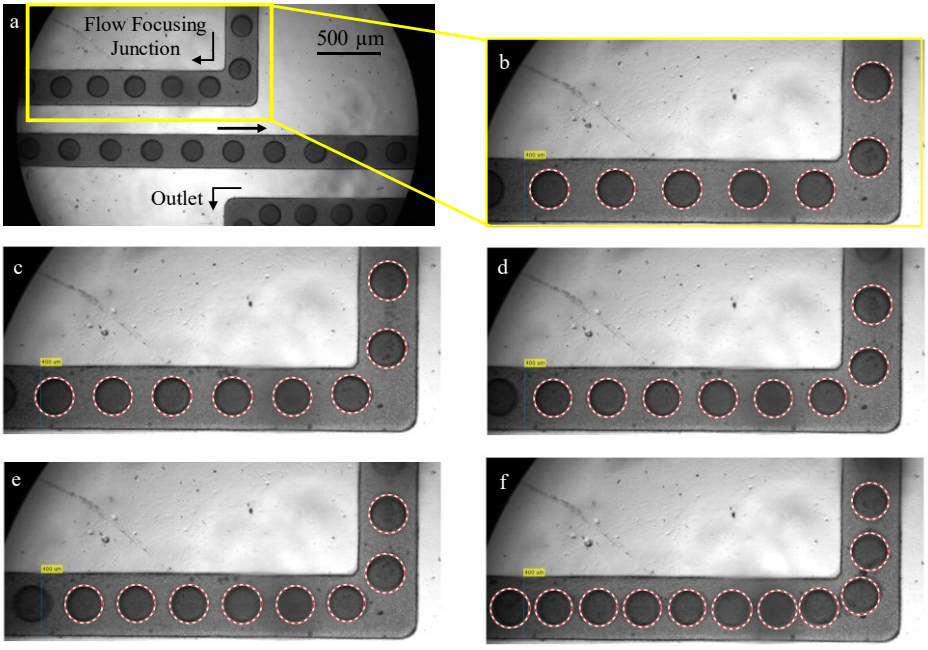

Figure 5.8. The views of droplets within the channel obtained for different values of applied vacuum pressure. (b) -100 mbar, (c) -150 mbar, (d) -200 mbar, (e) -250 mbar and (f) -300 mbar. Dispersed and continuous phases are DI water and silicon oil (10 cSt), respectively.

Figure 5.9 compares the droplet diameter and droplet formation frequency obtained as a result of the experiments with the numerical results obtained by COMSOL simulations. The smallest droplet diameter is measured as 240 µm. On the other hand, it is seen that the experimental results show a correlation with the numerical results obtained by 2D analysis using shallow channel approximation presented in Section 3.4. In these experiments, and the camera is used at its highest resolution (2048x1088 px) to be able accurately to measure the droplet size, so a maximum recording speed of 170 fps is achieved. Therefore, the measured droplet formation frequencies remain at a maximum of approximately 130 Hz. When the vacuum pressure was lowered below -30 kPa, it is observed that the droplet formation frequency increased, but it is not possible to obtain a processible image to measure the exact value of formation frequency. Another parameter that defines the performance of droplet formation is the

droplet size distribution. For evaluating this, the standard deviation and the mean droplet diameter is calculated. The value of the standard deviation is less than 3% for all pressure values. Accordingly, it is observed that the droplets formed using the flow-focusing junction have a high monodisperse distribution characteristic.

In the proposed integrated multi-drug analysis device, the viability of the cells trapped within the drug droplets over time must be monitored on-chip. This requires the droplets to remain stable during the test period which is the minimal requirement for the use of droplets as microreactors. Considering the operation of the integrated chip, it appears that the cells need to be transmitted to the chip as a suspension in a cell culture medium to provide necessary ingredients for cell viability. In this case, the droplet content will be a mixture of the medium and the drug. Accordingly, in order to experiment the stability of the droplets over time, silicone oil was used as the continuous phase, and RPMI-1640 media which has been specifically developed for the culture of human leukemia cells are used as the dispersed phase. In the trials, the vacuum pump is closed suddenly during operation. Since the pressure-driven flow control ensures high responsiveness, after stopping the vacuum generator, the droplets remain almost stationary in channels, and they can be observed for stability over time. As a result, it is seen that the droplets merged immediately after the closure of the vacuum pump (Figure 5.10 (a)). It suggests that some measures should be taken to increase droplet stability for viability observation. There are different solutions to droplet coalescence in the literature which employ the addition of surfactants into either phase. Here, surfactants are vital components of the droplet-based microfluidics to achieve the stabilization of droplet interfaces. Naturally, dispersion of immiscible fluids is a system out of thermodynamic equilibrium due to excess energy requirement for the creation of the interfacial area between them, so the system evolves into a configuration where the two liquids are homogenized into two separate phases due to minimum energy principle. This driving force can be counter-balanced by the addition of surfactants which induces steric repulsion due to the arrangement of surfactant

molecules at the interface and the drainage of the continuous film between droplets due to changes in the surface tension gradient, namely Marangoni effect [133].

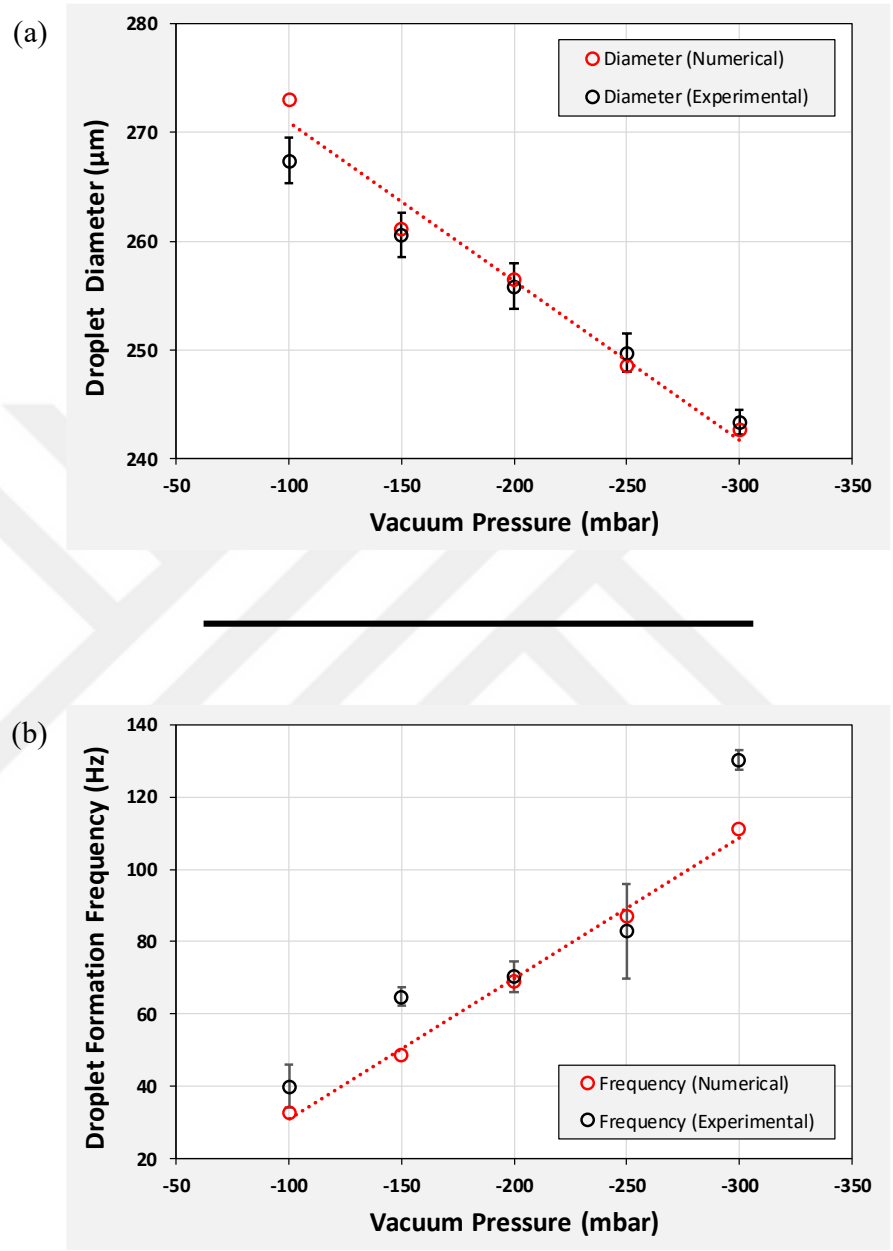

Figure 5.9. A comparison of experimental values of (a) droplet diameter and (b) formation frequency with numerical results.

In one of these solutions in literature, it is recommended to use hexadecane as 3% Span-80 surfactant mixture instead of silicone oil [134]. However, when this solution

proposal is tried, a result similar to the previous which involves no surfactants is obtained (Figure 5.10 (b)). In the next attempt, it is tried to change the dispersed phase instead of the continuous phase. Instead of RPMI-1640, a buffer solution of 8.5% sucrose and 0.3% dextrose is used as a different cell medium while the continuous phase is hexadecane (3% Span-80). It is observed that the droplets obtained using this solution did not merge immediately after the flow stopped (Figure 5.10 (c)). However, over time (about 30 minutes), the interface between the droplets is observed to begin thinning. This means that droplets can be tended to coalesce in long-term use.

As an alternative to these solutions, perfluoropolyethers (PFPEs), which are soluble in fluorocarbon oils provides good stabilization due to steric repulsion by forming a dense PFPE layer on the outer droplet surface [135]. Hence, it has been tried to use a mixture of a fluorinated oil (HFE-7500, 3M) and an unmodified fluorosurfactant (Krytox 157FSH) as the continuous phase while the dispersed phase is RPMI medium. In the experiments using the fluorosurfactant, it is observed that droplets retain their shapes for up to 12 hours (Figure 5.10 (d)) in PDMS channels. However, due to its charged carboxylate group, it is expected that Krytox interacts with the biomolecules of the opposite charge confined in the droplets, so interferes in their biological activity and causes them to absorb at the interface [135]. Thus, this limits its appeal for an application involving biological activity.

Consequently, the carboxylic head group has to be substituted with different nonionic hydrophilic head groups. Among fluorosurfactants, the polyethylene glycol (PEG) based triblock copolymer surfactant (PFPE-PEG-PFPE) has presented the most encouraging outcomes in restraining nonspecific agglomeration of biomolecules and permitting successful encapsulation of mammalian cells [136], [137]. Despite its performance, since the modification chemistry is relatively complicated, a commercially available biocompatible fluorosurfactant (PicoSurf ®, Dolomite) is obtained and similar results for droplet stability is achieved for HFE 7500 with 2% PicoSurf in comparison with Krytox.

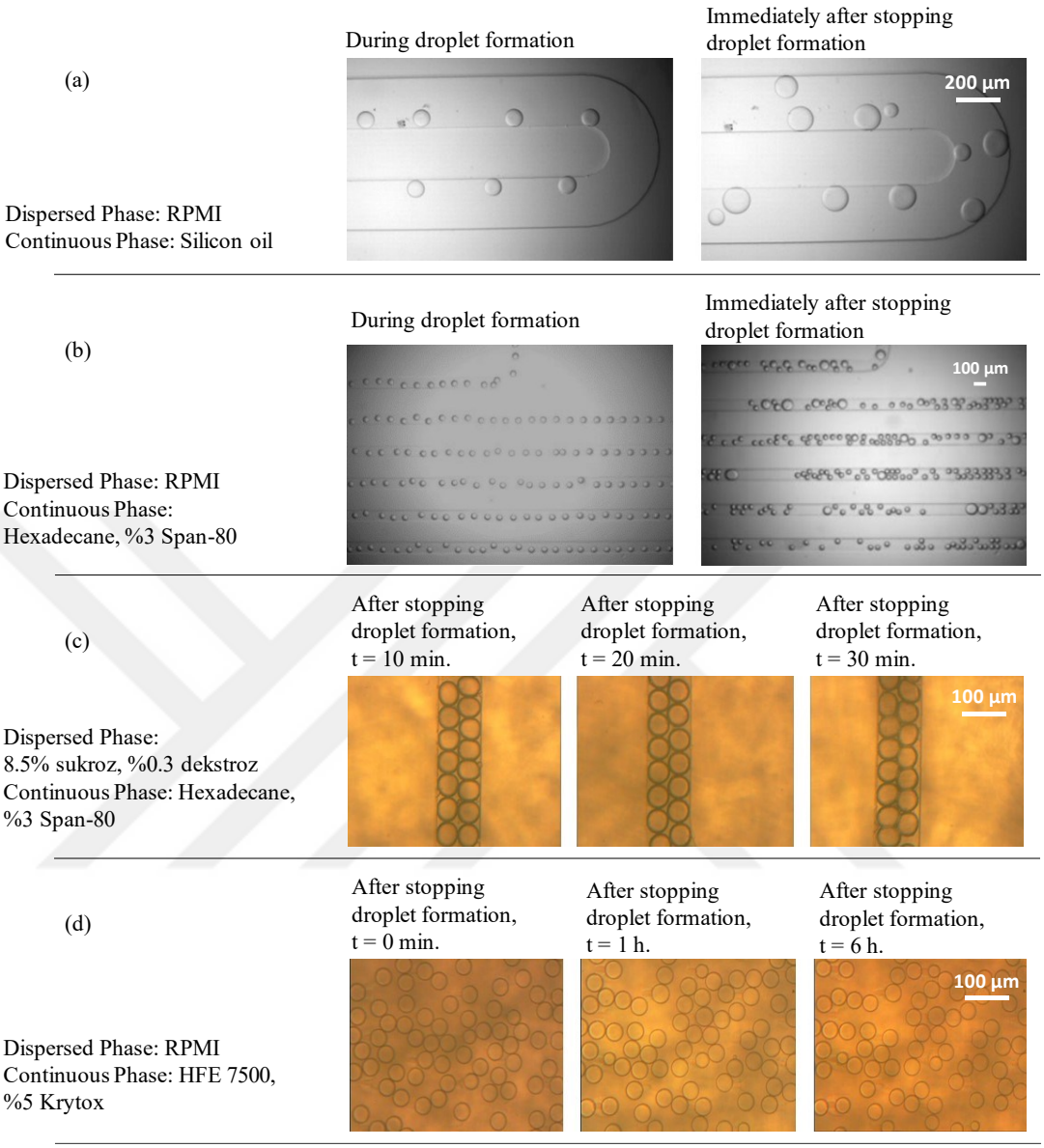

Figure 5.10. (a) RPMI and silicon oil. (b) RPMI and hexadecane (3% Span-80). (c) 8.5% sucrose, 0.3% dextrose mixture and hexadecane (3% Span-80), (d) RPMI and HFE7500 (5% Krytox).

Moreover, after being able to fabricate the silicone mold for soft lithography, droplet formation experiments are repeated by using PDMS microdevices sealed with glass covers which consists of the flow-focusing junction presented in Figure 3.3 and used for numerical modelling of droplet formation. The schematic of the device is illustrated in Figure 5.11.

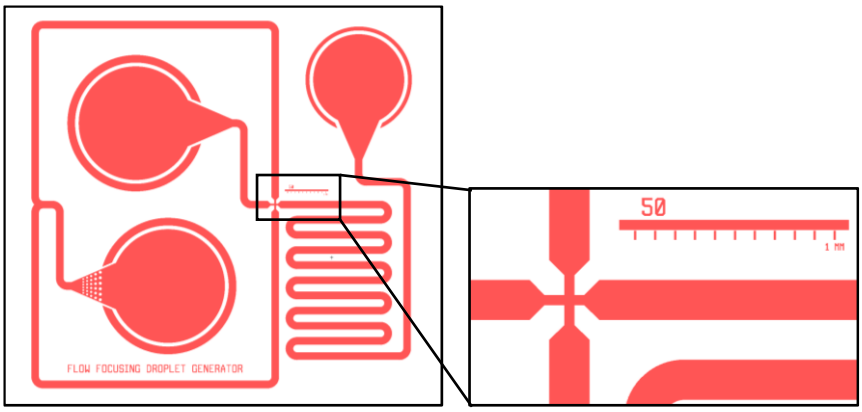

Figure 5.11. Layout drawing of droplet formation device which is fabricated by PDMS soft-lithography.

The design utilizes a common inlet for continuous phase which comprises a basic in-line filter. During before experiments regarding droplet formation, due to some undesired particles which mostly come from oil sample, a blockage of the flow focusing nozzle was experienced. Thus, in order to minimize this potential blockage of nozzles, in-line inlet filters which consist of several circular pins are included. These in-line filters block undesired particles before they are introduced to the microchannels if they are larger than a certain threshold which is smaller than the dimensions of the junction. The longest distance between the circular pins is 60 µm. This space becomes narrower towards the channels up to 35 µm. The filter threshold is not reduced further because the nozzle width in the junction is 50 µm. The examples of these filters can be seen in several studies in literature and commercial devices [138].

For the testing of the device, Novec 7500 (%2 PicoSurf) and DI water are used as continuous and dispersed phases, respectively. Then, a positive pressure is applied at both inlets by using a microfluidic pressure controller (Fluigent, MFCS-EZ). These pressure values are calculated with respect to flow rates used in the simulation study in Chapter 3 by solving a hydraulic circuit model of the microchannel network to able to compare the experimental and numerical results. Figure 5.12 indicates experimental images of droplet formation under varying inlet pressures obtained by using PDMS device which is shown in Figure 5.11.

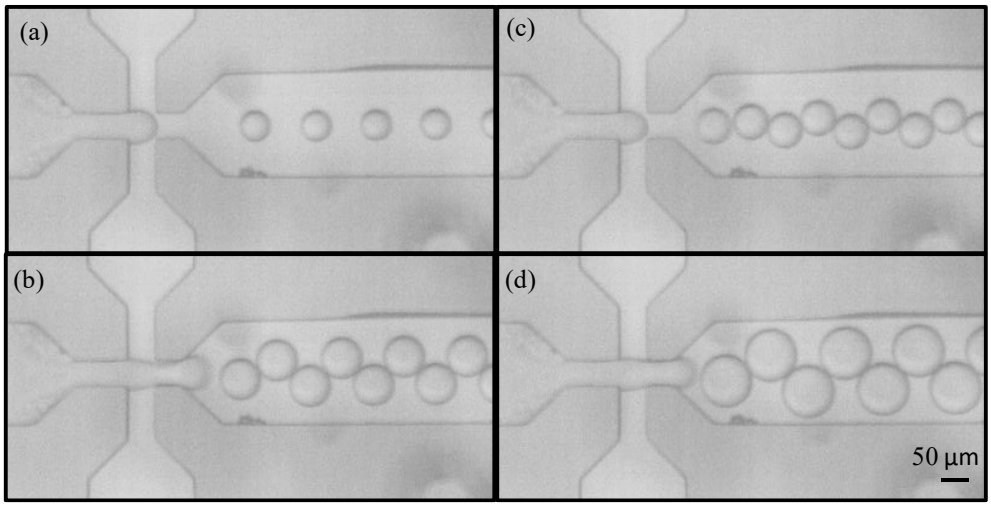

Figure 5.12. Experimental images of droplet formation under varying inlet pressures at water inlet. (a) 70 mbar. (b) 75 mbar. (c) 80 mbar. (d) 85 mbar. For all results presented, the inlet pressure at oil inlet is 80 mbar.

Figure 5.13 visually compares the droplet breaking process obtained as a result of the experiments with the numerical results obtained by COMSOL simulations for two instances of flow rates of both immiscible phases. The numerically simulated droplet formation results are well matched with the experimental data that suggests accurate modelling.

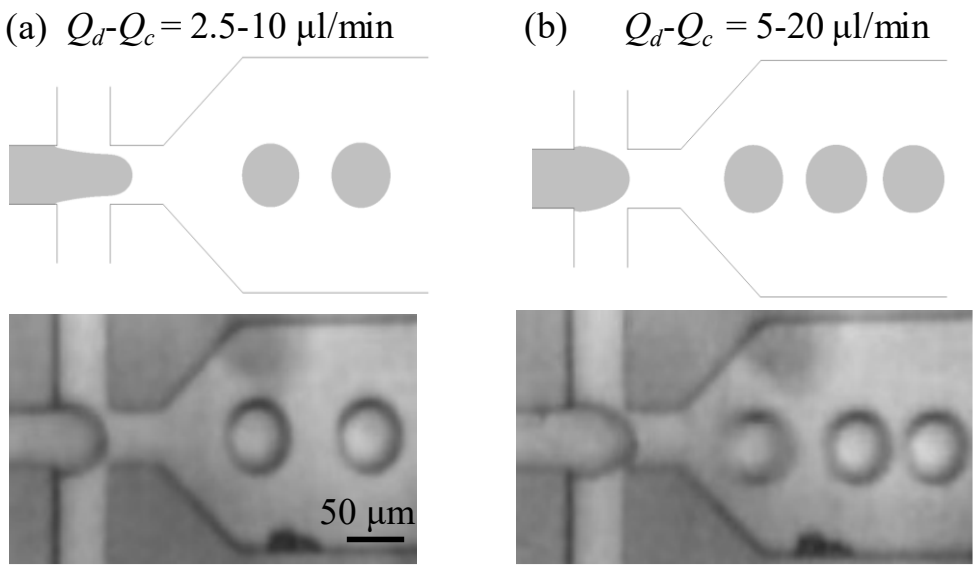

Figure 5.13. Comparison of the experimental outcomes with the numerical results of droplet formation.

Lastly, experimental droplet size distribution with respect to flow rates of both immiscible phases is given in Figure 5.14. As can be interpreted from the figure, spherical droplets with an effective size around 50 µm can be obtained by altering the flow rate values of both phases.

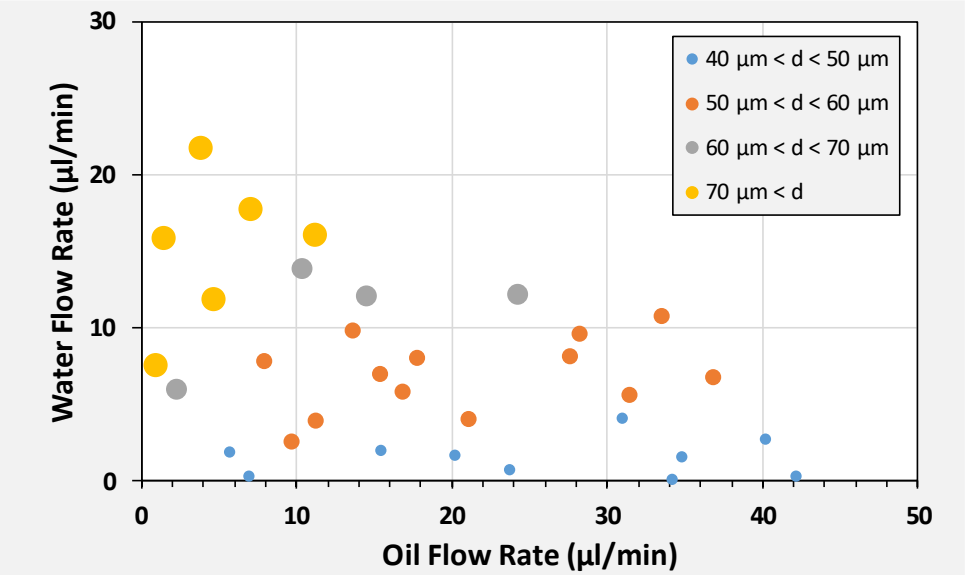

Figure 5.14. Experimental droplet size distribution with respect to the flow rates of the dispersed and continuous phases.

5.4. Experimental Characterization of Hydrodynamic Focusing for Enhancing Single-Cell Encapsulation

Considering the effect of dean flow for hydrodynamic focusing of particles and cells, the passive micromixer which is already included as a sub-unit in the microfluidic droplet workflow to achieve an efficient mixing of cell medium and drugs can lead to an improvement in single-cell encapsulation performance. Therefore, proposed contraction-expansion type passive micromixer consisting of consecutive sequential throttles that are connecting several circular wells is tested for evaluating the performance of single-cell confinement in droplets which is normally a stochastic process dictated by Poisson statistics. The droplet formation chip shown in Figure 5.15 is used in these experiments. On the design of the microfluidic device, there is a micro-mixer carrying the particle suspension, and droplets are formed in the flow

focusing junction which is located at the outlet of the micro-mixer. Test chips are manufactured with the standard PDMS molding method (Figure 5.2). During the experiments, the flow is provided by applying a vacuum through the outlet port. As a particle suspension, 1:10 buffer solution (PBS/DI water) - containing $1x10^6$ microbeads/ml concentration was used. The size of the microbeads is 10 µm. Silicon oil with a kinematic viscosity of 10 cSt was used as the carrier liquid.

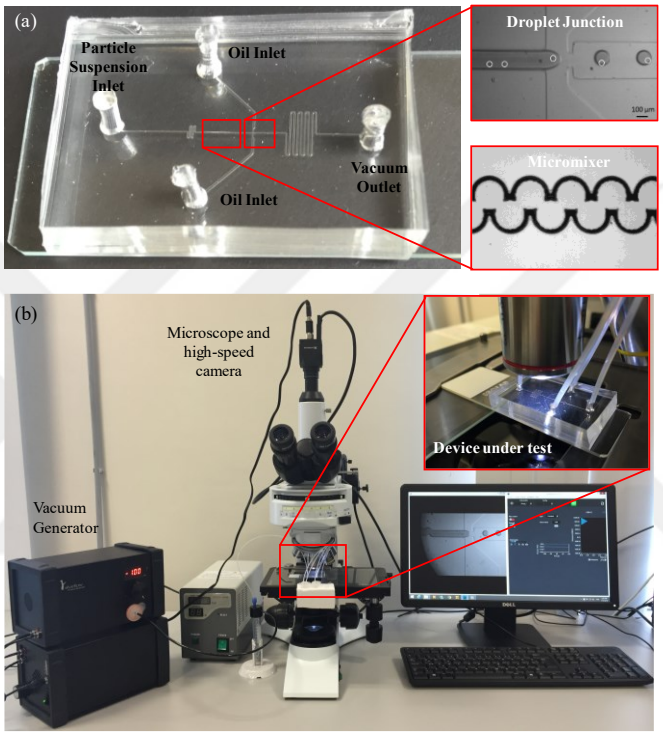

Figure 5.15. Single cell encapsulation experiments. (a) PDMS test device. (b) Experimental setup.

The droplet formation was observed under high-speed camera (169 fps) by applying a -10 kPa vacuum from the outlet port. During the test, the diameter of droplets created at 40 Hz was measured as 125 µm. According to this result, λ is calculated as 0.55. The probability of creating droplets with a single particle for the value λ = 0.55 is calculated as 32% according to the Poisson distribution. However, as a result of the experiment, it is observed that the particles are arranged near the channel walls at the exit of micromixer structure and the proportion of droplets containing single particles was measured as 42% (Figure 5.16). This result has also shown that the passive

micromixer structure can also be used to increase cell ordering in microchannels, and thus individual cell confinement performance.

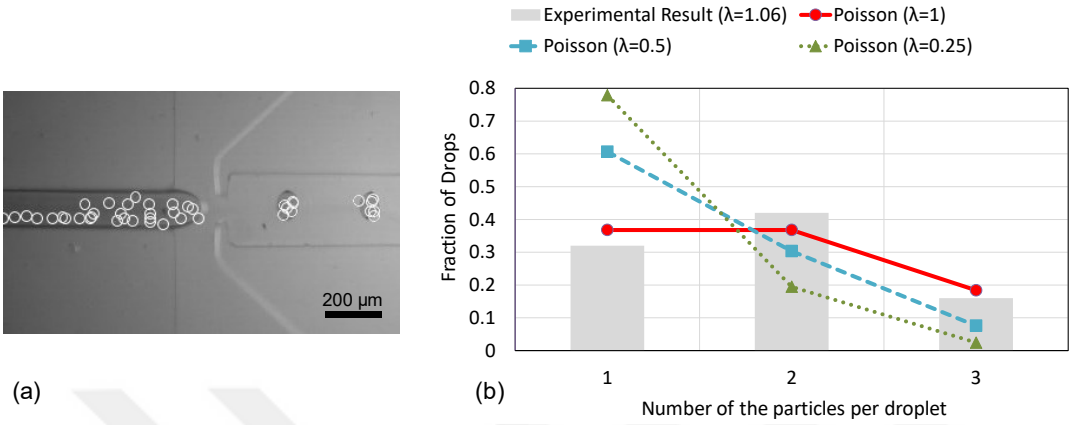

Figure 5.16. Experimental result of single-cell encapsulation. (a) The hydrodynamic ordering of particles. (b) The fraction of drops including different number of cells.

5.5. Full Droplet Screening Workflow and Observation of Cell Viability

In order to prove the concept of the integrated on-chip laboratory system, the effect of the drug on the individual cells confined in drops should be investigated after completing the experimental characterization of microfluidic sub-units. For this purpose, tests were performed using the droplet forming chip depicted in Figure 5.15.

Before the test, it is decided to use fluorescein diacetate and propidium iodide (FDA-PI) for live/dead cell staining. In this point, FDA is taken up by cells which convert the normally nonfluorescent molecules into the metabolite fluorescein which exhibits fluorescent green after excitation. The measured signal is regarded as a parameter indicating cell viability because the conversion of molecules depends on esterase activity [139]. Conversely, PI cannot pass through the intact membrane of living cells. It can permeate through decomposed areas of the membranes of dead cells and is inserted into the DNA double helix to exhibit fluorescent green after excitation [139]. Thus, dead cells are stained by red (PI) and viable cells will be stained by green (FDA).

Before introducing the oil to the device, cell culture medium was carried to the flow-focusing junction in a controllable manner by using a vacuum to prevent it from

wetting oil channel or chamber. Then, the oil phase introduced to PDMS droplet generation and incubation device. Finally, the device operated by tuning vacuum pressure at the outlet in order to obtain desirable droplet diameter.

Primarily, a control experiment was performed to observe how long the cells could live in droplets without the drug. A most important problem encountered during tests was the droplet shrinkage due to the low humidity of the test environment. Moreover, the air permeability of the PDMS material is relatively high that causes drying. The experiments were carried out in the cleanroom where continuous air flow exists with a room temperature of 18 °C and a humidity of %17. This leads to the droplet volume to shrink in a short period of time. Figure 5.17 illustrates the encapsulated cells in a serpentine channel region and the change in FDA staining over time. The test has been performed until the droplets lost their stability due to shrinkage. The level of cell fluorescence intensity was measured over time using an analysis method known as corrected total cell fluorescence (CTCF).

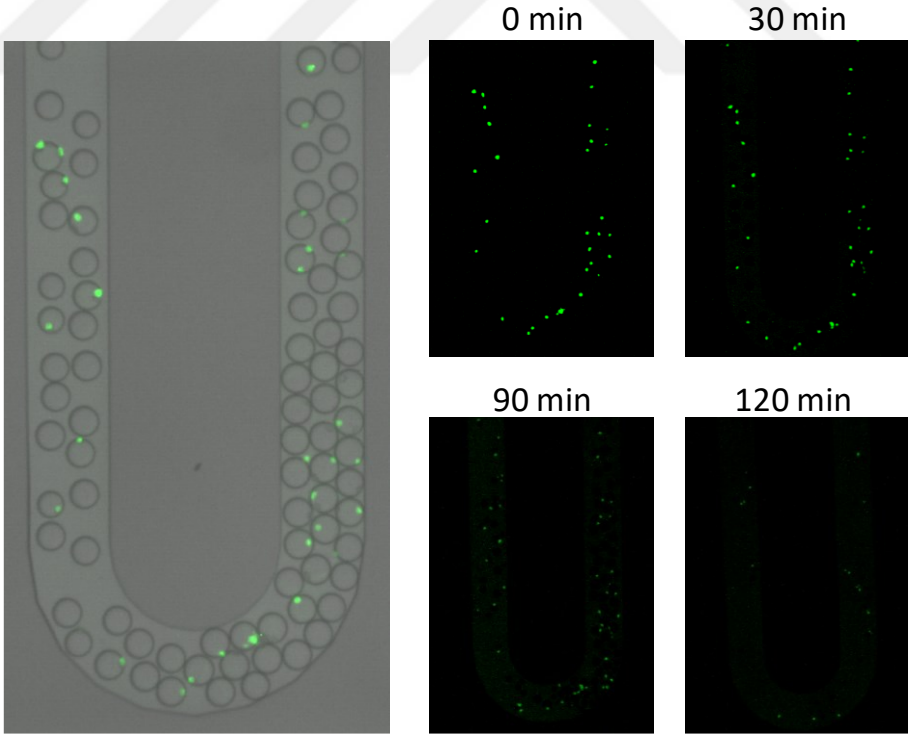

Figure 5.17. FDA staining of control experiment over time.

While extracting fluorescence signal from the microscopic images, the stages which are illustrated in Figure 5.18 is used. First, the color channels of the RGB image are split because the most process tools of ImageJ operate better for 8-bit images (b). Then, LUT is applied for the corresponding channel (for example, red is for red channel of PI) to introduce color to the image (c). The brightness and contrast of the image are autocorrected to extract information (d). After that, use the region-of-interest (ROI) tool to select a region encompassing a part of a cell together with some background, and reset the image while ROI is still active. Then, use the Auto correction again (e). The stretch will then be based on the intensities of the ROI (f).

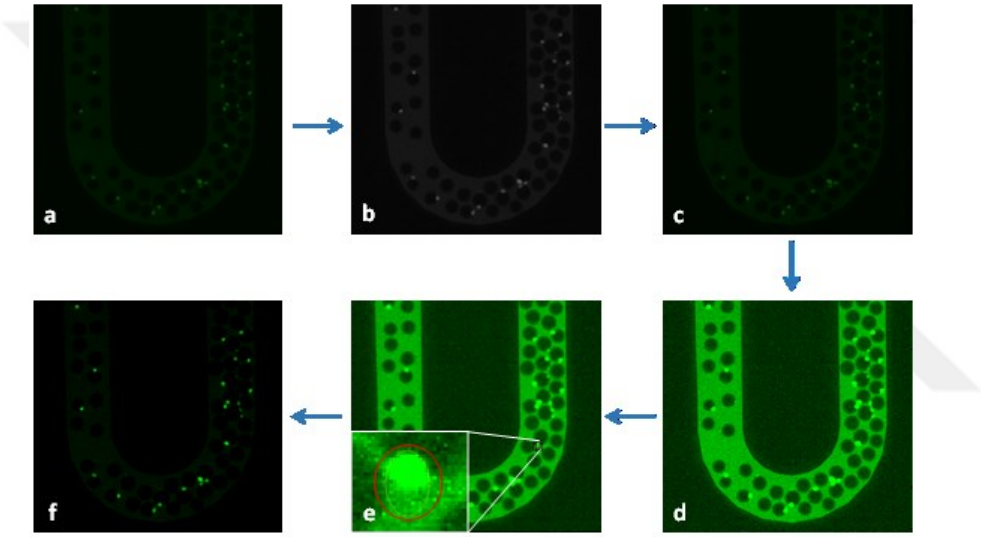

Figure 5.18. Processing stages of florescence images in ImageJ.

Image processing stages are applied for an enhancement in the visualization of images. For extracting CTFC graph, auto-corrected images can be used without hesitation because the average background is subtracted from the integrated density for every pixel identifying the cell during the calculation of corrected intensity values. CTCF graph corresponding to the control group is shown in Figure 5.19. For control group, although the cells are stained with PI, no red shift of the excitation is observed which indicates any cell death did not occur within the observation period of 2 hours. The decrease in the fluorescence brightness of fluorescein can be explained by the photobleaching behavior of the dye.

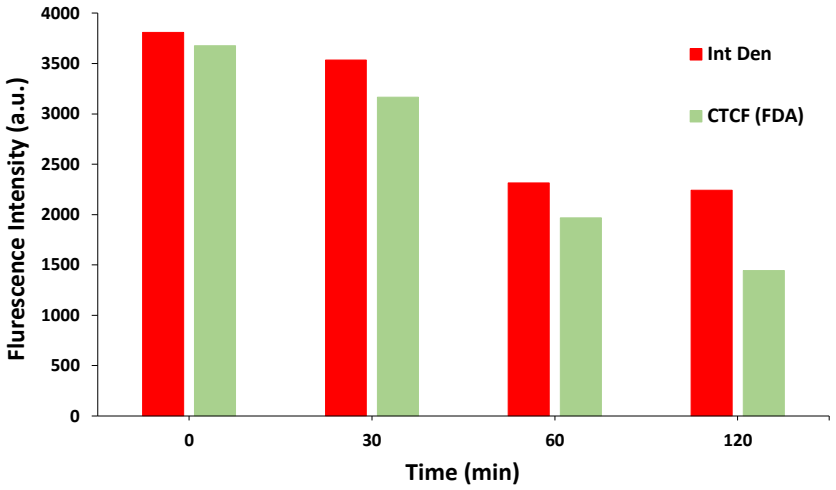

Figure 5.19. CTFC graph of FDA fluorescence intensity to measure the signal serves as an indicator for viable cells.

Moreover, another experiment was conducted by adding 20 µM doxorubicin into cell culture medium. This drug concentration corresponds to IC50 value of dox for 6 hours of incubation time. The cell culture was introduced into the device following 6 hours of incubation. After this incubation time, it is expected to observe sufficient dead K562 cells within a time frame of 2 hours as observed in six-well experiments done by biology department before. The fluorescence microscopy images which are obtained during the experiment are depicted in Figure 5.20.

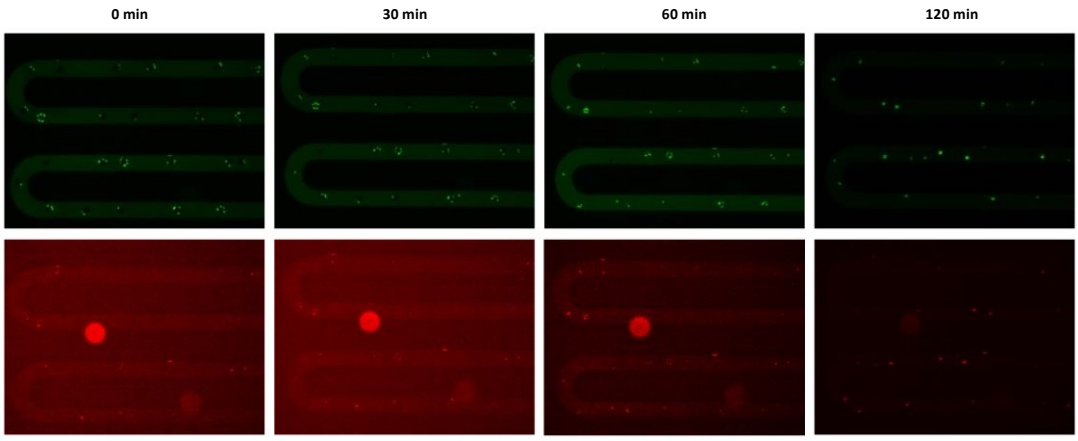

Figure 5.20. Live-dead assay. The upper row shows FDA staining (green) while the bottom row indicates PI staining (red).

Currently, the cell viability in droplets could be observed for at most 2 hours in PDMS channels due to humidity conditions of the laboratory environment. It is observed that all staining agents were functioned properly. From CTFC results which are given in Figure 5.21, it can be interpreted that the brightness of FDA decreases whereas that of PI increased as some of the cells dies in response to doxorubicin concentration of 20 µM. By using a chemotherapy agent in high concentration, multiple cell deaths are triggered and can be observed from increasing fluorescence intensity of PI over time as an indicator for dead cells.

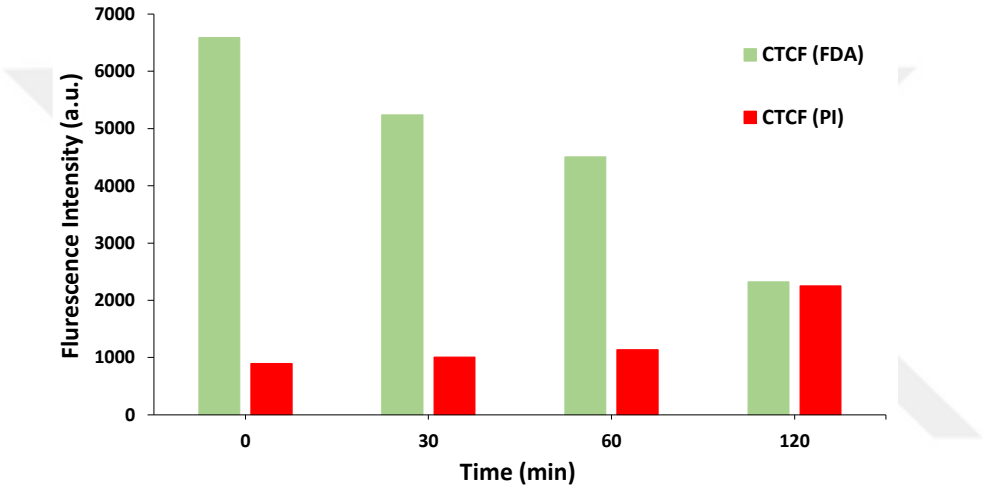

Figure 5.21. Time-dependent effect of 20 µM Dox on individual cells trapped in the droplets.

CHAPTER 6

NORMALLY CLOSED ELECTROSTATICALLY ACTUATED MICROVALVES

Microvalves are one of the most essential microfluidic components which are employed in regulating the timing, rate, and location of the flow along microchannels and crucial for systems which deliver complex functionality. Apart from flow regulation, applications of microvalves involve the prevention of the flow by behaving as an on/off switch and sealing of the gas or liquid samples in desired places. In this regard, a major impediment for complete miniaturization and victorious commercialization of fully integrated microfluidic devices is the development of dependable microvalves.

Microvalves can be classified roughly under two main categories depending on operation principle: active microvalves which need external energy for actuation mechanism and passive microvalves whose operational mode is directly determined by the flow they control without any source of external energy. Both types can utilize mechanical moving parts which convert an energy input into mechanical movement or non-mechanical moving parts incorporating smart materials. Passive microvalves which are mostly incorporated in the design of micropumps are confined to open under forward pressure, so they indicate a diode-like behavior. Moreover, the microvalves also can be categorized into normally open, normally closed and bistable microvalves with regard to their initial configuration.

For the multidrug effect analysis system proposed in the introductory chapter, the inclusion of microvalves is crucial to ensure reliable control of drug flow and proper routing of droplets within a microfluidic device by using a single pressure source. Selective activation of the fluid flow in the desired channel path requires the utilization of independent control of microvalves during operation. Here, active microvalves

allow interference upon user request for controlling the switching behavior at any time during operation. Thus, in this chapter, after giving a brief overview regarding the different types of active microvalves and their actuation schemes, an electrostatically actuated normally closed microvalve will be presented for internal control of the fluid flow. The rest of the chapter will cover the analytical and numerical analysis of the proposed electrostatic microvalve including several design considerations such as deflection of the membrane under an applied pressure, and pull-in voltage.

6.1. Review of Active Microvalves

Mechanical active microvalves can adopt several actuation methods to accomplish the movement of the mechanical part, usually in the form of a flexible membrane. These methods mainly include magnetic, electrostatic, piezoelectric, thermal and pneumatic actuation. Active microvalves with non-mechanical parts incorporate the use of smart materials which respond to a stimulus such as the temperature or pH by changing potentially its volume. These valves primarily can be reviewed under the following groups according to pertaining actuation mechanism: electrochemical, phase change, and rheological materials.

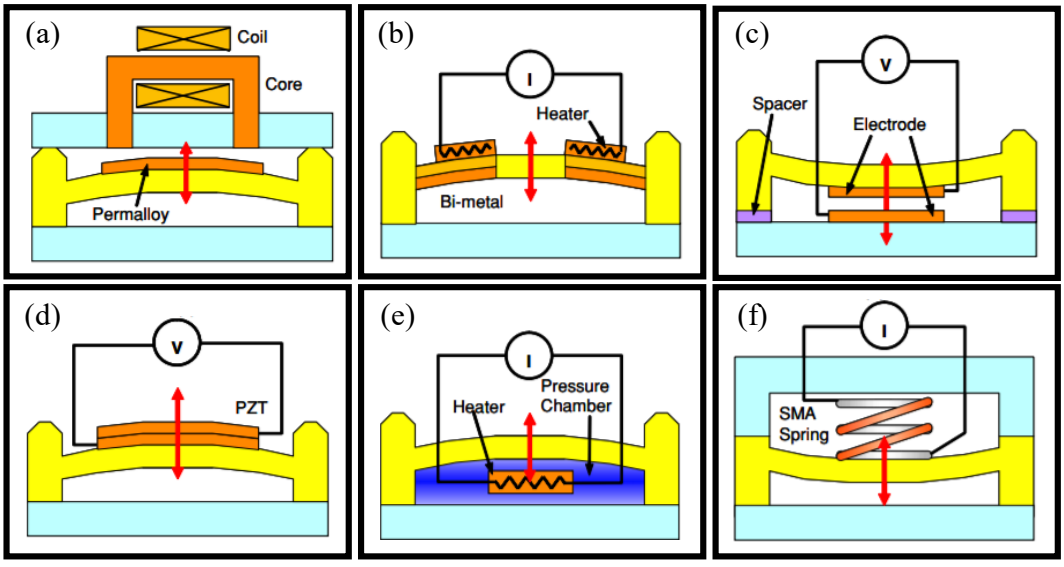

Figure 6.1. Schematic illustration of actuation types of active microvalves with mechanical moving parts: (a) magnetic, (b) thermal, (c) electrostatic, (d) piezoelectric, (e) thermopneumatic, (f) shape-memory alloy actuation [140].

Magnetic microvalves commonly consist of a magnetic core and a coil for creating a magnetic field to actuate the moving element. Electrical current passing along the solenoid coil generates a magnetic field inducing a force which pulls the core. The movable part can be integrated with either permanent magnet or coil to present a compact design, while the other is fixed. Moreover, magnetic valves can embody integrated magnetic inductors which creates a flux to magnetically move the membrane coupled with magnetic alloys. The magnetic microvalves yield a considerable force to actuate rapid large deflections of the membrane [140]; however, they mostly necessitate a complex fabrication process due to their complicated configuration which includes assembling of several frames. Especially, manual mounting of coils or magnetic core prevents batch fabrication. Moreover, the heating of the coil structure can precipitate considerable loss in efficiency [141].

Piezoelectric microvalves utilize piezoelectricity principle which applied external electric field squeezes the crystal structure and creates a mechanical strain deflecting the moving membrane. Piezoelectric actuation presents very large forces; however, very small strain in response to even very large voltages due to high Young's modulus of materials [141]. Thus, this type of actuation is suitable for micropumps where application requisites large forces but small deflections [140].

Another widespread actuation method is thermal actuation which bimetallic configuration, thermopneumatic and shape memory alloy principles substantially expand the resultant force achieving large deflections [140]. Despite their widespread usage due mainly to simple and convenient implementation in microstructures, thermal actuation mechanism suffers from several considerable drawbacks such as relatively slow response time, high-power consumption, and heat dissipation to the surroundings.

One of the most practical actuation principles is pneumatic actuation where valves are driven by external pneumatic air pressure or vacuum. Pneumatic microvalves are widely preferred in LOC applications due to their excellent rapid switching

performance, versatility and simple fabrication compatible with the introduction of especially PDMS as an elastomeric material [140]. They also enable complex manipulation of the flow and no leakage behavior because high-pressure input can be applied [142]. However, the requirement of additional bulky off-chip components such as external pressure devices, solenoid microvalves, and their connections are a serious drawback restricting the compactness of the system which is incompatible with the miniaturization and portability principles of LOC system.

For miniaturized LOC systems, electrostatic actuation scheme receives considerable attention. In electrostatic microvalves, the membrane structure is deflected by electrostatic attractive force which is generated by applying voltage difference to oppositely charge deflecting member and a counter electrode. The resulting attraction force bends the membrane onto the counter electrode while the elastic membrane will relax upon removal of the applied voltage. The electrostatic valves offer several advantages including complete on-chip integration, easy fabrication by standard micromachining processes, low power consumption, and fast response behavior [143]. However, they can provide relatively low actuation forces so respectively smaller possible deflection [143]; hence, both fluid operation pressure and electrode gap should be carefully considered specific to the application. The actuation is very effective for small gaps in the order of a couple of micrometers. Moreover, another serious issue regarding the implementation of electrostatic actuation scheme into LOC systems is the possibility of electrolysis of working fluids, electrode polarization, and electrical double layer formation. In order to render wet applications integrated with electrostatic actuation possible, these scenarios can be eliminated by the application of AC signals [144] or electrode passivation to obviate the direct contact between the electrode and working fluid [145].

Another type of active microvalves which employs non-mechanical moving structures can be adopted based on electrochemical, phase change and rheological actuation [140]. Electrochemical valving by gas generation as a result of electrolysis can offer considerable forces, thereby large deflections via relatively small voltages [146].

Phase chance actuation mechanism consumes several energy sources such as temperature, pH, electric fields or light to induce volume change in smart materials including hydrogels, sol-gel, paraffin, and also ice. Moreover, magneto- or electrorheological materials can be remotely actuated to move plugs to block channels; however, these effects generally requires high external field strengths and cannot generate appropriate deflections. These microvalves are attractive due to their simple device structure and disposability; yet their actuation usually takes long times in the order of seconds up to minutes and in some cases is irreversible. These actuation principles could be suitable for the applications if the quick response time is not crucial such as drug delivery.

Considering the types of active microvalves, the advantages and disadvantages of several actuation mechanisms are investigated up to now. Here, besides independent switching behavior which entails the use of active microvalves in the design of multidrug analysis system, since the droplet formation is completed in a matter of seconds, the microvalve should be able to respond at least in the same order. Here, mechanical active microvalves mostly exhibit much faster response times in comparison with non-mechanical ones. Moreover, they are traditionally achieved by utilizing MEMS-based micromachining where movable parts can be coupled to various actuation principles. Apart from the response time, other significant specification bases can be the available closing force and energy density. The closing force corresponds with the pressure that an actuator could generate under operation. Figure 6.2 denotes a comparison of controllability of several actuation mechanisms on the basis of response time. According to the time response range given in the figure, electrostatic microvalves elicits the fastest response in the order of 10^{-5} seconds.

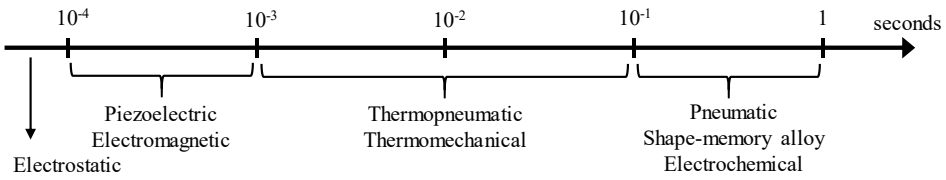

Figure 6.2. Response time behavior of different actuation mechanisms used in microvalves [147].

6.2. Design and Geometry of NC Electrostatically Actuated Microvalve

Given its important advantages including fast response time, low power usage, miniaturization capability and compatibility with standard microfabrication methods, electrostatic actuation can be considered as a reasonable candidate for the controlling of microvalves in the multidrug analysis system.

To circumvent the drawback regarding available low actuation forces which are strongly depend on the gap between electrodes, moving diaphragm of the normally closed electrostatic microvalve is placed under the fluid channel and the flow is blocked by a straight wall on the top of the diaphragm which acts as a valve seat; thus, a deflection in the range of few microns will be enough to allow the fluid to pass underneath the valve seat during operation. Furthermore, placing the valves underneath the channel also enables a reliable actuation mechanism for wet MEMS and microfluidic applications because the electrolysis of fluid samples is avoided. Since the initial configuration of microvalves is normally closed, the power will be consumed for only a very short time to change the state of the valve by selectively accumulating charge on parallel plate capacitors in order to control drug flow and routing of the droplets. In open state, there will be no current flow so no power consumption due to steady-state behavior of capacitors.

When a DC voltage is applied across the bottom and top electrodes, an electrostatic force is exerted on the diaphragm, pulling it towards the bottom electrode. As expected, the diaphragm deflects more while increasing applied voltage. At a certain voltage, namely pull-in voltage, it suddenly collapses down on the fixed ground. As the applied voltage increases further, the touch area of diaphragm expands. Here, an actuation potential can be defined where the touch area is feasible for appropriate values of the applied voltage to allow desired flow. Another force applied to unit area of the diaphragm is the fluidic pressure which should also be considered. This pressure also tends to move the diaphragm down although the microvalve is in closed state, so engenders a leakage behavior and limits the withstanding pressure capacity of the

valve. The schematics in Figure 6.3 illustrates the conceptual cross-sectional view of the valve structure and different states of operation. The first version of normally closed electrostatic microvalve structure is designed by Assoc. Prof. Dr. Ender Yıldırım [148].

In the design of the microvalves, parylene is selected as the structural material for both elastic and dielectric properties. To actuate the movement by electrostatic forces, a thin gold layer will be implemented on the diaphragm.

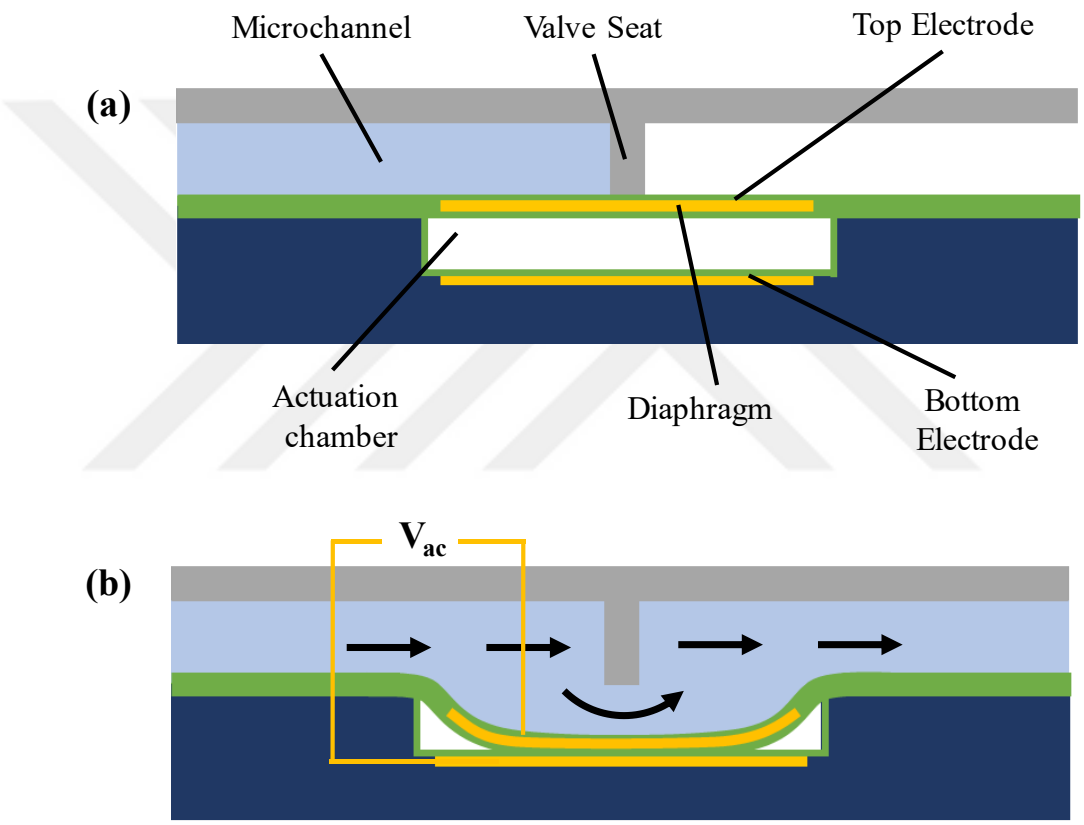

Figure 6.3. The structure of electrostatic microvalve and operation states. (a) Closed state. (b) Open State.

6.3. Modeling of Electrostatic Microvalves

Initially, a description of the parameter set which is involved in the analytical and numerical analysis of electrostatic microvalves is listed in Table 6.1 and geometrically illustrated in Figure 6.4.

Table 6.1. *Parameters and material properties involved in the design of electrostatic microvalve.*

Design Parameters	Mechanical Properties	Electrical Properties
Diaphragm radius (a = 300 µm)	Elastic modulus of parylene (E_p=3.2 GPa)	Dielectric constant of parylene (ε_p=3.15)
Gap (g = 7 µm)	Elastic modulus of gold (E_{au}=77 GPa)	Dielectric constant of air (ε_{air}=1)
Parylene thicknesses (t_1, t_3, t_4) = (1 µm,3.5 µm,1 µm)	Poisson ratio of parylene (v=0.33)	The permittivity of vacuum (ε_0=8.85x10^{-12} F/m)
Top Electrode thickness (t_2 = 0.2 µm)	Poisson ratio of gold (v=0.42)	

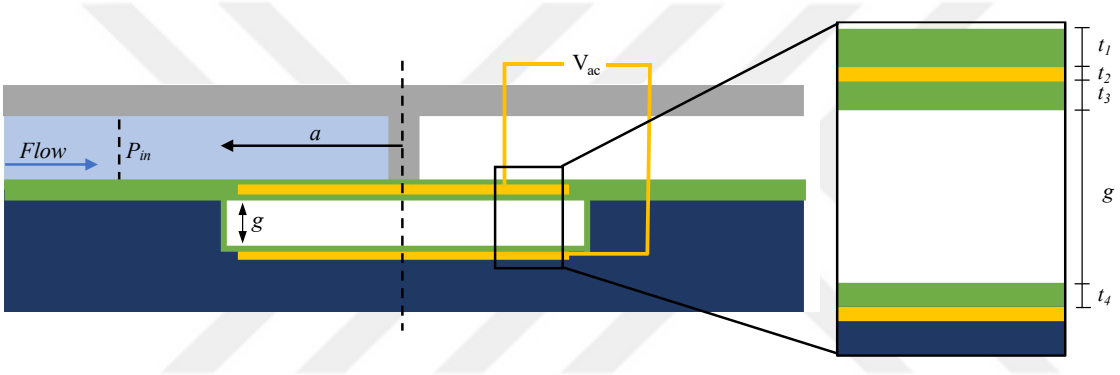

Figure 6.4. Geometric parameters involved in the design of the microvalves.

6.3.1. Parallel-Plate Approximation

A simple approach to model behavior of the electrostatic actuator is the parallel-plate capacitor approach derived from the coupling between electrical and mechanical domains (Figure 6.5). In this model, two parallel plates are separated by a gap (g) and one of which is movable in the vertical direction. Considering the mass-spring model, an imaginary linear spring suspends the upper plate and exerts an elastic restoring force on the plate. By applying DC voltage between parallel plates, the movable plate deflects.

The equilibrium of mechanical and electrostatic forces determines the value of deflection where k is the stiffness coefficient of the linear spring, g is the initial gap

between the circular plates, A is the area of the circular plates, V is the applied potential, w is the deflection.

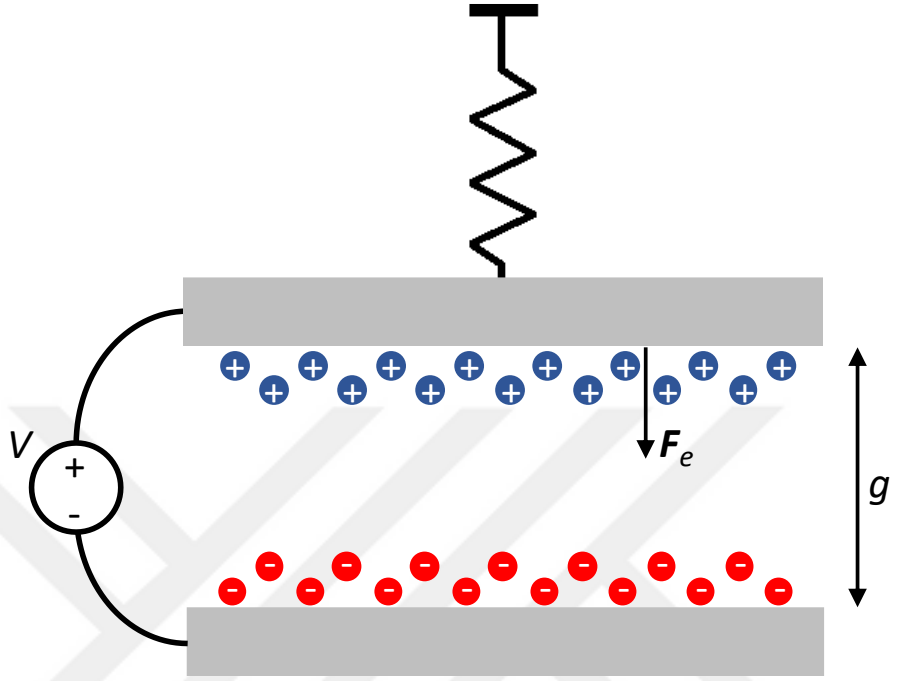

Figure 6.5. Schematic illustration of the parallel-plate approach.

If the applied potential is smaller than a specific critical value of applied voltage, equation (6.1) reaches a stable equilibrium eventually because the spring force, namely elastic restoring force of the plate, contends with the electrostatic force.

$$kw = \frac{\varepsilon A V^2}{2(g-w)^2} \tag{6.1}$$

However, a critical voltage is reached, electrostatic forces become greater than the mechanical force; thus, the diaphragm suddenly collapses onto the bottom plate. This is called the pull-in phenomenon where the system becomes unstable because of excessive electrostatic force. Here, the derivative of the net force is larger than zero, the system resides at a local minimum and is stable. However, if it is smaller, the system is in an unstable equilibrium state. The pull-in occurs when the derivative of the net force equals to zero at some value of applied voltage. Then, according to this

stability criteria, the ratio of pull-in displacement to the initial gap between plates can be found as $w_{PI}/g = 1/3$ and correspondingly a general formula for pull-in voltage (V_{PI}) is obtained as follows:

$$V_{PI} = \sqrt{\frac{8kg^3}{27\varepsilon A}} \tag{6.2}$$

However, this simple approach might hold accuracy when the displacement due to exerted electrical force is much smaller than the thickness of the diaphragm. However, in the case of the proposed electrostatic actuator, the deflection is comparable with the plate thickness; hence, this approximation renders inaccurate results mainly because it assumes piston-like displacement of a linear spring, ignores fixed boundary condition at the circular edge, non-uniform electrostatic force due to shape of the plate during deflection, and nonlinear stretching of the diaphragm. Thus, a more elaborated model should be defined by taking large deflection into consideration.

6.3.2. Uniformly Loaded Circular Plates with Large Deflections

In order to characterize the behavior of the microvalves under an applied DC voltage, first clamped circular plates where the displacement under uniform load is large should be studied. Normally, if the deflection is small compared to the plate thickness, the strain due to the middle plane stretching can be neglected. However, for the case in which the deflection is larger than the thickness but still small when it is compared with the other dimensions, the calculations should be advanced to cover the strain of the middle plate to obtain more realistic behavior of the plate under uniform pressure.

For circular plate with the boundary condition of clamped edges under a uniform load, the shape of the deflection (w) can be defined by the basic plate theory as a function of the radial position (r) where a is radius of the diaphragm and w_0 is the maximum deflection which occurs at the center of the plate as follows:

$$w = w_0\left(1 - \frac{r^2}{a^2}\right)^2 \tag{6.3}$$

It is important to note that the average plate displacement (6.4) is equal exactly to one-third of the peak deflection.

$$w_{avg} = \frac{\int_0^a 2\pi r w(r) dr}{\pi a^2} = \frac{w_0}{3} \tag{6.4}$$

The radial displacement (u) due to stretching can be represented as a function of the position (6.5) where the terms of function are selected to satisfy the conditions that the radial displacement must vanish at the clamped edges and the center of the plate.

$$u = r(a-r)(C_1 + C_2 r + C_3 r^2 + \cdots) \tag{6.5}$$

Here, a useful formulation to approximately estimates the deflections is obtained by applying the energy method. The total strain energy of the plate including the effects of both bending and stretching can be used to derive large deflections by using the principle of virtual displacements where total work exerted by external forces should be equal to the corresponding change in strain energy for assumed infinitely small variation in displacement.

In order to be able to acquire the corresponding strain energy due to bending of the plate, some useful definitions regarding the mechanics of materials should be denoted beforehand. First, the stress components can be defined by the material strain where E and v are elastic modulus and Poisson ratio of the plate material, ε is the strain in the corresponding direction, and where z is the direction of the deflection perpendicular to mid-plane. In the equations (6.6) and (6.7), only the effect of curvatures of the middle surface is included by assuming the deflection is small; thus, the transverse strains in the middle plane is ignored. Moreover, when an axisymmetric load is distributed with regard to the center, the plate deflection w becomes independent of θ, shearing stress components can be neglected.

$$\sigma_r = \frac{Ez\left(\kappa_r + v\kappa_t\right)}{1-v^2} = -\frac{Ez}{1-v^2}\left(\frac{\partial^2 w}{\partial r^2} + \frac{v}{r}\frac{\partial w}{\partial r}\right) \tag{6.6}$$

$$\sigma_t = \frac{Ez\left(\kappa_t + v\kappa_r\right)}{1-v^2} = -\frac{Ez}{1-v^2}\frac{1}{r}\left(\frac{\partial w}{\partial r} + v\frac{\partial^2 w}{\partial r^2}\right) \tag{6.7}$$

By using Hooke's Law, the definitions of the radial and tangential bending moments M_r and M_t is given in the following equations where h is the diaphragm thickness.

$$M_r = \int_{-h/2}^{+h/2} z\sigma_r dz = -\frac{Eh^3}{12\left(1-v^2\right)}\left(\frac{\partial^2 w}{\partial r^2} + \frac{v}{r}\frac{\partial w}{\partial r}\right) = -D\left(\frac{\partial^2 w}{\partial r^2} + \frac{v}{r}\frac{\partial w}{\partial r}\right) \tag{6.8}$$

$$M_t = \int_{-h/2}^{+h/2} z\sigma_t dz = -\frac{Eh^3}{12\left(1-v^2\right)}\left(\frac{1}{r}\frac{\partial w}{\partial r} + v\frac{\partial^2 w}{\partial r^2}\right) = -D\left(\frac{1}{r}\frac{\partial w}{\partial r} + v\frac{\partial^2 w}{\partial r^2}\right) \tag{6.9}$$

D is the flexural rigidity of diaphragm in the following form.

$$D = \frac{Eh^3}{12\left(1-v^2\right)} \tag{6.10}$$

Eventually, the strain energy arises from bending can be derived from the work done by the radial and tangential bending moments and can be defined by (6.11).

$$\begin{aligned} V &= -\frac{1}{2}\int_0^a\int_0^{2\pi}\left[M_r\left(\frac{\partial^2 w}{\partial r^2}\right) + M_t\left(\frac{1}{r}\frac{\partial w}{\partial r}\right)\right] r d\theta dr \\ &= \frac{1}{2}D\int_0^a\int_0^{2\pi}\left[\left(\frac{\partial^2 w}{\partial r^2}\right)^2 + \frac{1}{r^2}\left(\frac{\partial w}{\partial r}\right)^2 + \frac{2v}{r}\frac{\partial w}{\partial r}\frac{\partial^2 w}{\partial r^2}\right] r d\theta dr \\ &= \frac{32\pi}{3}\frac{w_0^2}{a^2}D \end{aligned} \tag{6.11}$$

Moreover, in the case of large deflections, the construction of the solution should include the strain of the middle plane of the plate to account for stretching effects. The radial and tangential strains of a point in the middle plane can be given as follows:

$$\varepsilon_r = \frac{du}{dr} + \frac{1}{2}\left(\frac{dw}{dr}\right)^2, \quad \text{and} \quad \varepsilon_t = \frac{u}{r} \tag{6.12}$$

By using Hooke's law again, in-plane normal forces N_r and N_t which precipitate nonlinear stretching of the plate can be obtained in polar coordinates.

$$N_r = \int_{-h/2}^{+h/2} \sigma_r dz = \frac{Eh}{1-v^2}\left(\varepsilon_r + v\varepsilon_t\right) = \frac{Eh}{1-v^2}\left(\frac{du}{dr} + \frac{1}{2}\left(\frac{dw}{dr}\right)^2 + v\frac{u}{r}\right) \tag{6.13}$$

$$N_t = \int_{-h/2}^{+h/2} \sigma_t dz = \frac{Eh}{1-v^2}\left(\varepsilon_t + v\varepsilon_r\right) = \frac{Eh}{1-v^2}\left(\frac{u}{r} + v\frac{du}{dr} + \frac{v}{2}\left(\frac{dw}{dr}\right)^2\right) \tag{6.14}$$

After calculating strains and stress resultants, the additional strain energy of the middle plane due to nonlinear stretching can be derived as follows.

$$\begin{aligned} V_1 &= \frac{1}{2}\int_0^a \int_0^{2\pi} \left(N_r\varepsilon_r + N_t\varepsilon_t\right) r d\theta dr \\ &= \frac{\pi Eh}{1-v^2}\int_0^a \left(\varepsilon_r^2 + \varepsilon_t^2 + 2v\varepsilon_r\varepsilon_t\right) r dr \\ &= \frac{\pi Eh}{1-v^2}\left[0.3048\, w_0^4/a^2 + 0.1167 a^6 C_2^2 + 0.3 a^5 C_1 C_2 + 0.25 a^4 C_1^2 \right. \\ &\qquad \left. + a^2 w_0^2 C_2\left(0.0127 + 0.1397v\right) + a w_0^2 C_1\left(-0.1460 + 0.2603v\right)\right] \end{aligned} \tag{6.15}$$

The constants C_1 and C_2 can be estimated by the condition that the total strain energy should be minimum at an equilibrium position of deflection which yields the following conditions.

$$\frac{\partial V_1}{\partial C_1} = 0, \quad \text{and} \quad \frac{\partial V_1}{\partial C_2} = 0 \tag{6.16}$$

Above equations give two linear equations that can be easily solved by elimination method using the addition property of the equality and the values of constants can be concluded (6.17).

$$C_1 = \frac{w_0^2}{a^3}\left(1.4157 - 0.7079v\right), \quad \text{and} \quad C_2 = \frac{w_0^2}{a^4}\left(-1.8801 + 0.3071v\right) \tag{6.17}$$

Eventually, the final form of the strain energy due to nonlinear stretching becomes a quartic function of deflection and is presented as equation (6.18).

$$V_1 = \pi D \frac{w_0^4}{a^2 h^2}\left(\frac{-2109v^2 + 3210v + 5679}{2500}\right) \tag{6.18}$$

At this point, the principle of virtual displacements can be applied to appraise deflection of the diaphragm under an applied mechanical force. From this principle, it follows:

$$\frac{d\left(V + V_1\right)}{dw_0}\delta w_0 = 2\pi \int_0^a q\delta w r dr = 2\pi q \delta w_0 \int_0^a \left(1 - \frac{r^2}{a^2}\right)^2 r dr \tag{6.19}$$

Thus, by substituting equations (6.11) and (6.18) into (6.19), the following expression can be obtained.

$$q\pi a^2 = \frac{192\pi D}{a^2} w_{avg} + \frac{81\pi D}{a^2 h^2}\left(\frac{-2109v^2 + 3201v + 5679}{625}\right) w_{avg}^3 \tag{6.20}$$

Equation (6.20) can be represented in the general form of restoring mechanical force of nonlinear spring where k_1 and k_3 are spring constants of the system where the first term represents the Hooke's law term and the second term, characteristic of a Duffing spring (6.21). For small deflections, the effect of cubic nonlinearity arising from axial extension due to large deflections can be ignored, and the deflection under a uniform load is purely linear.

$$F_m = k_1 w_{avg} + k_3 w_{avg}^3 \tag{6.21}$$

In the above calculations, the effect of the top electrode is not included. Despite being expected to be much thinner than the parylene-C diaphragm, its stiffness is much greater. Thus, its effect should be taken into consideration by recalculating the regarding moments and stress resultants. Actually, the diaphragm structure can be interpreted as a laminated composite plate which consists of three plies (Figure 6.6).

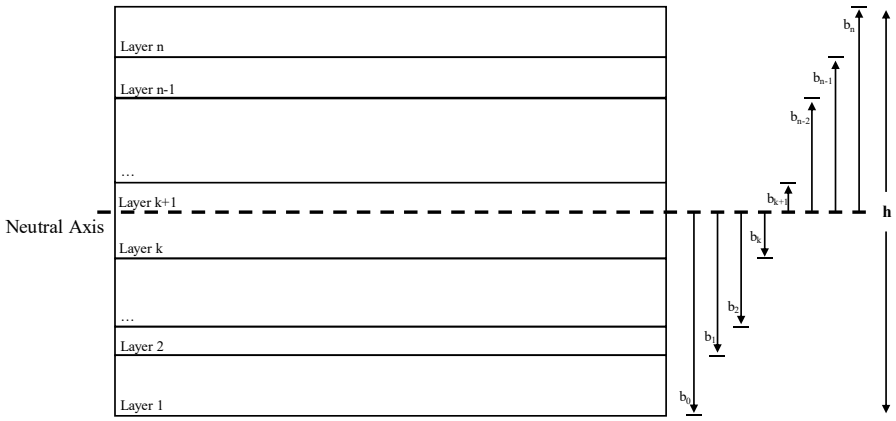

Figure 6.6. Schematic illustration of the cross-section of a laminated composite material.

In order to include the effect of implementing electrode on the diaphragm, the total strain energy of the plate should be written after recalculating moment and force stress resultants for the laminated composite plate with respect to (6.22) and (6.23) where $b_{k\text{-}1}$ is the distance from the neutral plane to the bottom of kth ply.

$$M_r = \sum_{k=1}^{n}\left(\int_{b_{k-1}}^{b_k} \sigma_r z dz\right), \quad \text{and} \quad M_t = \sum_{k=1}^{n}\left(\int_{b_{k-1}}^{b_k} \sigma_t z dz\right) \tag{6.22}$$

$$N_r = \sum_{k=1}^{n}\left(\int_{b_{k-1}}^{b_k} \sigma_r dz\right), \quad \text{and} \quad N_t = \sum_{k=1}^{n}\left(\int_{b_{k-1}}^{b_k} \sigma_t dz\right) \tag{6.23}$$

For homogeneous plates and symmetric composite plates, the neutral plane is the middle plane where the bending stress is zero. However, since the diaphragms of the electrostatic actuator is non-symmetric, the neutral axis where the bending stress is zero should be determined for any direction beforehand. The plane of zero strain can be determined by recalling that the stresses through the cross-section must be in equilibrium. Thus, the total force calculated by integrating the radial and tangential stress components around the neutral axis over the cross-sectional area should be zero. The location of the neutral plane can be determined by solving equation (6.24). The formulation can be simplified under the assumption that the bending curvatures are same for all plies because they are intact. Moreover, since the diameters of the plies

are same, the area integral reduces to a line integral over the thickness of the plate around the neutral axis.

$$\sum F = \int_A \sigma_r dA = 0 \tag{6.24}$$

By assessing the equations in (6.22), the homogenized flexural rigidity of a composite plate can be expressed by the following general formula to be substituted into equation (6.11).

$$D = \frac{1}{3}\sum_i^n \frac{E_i\left(b_i^3 - b_{i-1}^3\right)}{1-v_i^2} \tag{6.25}$$

Moreover, if equations (6.23) are analyzed for calculation of in-plane forces to obtain strain energy due to stretching of a composite plate, following values can be substituted into equation (6.18) where D_i is the flexural rigidity of ith ply calculated by (6.10).

$$\frac{D}{h^2} = \frac{\sum_i^n D_i \dfrac{\prod_i^n t_i^2}{t_i^2}}{\prod_i^n t_i^2}, \quad \text{and} \quad v = \frac{\sum_i^n D_i v_i \dfrac{\prod_i^n t_i^2}{t_i^2}}{\sum_i^n D_i \dfrac{\prod_i^n t_i^2}{t_i^2}} \tag{6.26}$$

6.3.3. Electrostatic Actuation and Pull-in Voltage

In order to obtain the electrostatic force acting on the diaphragm, first, the electrical capacitance (6.27) between the moving top and fixed bottom electrodes should be calculated by including the shape function of the deflection.

$$\begin{aligned} C &= \int_0^a \frac{2\pi r\varepsilon_0}{h - 3w_{avg}\left(1-\dfrac{r^2}{a^2}\right)^2} dr = \frac{2\pi\varepsilon_0}{h}\int_0^a \frac{r}{1-\dfrac{3w_{avg}}{h}\left(1-\dfrac{r^2}{a^2}\right)^2} dr \\ &= \frac{\varepsilon_0\pi a^2}{h}\frac{1}{2\sqrt{3w_{avg}/h}} In\left(\frac{1+\sqrt{3w_{avg}/h}}{1-\sqrt{3w_{avg}/h}}\right) = \varepsilon_0\pi a^2 \frac{\arctan h\left(\sqrt{3w_{avg}/h}\right)}{\sqrt{3w_{avg}h}} \end{aligned} \tag{6.27}$$

where $h = g + (t_3 + t_4)/\varepsilon_p$. Normally, fringing fields which are peripheral electric fields outside the volume between two parallel plates causes an increase in the capacitance. However, for the proposed actuator, these fields do not considerably affect the capacitance because the gap between the electrodes is much smaller compared to the planar dimensions of diaphragm. Thus, the effects of fringing fields excluded during formulation.

Moreover, the first derivative of capacitance with respect to w_{avg} (6.28) is assessed to be used in the electrical force definition.

$$\frac{dC}{dw_{avg}} = \frac{\varepsilon_0 \pi a^2}{2 w_{avg} h}\left(\frac{1}{1 - 3w_{avg}/h} - \frac{\arctan h\left(\sqrt{3w_{avg}/h}\right)}{\sqrt{3w_{avg}/h}} \right) \tag{6.28}$$

Finally, the electrical force acting on the diaphragm due to the applied voltage can be obtained as follows.

$$F_e = \frac{dU_e}{dw_{avg}} = \frac{1}{2} V^2 \frac{dC}{dw_{avg}} \tag{6.29}$$

After calculating electrostatic force acting on the diaphragm, the static equilibrium condition (6.30) yields the deflection.

$$F_m - F_e = 0 \tag{6.30}$$

An electrostatic actuator typically yields two possible equilibrium deflections where the first derivative of total potential energy with respect to deflection is zero which means that the net force on the diaphragm is zero. Here, if the second derivate of the stored energy at an equilibrium point is larger than zero, this point is a local minimum and the system is stable. However, if it is smaller, the system is in an unstable equilibrium state. The pull-in occurs when the second derivative of the stored energy equals to zero at some value of applied voltage where two points of equilibrium merge at an inflection point of stored potential energy. For beyond pull-in voltage, the diaphragm collapses because no equilibrium state exists and any perturbation to the

system will induce an electrostatic attraction force greater than the mechanical restoring force. According to the mentioned methodology of energy stability criteria, pull-in voltage can be computed by using the total energy expression which is given below.

$$U_t = U_m + U_e = \frac{1}{2}k_1 w_{avg}^2 + \frac{1}{4}k_3 w_{avg}^4 + \frac{1}{2}CV^2 \tag{6.31}$$

Thus, at pull-in, the first two derivatives of equation (6.31) in respect of generalized deflection becomes zero. More explicitly, $dU_t/dw_{avg} = 0$ accounts for equilibrium, and $d^2U_t/dw_{avg}^2 = 0$ accounts for stability. If both derivatives are defined at a point where both results in zero and subsequently combined, the voltage-controlled pull-in equation can be obtained.

$$\frac{dU_m}{dw_{avg}}\frac{d^2C}{dw_{avg}^2} - \frac{d^2U_m}{dw_{avg}^2}\frac{dC}{dw_{avg}} = 0 \tag{6.32}$$

This general equation can be solved for displacement, then calculated deflection (w_{PI}) can be substituted into equation (6.30) to account for the value of pull-in voltage as follows.

$$V_{PI} = \sqrt{2F_m\left(w_{PI}\right) \Big/ \left.\frac{dC}{dw_{avg}}\right|_{w_{avg}=w_{PI}}} \tag{6.33}$$

6.3.4. FEM Analysis of Electrostatic Microvalve

The finite element method (FEM) is employed as a second tool for modeling the electrostatic microvalve apart from the theoretical model of plates to validate the acquired results for deflection and pull-in behavior.

Initially, to validate the accuracy of the mechanical model including nonlinear deflection behavior due to stretching, the average deflection values for applied pressure is obtained by both the analytical model and FEM, respectively. The 2D axisymmetric model was selected as the model dimension to decrease the time of

simulation. Geometry and corresponding mesh are defined to describe structural domains as depicted in Figure 6.7.

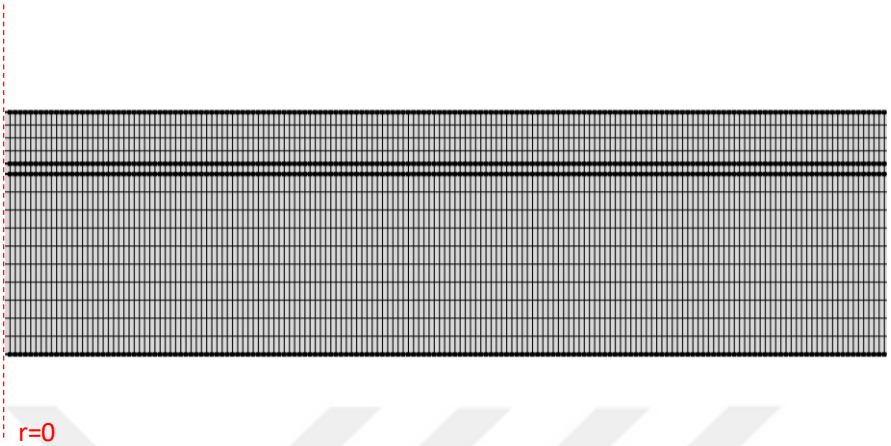

Figure 6.7. Geometry and Mesh of 2D-axisymetric diaphragm model. The geometry is scaled 15x along y-direction to visualize clearly.

Second, the pull-in voltage and the peak deflection at pull-in is calculated by the analytical model and validated with respect to FEM analysis for the accuracy of the model which includes the coupling of electrostatic and mechanical effects. The numerical model is solved in COMSOL Multiphysics ® v5.3a by coupling Solid Mechanics and Electrostatics interfaces. The computation of pull-in voltage is implemented as an inverse problem by using a global equation which searches equilibrium voltage at a given displacement whether it is stable or not. Initially set values of displacement are continuously ramped up by using an auxiliary sweep study and, the achievable maximum value of voltage for given displacements corresponds to pull-in voltage. The model geometry is similar to Figure 6.7; however, in addition to structural domains, two additional parallel adjunct domains are added to define the gap and dielectric layer on the bottom electrode.

FEM can be used for further analysis of microvalves apart from mechanical and electromechanical characterization to investigate touch mode behavior. For simulations studying touch mode, the electrostatic pressure is implemented as a boundary pressure with respect to equation (6.34) to obtain convergence by avoiding

overlapping model boundaries, namely bottom of the diaphragm and the dielectric layer of the top electrode. The upper-side of the equation yields gives exact same results with the coupled electromechanics simulations. After pull-in, the electrostatic pressure is written as a concentrated pressure field applied to the area that touches the bottom of the actuation chamber. Moreover, maximum achievable deflection is prescribed by the gap between the bottom and the top side in the z-direction.

$$q_e = \begin{cases} \dfrac{\varepsilon_0 V^2}{2\left[\left(h-w\right)+\dfrac{t_3+t_4}{\varepsilon_p}\right]^2} & 0 < w < h \\ \dfrac{\varepsilon_0 \varepsilon_p V^2}{2\left(t_3+t_4\right)^2} & w = h \end{cases} \tag{6.34}$$

Apart from touch mode behavior, by coupling the problem with Laminar flow interface to include fluid-structure interaction, the working performance of the microvalves under applied flow fields is examined. Without any applied voltage, the fluid flow can deform the elastic diaphragm. Due to the structural deformation of the diaphragm, in return, the shape of the fluidic domain deforms. Therefore, these two systems cannot be solved independently, and a two-way coupling approach should be used for fluid-solid interaction. The Navier-Stokes equations are computed on a deforming mesh, which forms the fluid domain. The deformation of the mesh with regard to the initial geometry is solved using the default smoothing. The diaphragm is fixed to bottom of the channel from its circular edge. Its top surface boundary is subjected to a load from the fluid representing the sum of pressure and viscous forces which can be defined according to (6.35) where $\boldsymbol{n}$ is the normal vector to this boundary, p is the pressure exerted on the diaphragm surface by the fluid (Pa), μ is the dynamic viscosity (Pa·s) and $\nabla\boldsymbol{u}+(\nabla\boldsymbol{u})^T$ denotes the strain-rate tensor which viscous stress tensor directly depends on. Two-way coupling method is implemented by segregated solvers where each solves a single associated field iteratively until convergence. Here, first, converged solutions of the fluid flow interpolated the solid body as one-way coupling. Then, the structural mesh is displaced, so obtained mesh

displacement values are inserted to the fluid geometry by deforming the mesh. The procedure is iterated until the desired accuracy is achieved.

$$\boldsymbol{F}_f = -\boldsymbol{n}\cdot\left(-p\boldsymbol{I}+\mu\left[\nabla\boldsymbol{u}+\left(\nabla\boldsymbol{u}\right)^T\right]\right) \tag{6.35}$$

The model geometry for fluid-solid interaction is depicted in Figure 6.8. Since the problem is half symmetric, only half of the geometry is included to relieve computation. First, the boundary where diaphragm and channel intersect is meshed by triangular elements and these mesh elements are extruded through the thickness of the diaphragm by using swept mesh functionality. Then, the fluid domain is meshed by free tetrahedral elements. Moreover, an initial tiny gap under the wall which is negligible compared to channel depth is applied to define 3D mesh elements which can be deformed during simulation study. Finally, boundary layers are defined for fluid domain only.

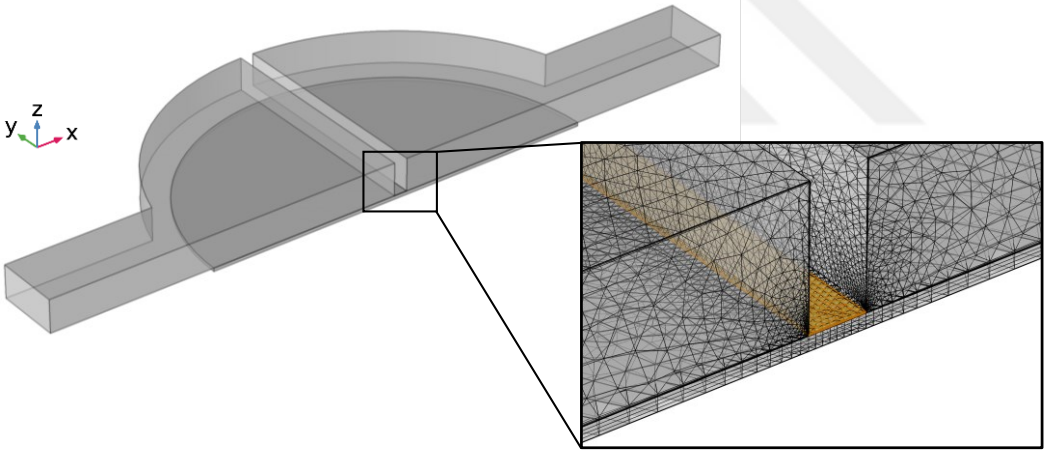

Figure 6.8. Model geometry and meshing of fluid-structure interaction problem regarding microvalves. The yellow region describes the initial gap that allows fluid flow to define deformable meshes while the solution evolves.

6.4. Analytical and Numerical Results and Discussions

The analytical formulation given in 6.3.2 and 6.3.3 is written and solved in MATLAB for given parameters in Table 6.1. Moreover, respective simulations are conducted using COMSOL Multiphysics ® v5.3a as described in 6.3.4.

Figure 6.9 shows the diaphragm displacements for an applied uniform pressure without DC voltage. When nonlinear effects due to stretching ignored, the deflection increases linearly with pressure. The addition of nonlinear spring constant, k_3, accurately captures the nonlinear effects during large deflections. For the microvalve case, nonlinear effects become apparent even at low values of applied pressure when peak displacement is comparable with the diaphragm thickness. Thus, including the nonlinear spring constant is significant for accurately modelling the proposed electrostatic microvalve.

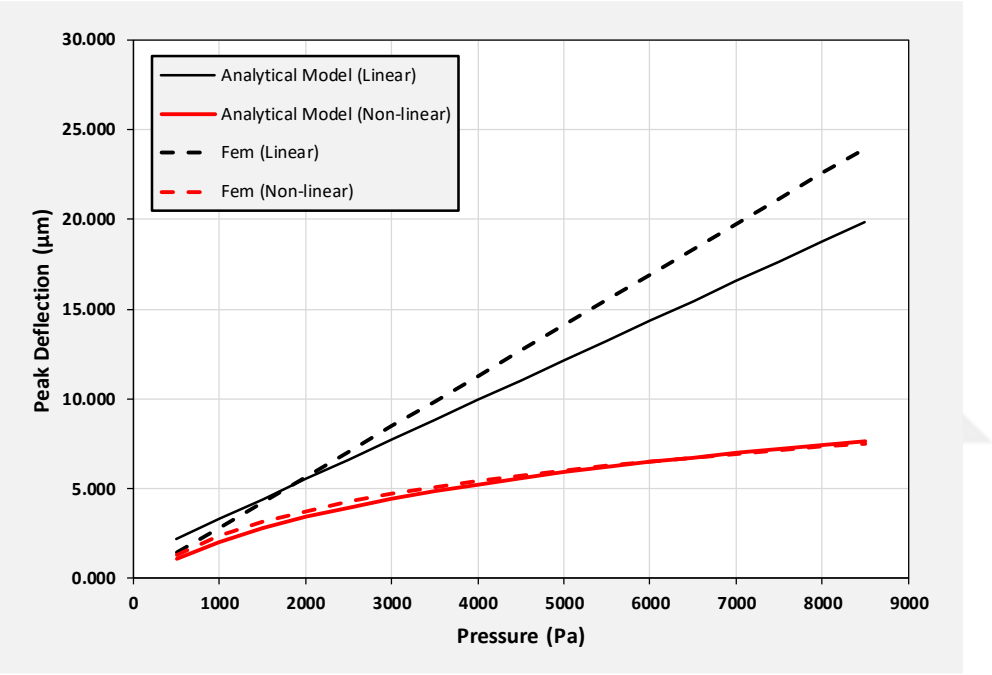

Figure 6.9. Peak displacement for applied uniform pressure values.

Moreover, the pull-in voltage and deflection are calculated by both analytical and numerical models and corresponding results are tabulated (Table 6.2). Analytically calculated pull-in voltages and displacement corresponding to pull-in voltage show accuracy with the numerical values obtained by simulations. For the nonlinear model, the relative error is 2.79% for pull-in voltage and 0.05% for peak displacement where pull-in occurs.

Table 6.2. *Obtained pull-in voltage and displacement values by analytical models and COMSOL simulations.*

Model	**Pull-in Voltage (V_{PI})**	**Pull-in Displacement (w_{PI}/g)**
Analytical (Linear)	99.95 V	0.5584
FEM (Linear)	101.90 V	0.5720
Analytical (Non-linear)	135.99 V	0.7567
FEM (Non-linear)	132.19 V	0.7571
Parallel-Plate Capacitor	113.83 V	0.3334

The following figure shows the voltage curve obtained by solving an inverse problem in COMSOL and the deflection profile of diaphragm just before the pull-in (Figure 6.10). It can be transparently observed that the peak deflection of the diaphragm which occurs at the center is approximately 5.3 µm for a 7 µm gap. Thus, this value is far different than the pull-in displacement obtained by the simple parallel-plate capacitor approach which corresponds to 1/3 of the gap distance.

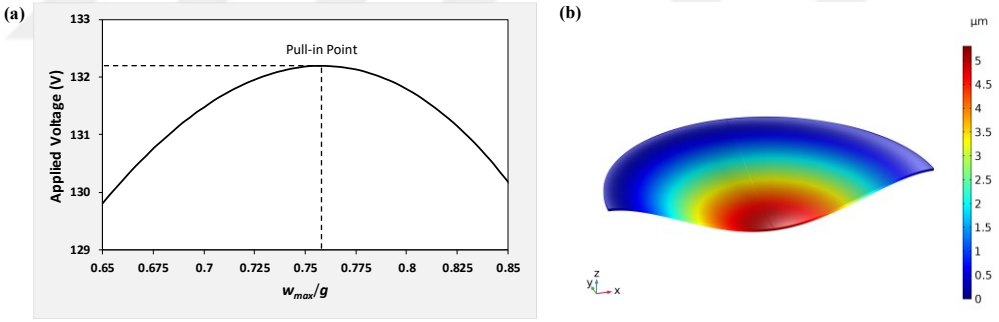

Figure 6.10. (a) Voltage curve with respect to given displacement. (b) Deflection profile of diaphragm just before electrostatic pull-in.

Moreover, as described in the subsequent section, the touch area with respect to applied voltage after electrostatic pull-in is also obtained by COMSOL. In Figure 6.11, the radius of the touch area is presented to easily compare the deflection with the diaphragm radius. As another metric, the open area under the wall of an actuated diaphragm is also obtained by integrating the amount of deflection along a line through the diameter of the diaphragm. For 250 V, the radius of the touch area is almost 135

μm. Thus, only the quarter of the total diaphragm area touches to the bottom. However, for same value of voltage, actually, almost %75 of the gap under the wall which behaves as an impediment to the flow at closed state is open.

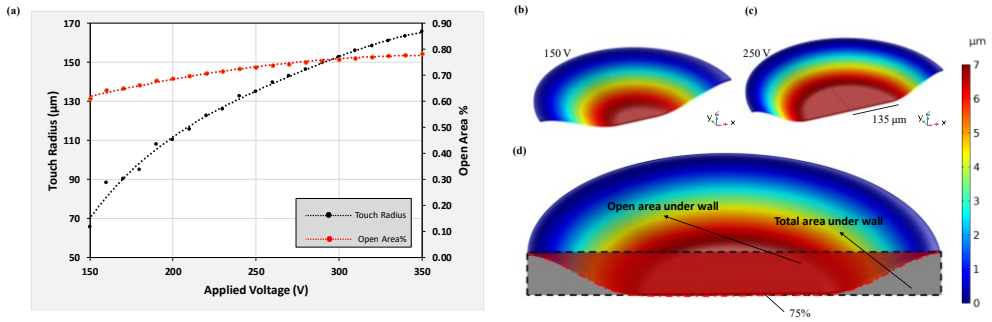

Figure 6.11. An analysis of open-state behavior of microvalves. (a) The plot illustrates open-state metrics which might be beneficial to determine the actuation voltage of microvalves. (b) Touch mode deflection profile at V=150 V. (c) Touch mode deflection profile at V=250 V. (d) Open area under the valve wall which obstructs the fluid flow at closed-state.

Finally, in order to understand the behavior of microvalves under fluid flow, the simulation study involving an electromechanics problem is coupled with fluid flow interface as described in Section 6.3.4. The corresponding results for applied inlet pressure of 10 kPa are illustrated in Figure 6.12. At 10 kPa, diaphragm deflects approximately 5 μm; so open area exceeds 30% which will cause high leakage flows while operating with positive pressure at the inlet although the applied pressure is not so high. Thus, the performances of microvalves will be tested under vacuum pressure which actuates the flow of fluid. In this case, the applied voltage should overcome the applied vacuum pressure, so calculated pull-in voltage is expected to increase.

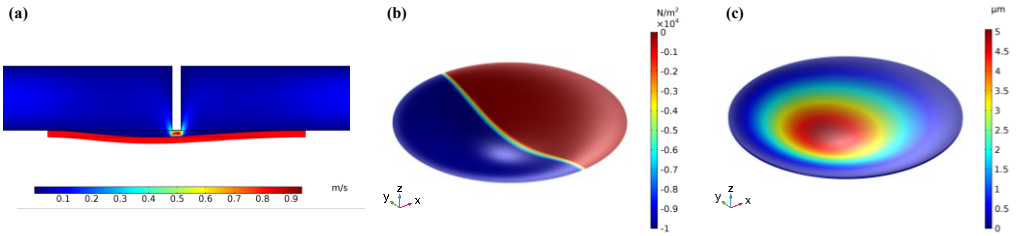

Figure 6.12. Fluid-structure interaction analysis of microvalves at P_{in}=10 kPa. (a) The cross-section of the valve representing the fluid velocity for the applied inlet pressure. (b) Sum of the pressure and viscous forces which is loaded to the diaphragm by the fluid. (c) The displacement of the mechanically moving diaphragm.

CHAPTER 7

FABRICATION AND EXPERIMENTAL VALIDATIONS OF NC MICROVALVE

In this chapter, first, MEMS fabrication of normally closed electrostatic microvalves are presented. The processes are illustrated with images and explained in detail. Fabricated moving diaphragm prototypes are tested to characterize the behavior of mechanically moving diaphragm for several key parameters such as pull-in and pull-out voltages, repeatability, response times and touch area. Eventually, PDMS microfluidic channel is integrated with micro diaphragm by plasma-assisted bonding.

7.1. Microfabrication

In this section, MEMS fabrication of normally closed electrostatic microvalves is presented. The proposed electrostatic microvalves incorporate a circular parylene diaphragm as its mechanical moving part residing over an actuation chamber which connected to ambient pressure through air vent channels. To achieve electrostatic actuation, the top electrode is defined on top of the diaphragm whereas the fixed bottom electrode is placed at the bottom of the actuation chamber. When a DC voltage is applied across the bottom and top electrodes, an electrostatic force is induced on the diaphragm, pulling it towards the fixed bottom electrode.

The layouts of the microvalve characterization device are drawn and compiled using Tanner® L-Edit® software and regarding visuals of each mask are shown in Figure 7.1. The fabrication is a five-mask process; however, it includes six lithography processes because a single mask is used for both the etching of recesses defining actuation chambers and air vents and filling them with sacrificial photoresist before coating the diaphragm layer. Parylene RIE Mask-2 can be used if parylene microchannels are preferred apart from PDMS integration which will not be included in the scope of this thesis. In summary, apart from photolithography, the fabrication

mainly consists of wet and dry etches, parylene-C coating, metal sputtering, and PECVD deposition.

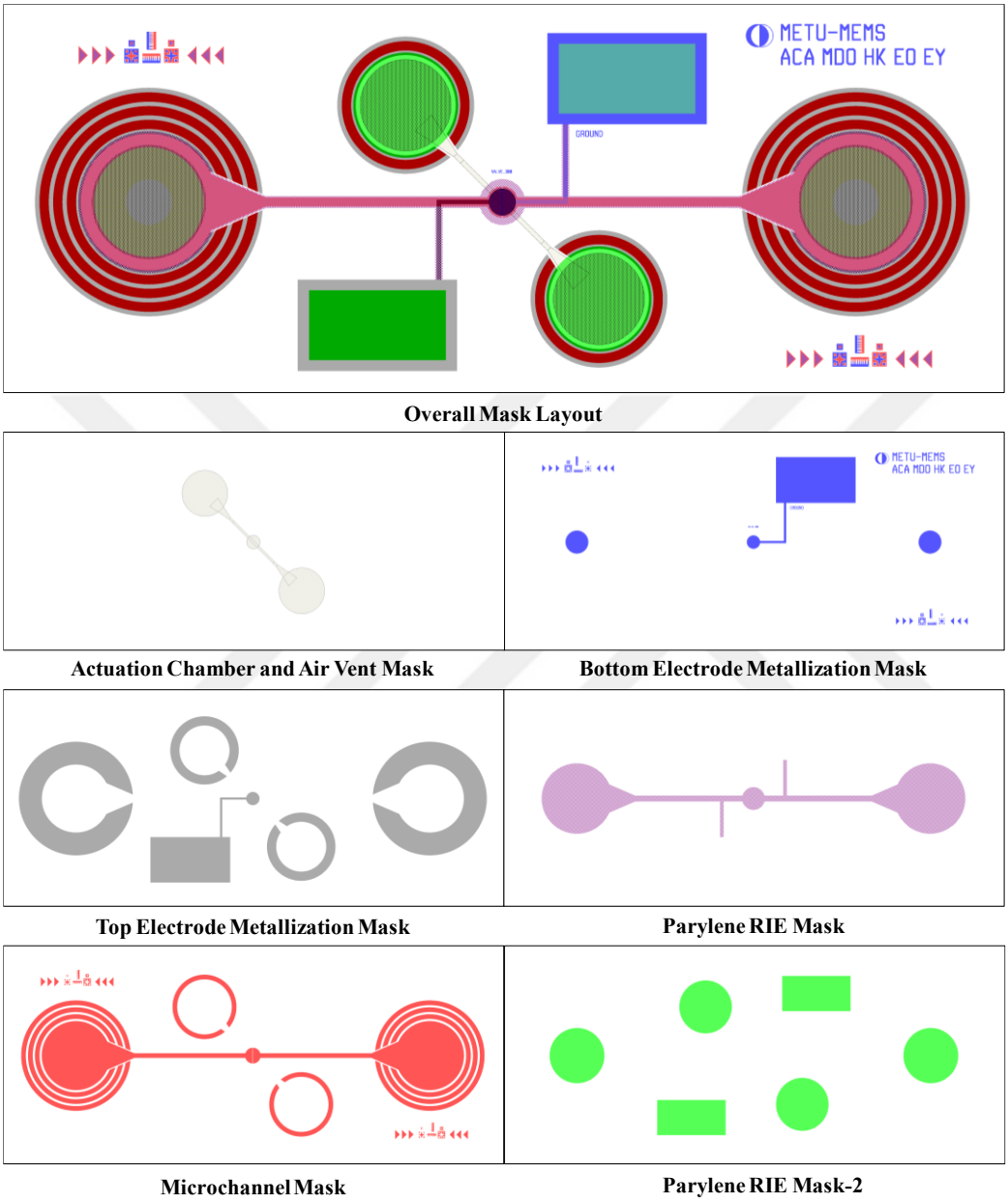

Figure 7.1. Mask layouts for every single process for the fabrication of PDMS/glass hybrid devices.

The microfabrication process steps are depicted schematically in Figure 7.2. The process flow is divided into several sequential stages and explained in the following of this section. The moving diaphragm is fabricated by conventional MEMS

technology. Then, soft-lithography is applied for microchannel fabrication. Both substrates are sealed with oxygen plasma treatment at die level to achieve a complete electrostatically actuated microvalve.

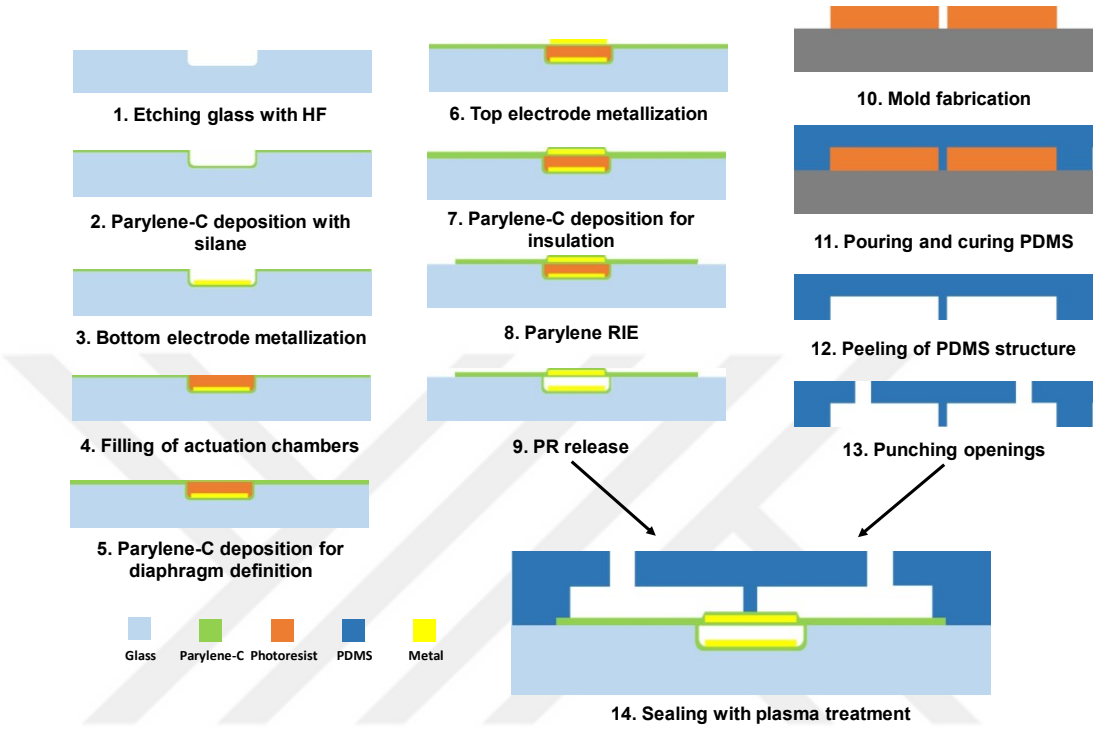

Figure 7.2. Fabrication flow schematic cross-section diagram. The structures are not drawn actual layout dimensions.

For the fabrication of mechanical moving diaphragm, a glass wafer is used as the substrate material. At the first step, actuation chambers and air vents are defined by wet etching of glass in a highly concentrated HF solution (49%). Thus, the wafers are coated with 30/300 nm thick bimetallic Cr/Au layer in order to define the masking layer for wet etching. The desired regions corresponding actuation chambers and air vent channels are patterned by photolithography resulting in a negative pattern of the chrome mask using image reversal photoresist AZ® 5214 E by using actuation chamber and air vent mask in Figure 7.1. Before starting the metal etch, all wafers are descummed for removal of photoresist residues which is remained after development. 300 nm thick Au layer at the top were etched for approximately 40 sec at commercial Transene Gold Etchant TFA. After rinsing wafers, they are descummed again in order

to oxidize chromium layer because the etching agent, namely Transene Chromium Etchant 1020, is more effective against chromium oxide. Then, the resulting layer was etched for approximately 50 sec and immersed into 2% H_2SO_4 solution for 15 sec to clean the residues off. The fabrication is continued with etching of recesses at the actuation chamber and air vent sites. The patterns are etched by hydrofluoric acid at the presence of a bimetallic mask layer for 1 min to achieve a recess depth of approximately 8 μm. Following to glass etching, PR removal was carried out by immersing the wafers into PRS 2000 stripper at 80 °C for 15 min + 15 min treatment and the bimetallic layer is removed subsequently by using corresponding commercial etchants. An additional short etch is necessary to clean diffused gold layer after chromium etch. Afterward, BHF (1:7) treatment was applied for 3 minutes to smooth sharp edges at the etch regions. Corresponding microscopic images taken after the definition of actuation chambers and air vents can be seen in Figure 7.3.

Figure 7.3. Microscopic images (5x) which are taken after glass etch.

After defining the chambers and venting channels, a 0.2 μm-thick PECVD oxide layer is deposited onto wafers to facilitate plasma bonding with PDMS channels after finalizing the fabrication of moving diaphragm.

Next, a bimetallic layer is formed by sputtering 20/200 nm-thick Ti/Au at Bestec. Then, photolithography was completed with SPR 220-7 photoresist to define the bottom electrodes regions, corresponding pads, and wires during wet etching of metal layers by using the bottom electrode mask illustrated in Figure 7.1. The gold layer was etched with commercial etchant for 30 sec while the titanium layer is removed by immersing in HF:H_2O_2:H_2O (1:1:200) solution for 35 sec. All the PR layers were then

stripped in acetone for an hour. Then, 1 µm-thick parylene-C layer was deposited onto wafers by using Silane A174 for adhesion promotion. This parylene layer serves a substrate surface which ameliorates diaphragm stiction problem after releasing of sacrificial photoresist which will be defined at the next step. It is measured that surface stiction between two parylene-C layers is much lower than the stiction of parylene to gold or oxide surfaces when devices are air dried after releasing [149]. Moreover, it also increases the dielectric strength of the electrostatic microvalves.

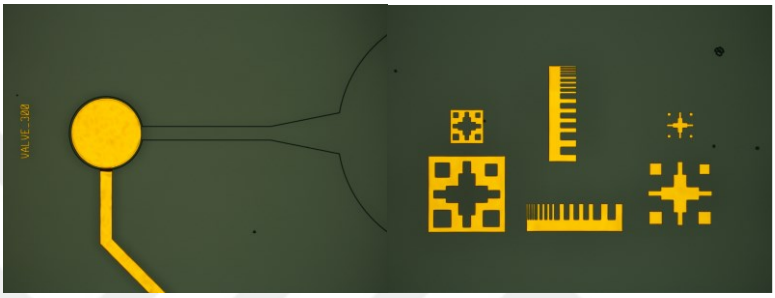

Figure 7.4. Microscopic images (5x) which are taken after bottom electrode metallization.

Next step is the filling of actuation chambers and air vent channels. After parylene-C deposition, the remaining depth is expected as 7 µm. However, the aggressive nature of concentrated HF makes difficult to precisely control the resulting etch depth; thus, the resulting recess depth can deviate up to 0.5 µm for each wafer. The final recess depth is investigated by DEKTAK surface profilometer. Thus, by optimizing the spin-speed curve of SPR220-7.0 beforehand, appropriate spin rates were selected for each wafer, so the recesses are filled with the sacrificial photoresist by using actuation chamber and air vents mask for the second time.

After completing the filling step, an undercut around the etch depth is observed because the expected isotropy ratio for this specific mask layer is ~1. Due to the undercut effect, when the filling of the chamber sites with sacrificial photoresist is finalized, a gap of approximately 7 µm gap between the edges of the holes and photoresist which is comparable with the etch depth was formed because the same mask is utilized for both definition and filling of recesses during the exposure of the photoresist. The corresponding image which is taken after filling of the actuation

chambers and air vent channels is illustrated in Figure 7.5. Subsequently, to ensure the endurance of the sacrificial photoresist during following fabrication steps, the wafers are hard-baked at 90 ºC for eight hours is completed. A subnormal temperature was selected to preserve the integrity of the underlying Parylene-C layer.

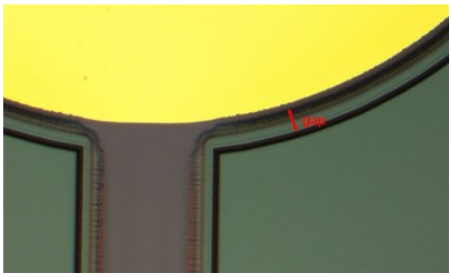

Figure 7.5. Illustration of the gap between the photoresist and the edges of the recesses (50x).

In the next step, 2.5 µm-thick parylene-C layer is deposited in order to define the moving diaphragm. Thus, the gap between the photoresist and the edges is also filled with parylene-C. Microscopic images taken after parylene deposition is illustrated in Figure 7.6.

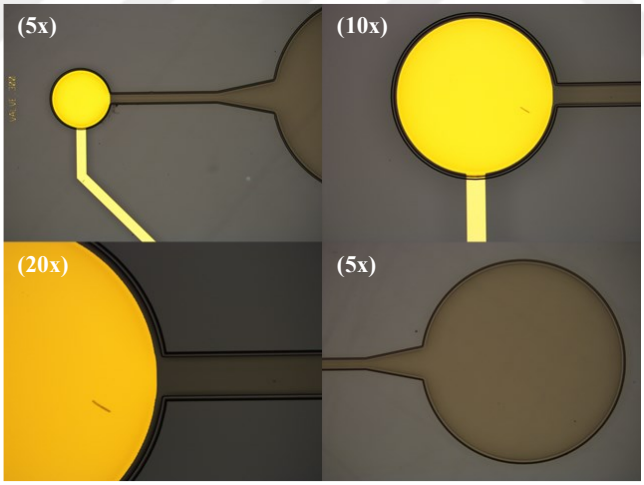

Figure 7.6. Microscopic images which are taken after 2.5 µm-thick parylene-C layer.

The same metallization process with the pattering of the bottom electrodes is used to form the top electrodes by using the top electrode mask illustrated in Figure 7.1. Later, 1 µm-thick parylene-C layer is deposited to avoid electrolysis when operating under liquid flow.

Finally, in order to render PDMS/glass hybrid devices possible, all parylene over the wafer apart from concerned locations such as valves to define the diaphragm, channels to induce hydrophobicity and metal wires to provide electrical isolation is dry etched by RIE. The masking layer is defined by 20 μm-thick AZ® 40 XT by using parylene RIE mask. The corresponding microscopic images which are taken after completing dry etching are shown in Figure 7.7.

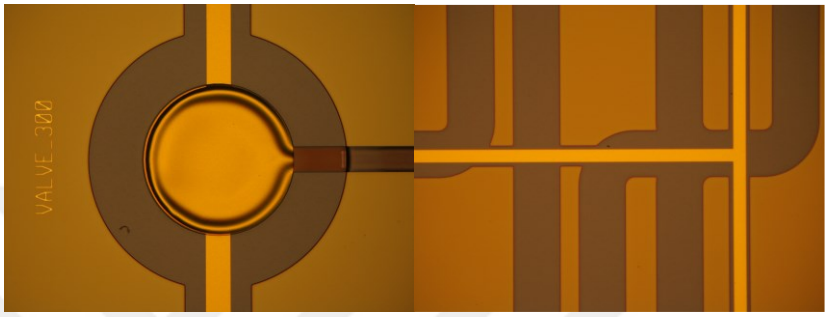

Figure 7.7. Microscopic images (10x) which are taken after parylene RIE. All parylene over the wafer apart from concerned locations including diaphragms, channels and metal wires is dry etched.

After completing the fabrication with RIE step, powder-like gold particles are observed over the surface of the wafers probably because the top electrode layer is deposited on parylene-C (Figure 7.8 (a)). To clean the surface to facilitate plasma bonding with PDMS without damaging the electrode pads and wires, a diluted Aqua regia solution is prepared at a ratio of 3:1:6 ($HCI:HNO_3:H_2O$). A short treatment of 7-8 sec is appropriate for removing gold particles residing on the wafer surface as can be in Figure 7.8 (b). Here, fabrication of the moving diaphragms is completed, and wafers are ready for dicing.

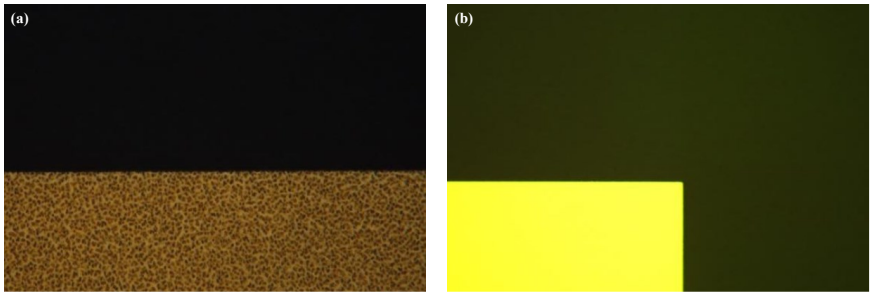

Figure 7.8. Microscopic images (50x) regarding short duration treatment with diluted Aqua regia. (a) Before treatment. (b) After treatment.

Moreover, to fabricate PDMS channels by soft-lithography as described in Chapter 5, the silicon master is made by AZ® 40 XT photoresist by using the recipe that results in 50 μm thickness. The only difference was that curing is completed under room temperature in order to avoid shrinkage of dimensions which important to precise alignment. After peeling of PDMS, the individual devices are cut by a razor blade, and inlet/outlet ports are opened using a biopsy punch. Before plasma bonding, in order to remove the photoresist on the surface of the glass, the dies are immersed in acetone and IPA for 10 min, respectively. The diaphragms are not fully released because the application of lubricants which allows the alignment of the substrates under microscope causes diaphragm stiction after drying on a hot plate.

Finally, PDMS channels are irreversibly sealed with glass dies comprising electrostatically-driven diagrams by using oxygen plasma-assisted bonding at 100 W for 90 sec. The quality of bonding is determined by modifying the exposure duration and RF power for constant oxygen flow and vacuum pressure. After the plasma treatment, a drop of lubricant which does not corrupt the plasma activated surface such as methanol, ethanol or water is dropped between the glass and PDMS to allow enough time to achieve alignment of devices. After the alignment of two substrates under a microscope, the devices were put on a hot plate at 110 °C for 5 minutes to evaporate the lubricant between them. Before, irreversibly bond two substrates, diaphragms are released by immersing into acetone for at least 2 days at die-level. After a one-day IPA treatment to ensure IPA is fully replaced with acetone, the dies are air dried. This method is the most reliable release method which prevents stiction of diaphragms due to capillary effects during evaporation. Finally, the devices are ready to be tested. The final microvalve characterization device is illustrated in Figure 7.9.

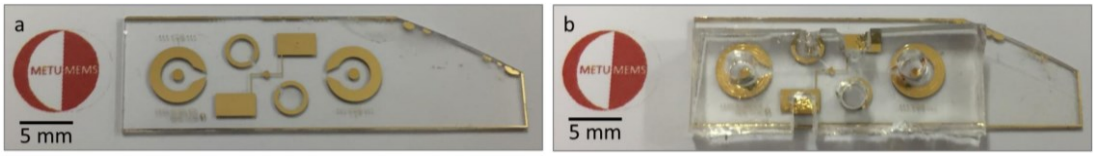

Figure 7.9. The fabricated microvalve characterization device. (a) Mechanical moving part on glass wafer. (b) Final device after integrated with PDMS microchannel.

7.2. Experimental Validation of Electrostatically Actuated NC Microvalves

There are several significant figures of merits by which a microvalve operation is evaluated: pull-in and pull-out voltages, response times, pressure range and reliability.

First, the characterization of electrostatic microvalves fabricated on glass pertaining to pull-in and pull-out voltages is completed under atmospheric pressure without fluid flow (Table 7.1). In order to obtain pull-in voltage, the applied voltage is gradually increased by 1 V-steps until diaphragm collapses to the bottom of the actuation chamber. Subsequently, the method of gradually reducing the voltage until the diaphragm returned to its initial closed state was used to determine the pull-out voltage. Pull-in voltages are measured around 122 ± 10.65 V for microvalves with 300 µm diaphragm radius. Thus, experimental values of pull-in voltages are closely consistent with numerical and analytical studies. Response time for both opening and closing states observed between 1-3 seconds for different valves. The microvalves were tested for test-retest reliability (repeatability). Thus, the diaphragms are actuated at 150 V and repeatedly cycled on/off more than 50 times without no problems.

Table 7.1. *Pull-in and pull-out voltages and response times measured for different diaphragms.*

Microvalve no:	Diaphragm Radius (µm)	Pull-in Voltage (V)	Pull-out Voltage (V)	Pull-in Response Time (s)	Pull-out Response Time (s)
1	300	130	-	1.8	1.7
2	300	112	51	3.3	2.1
3	300	111	67	1.6	1.3
4	300	135	-	1.1	1.5

After pull-in, the applied potential is increased further in order to define an operation voltage by evaluating the touch area. Figure 7.10 shows the snapshots of an example microvalve (300 µm diaphragm radius, full top electrode) which were taken while applying different actuation potential values. Touch area for different applied potential values is extracted by using ImageJ.

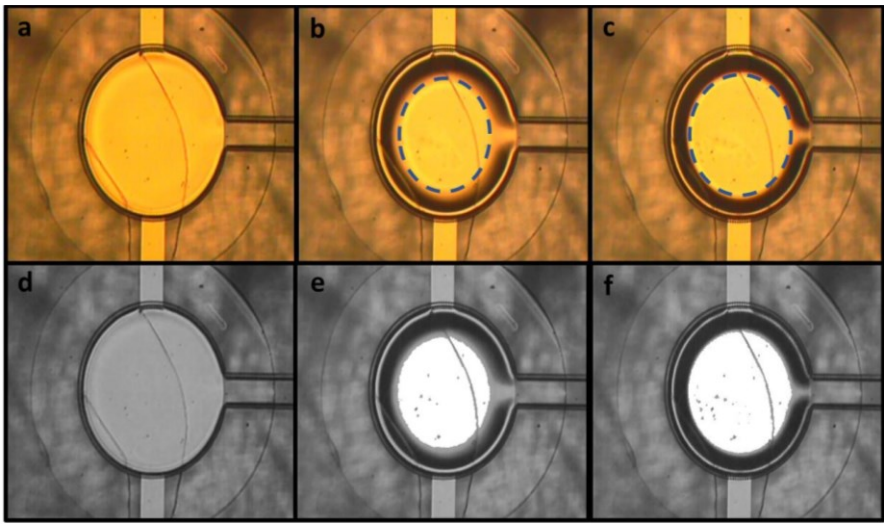

Figure 7.10. Microscopic images regarding the electrostatically-driven micro diaphragms at different applied voltages. The dashed circles denote the area touching to the bottom of the chamber. Diaphragm radius is 300 µm. (a) No voltage applied (open state). (b) V=140 V. (c) V=200 V. (d-f) Images were processed with ImageJ in order to make the touch area more visible.

In order to measure the area of the collapsed diaphragm, first, images corresponding to certain time spans which a specific voltage value is applied are extracted from videos by VirtualDub. Then, these images are imported to ImageJ as a stack by converting them into 8-bit grayscale images in order to use relevant process and analysis tools of open source software. Then, to utilize threshold function efficiently, a circular region of interest surrounding the inside of the microvalve is defined. Outside of this region is cleared for all images in the stack. Then, by using threshold tool inactively, images are segmented into features of interests representing touch area of the diaphragm. After thresholding, areas which are touching to the bottom of the actuation chamber for corresponding voltage values were measured by using particle analyze tool by showing the outline of the extracted region and measured area. While analyzing recorded videos, it is noticed that the view elongated vertically; thus, the diaphragm profile was more elliptical apart from being circular. By using normalization, spatial errors of the camera can be eliminated safely. In this point, additionally, the diaphragm area in open state is also extracted carefully in order to normalize the measured touch areas which have a scale unit of square pixels.

Finally, the corresponding results are represented graphically as percentages with respect to the total valve area (Figure 7.11). The measured experimental touch areas are much higher than the numerical results which means that a lower value for actuation voltage inducing a sufficient open area under the valve wall which allows fluid flow can be selected.

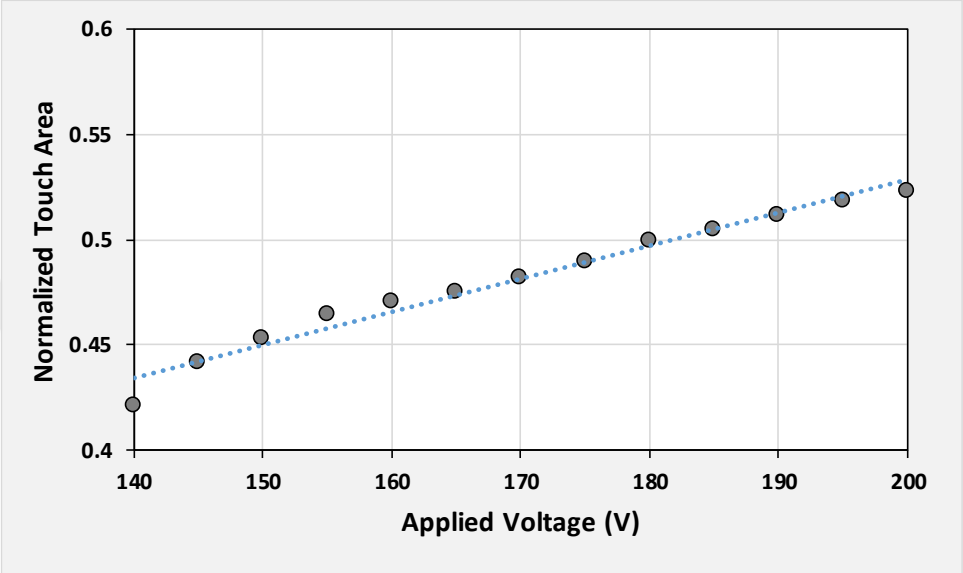

Figure 7.11. Experimental values measured for touch area of the actuated diaphragm in response to applied voltage.

Moreover, after completing the characterization of moving diaphragms, they are sealed with PDMS microchannels and tested for fluid flow characterization under applied vacuum pressure. While the working fluid is air, under outlet vacuum pressures of 0 mbar (initial condition), -50 mbar, -100 mbar, -150 mbar, and -200 mbar, the corresponding pull-in voltages were obtained as 90 V, 130 V, 150 V, 175 V, and 215 V, respectively.

The snapshots which were taken under operation is visually represented in Figure 7.12. Actually, PDMS valve wall pushes down the parylene-C membranes because they are slightly above the glass surface. Thus, it engenders a decrease in the pull-in voltage for the first case (P=0) in comparison with the initial characterization of the diaphragm without microchannels where pull-in voltage is measured around 122 V.

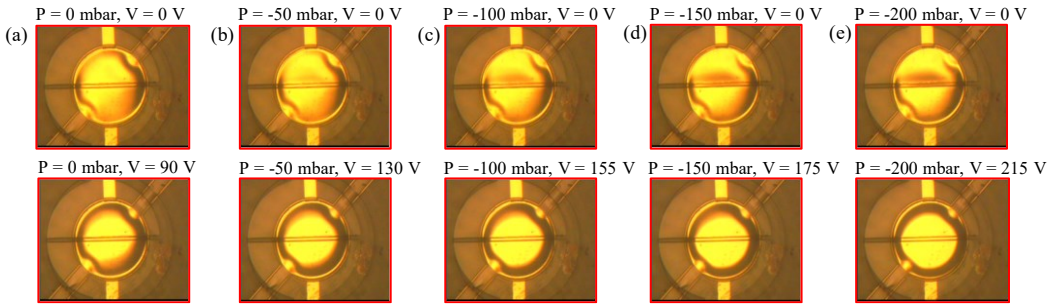

Figure 7.12. Determination of pull-in voltages under operating with vacuum pressure. (a) P=0 mbar. (b) P=-50 mbar. (c) P=-100 mbar. (d) P=-150 mbar. (e) P=-200 mbar. P is the applied vacuum pressure (mbar).

Lastly, microvalves are tested under fluid flow while working fluid is colored DI water. At an applied pressure of 10 mbar, no leakage flow is observed due probably to the high hydraulic resistance between the valve seat and the diaphragm (Figure 7.13 (a)). When the microvalve is actuated by applying 250 V, working fluid flows through the valve region (Figure 7.13 (b)).

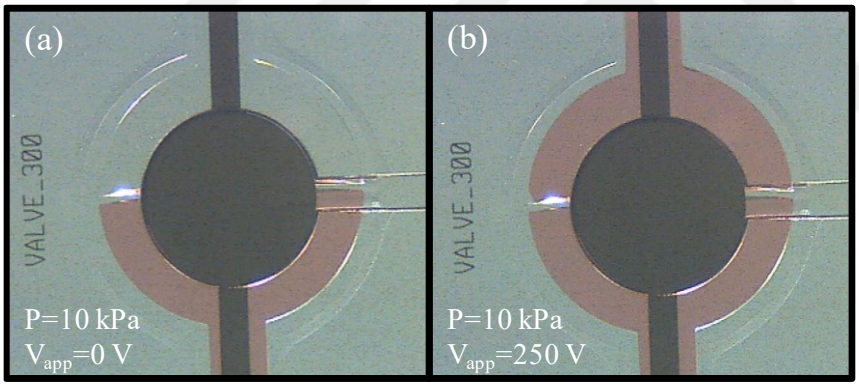

Figure 7.13. Microscopic images which indicate the operation of the electrostatic microvalve while working fluid is colored DI water. (a) The fluid is given to the microchannel by applying positive pressure of 10 kPa at the inlet. (b) The microvalve is actuated at V_{app}=250 V and allows fluid flow.

CHAPTER 8

CONCLUSION AND FUTURE WORKS

This thesis covers the design and implementation of several sub-units which used in microfluidic devices. These units are designed for a droplet-based multidrug analysis system which aims to reveal the efficacy of cancer chemotherapy for personalized treatments by using numerical models, and eventually, the designs are fabricated and validated by experimental studies. In this chapter, the main findings of the research will be summarized, and the possible future directions will be briefly discussed.

Accomplished tasks during the research regarding the microchannel network are summarized as follows:

- To achieve an almost homogenous drug-cell medium composition, a contraction-expansion type passive micromixer with series of throttles, which couples Dean vortices arising by the presence of the centrifugal forces and expansion vortices which are induced by flow separation to increase the extent of mixing at the microscale, is presented.
- Mixing performance of the micromixer was evaluated both numerically and experimentally by defining a figure of merit which depends on the standard deviation of species concentration at both the inlet and the outlet.
- Evaluating both the experimental results and numerical simulations indicates that reasonably good mixing with an efficiency over 80% can be achieved for a wide range of Reynolds numbers by increasing the number of throttles.
- A conventional flow-focusing junction for droplet generation is presented to ensure the formation of isolated tiny compartments where drug-cell interaction can be observed at the single-cell level.

- Numerical simulations demonstrate that almost spherical droplets which contain sufficient amount of medium content to support cell cultivation at a high generation rate (>1000 kHz) can be obtained for several flow rate couples of dispersed and continuous phases.
- The size distribution of droplets with respect to flow rates of immiscible phases is experimentally obtained and the experimental studies corroborate that droplets with an effective size around 50 μm can be generated by altering the flow rates of both phases.
- In the experiments using the fluorosurfactant, it is observed that droplets retain their shapes for up to 12 hours in PDMS channels.
- A significant hindrance in droplet-based single-cell studies is that the encapsulation of the cells is dictated by stochastic cell loading. This limitation can be circumvented by hydrodynamic focusing of cells before generating the drops at the junction. Here, hydrodynamic self-ordering in a microchannel incorporating proposed passive micromixer structure is realized numerically by particle tracing simulations where the total lift force obtained by DNS studies is manually interpolated. Here, hydrodynamic self-ordering in a microchannel incorporating proposed passive micromixer structure is numerically realized by particle tracing simulations where the total lift force obtained by DNS studies is manually interpolated.
- Additionally, it is experimentally validated that the micromixer enhances the single-cell encapsulation ratio to a certain degree (up to %42) by hydrodynamically focusing the cells to the middle of the microchannel.
- After completing the design and experimental validation of the sub-units of microchannel network, in order to prove the concept of droplet-based drug effect analysis system, the cytotoxicity effect of the drug on the individual K-562 leukemia cells confined in droplets is investigated. For this purpose, the effectivity of the anti-cancer drug, doxorubicin, on K-562 leukemia cancer cells is measured at the single-cell level based on the fluorescence intensity

change over 2 hours and compared with a control group which is not exposed to the drug. For future studies, the limitation regarding the duration of viability monitoring due to droplet shrinkage problem in PDMS channels will be overcome.

Besides developing the microchannel network for full droplet screening workflow, accomplished tasks regarding the electrostatically actuated microvalves are summarized as follows:

- By employing analytical models and numerical simulations, the complete design of a normally closed type electrostatically actuated microvalve is proposed. The valve operates by applying DC voltage across the top and bottom electrodes located at the bottom of the actuation chamber and at the top of the diaphragm. When the diaphragm is pulled towards the bottom electrode, it allows fluid flow underneath the valve seat suspending from top of the microchannel.
- The fabrication process flow is explained, and the performance of the fabricated microvalves is investigated in terms of several figures of merits including pull-in and pull-out voltages, response times, repeatability and touch area with respect to applied voltage.
- Pull-in voltage is measured around 122 ± 10.65 V with 300 μm diaphragm radius. The experimentally obtained value of pull-in voltage is closely consistent with numerical and analytical studies.
- Response times for both opening and closing states observed between 1-3 seconds for different valves.
- The diaphragms are actuated at 150 V and repeatedly cycled on/off more than 50 times without no problems.
- Moreover, fabricated moving diaphragms which are sealed with PDMS microchannels are tested under flow to prove that the proposed channel

integration allows fluid flow underneath the valve seat when the valve is actuated.

All of these sub-units are generic parts which can be utilized in several LOC systems. Micromixers are critical components of many microfluidic reactors, particularly for chemical and biological applications which demand fast interaction of reagent molecules, including the study of reaction kinetics, chemical synthesis, sample preparation for biological analysis and so on [150]. Apart from enabling analysis at the single-cell level, microdroplet technology offers many distinctive features for various application fields due mainly to monodisperse and high-throughput compartmentalization. One current trend of continuous-flow droplet microfluidics is to develop integrated and automated LOC devices to perform polymerase chain reaction (PCR) on-chip for amplification of DNA sequences for functional analysis of genes [151]. In addition, droplet-based spheroids are appealing for studying 3D cell culture which is a sophisticated in vitro environment for studying drug discovery, the mechanism of diseases, and tissue engineering and even promise organ biofabrication [152]. Moreover, inertial microfluidics is a mainstream technology where hydrodynamic forces can even be used as a size-based cell separation for circulating tumor cell (CTC) isolation and blood filtration [117]. Lastly, microvalves are crucial microfluidic elements delivering complex functionality where regulating the timing, defining the rate and location of the flow along microchannels is necessary. Thus, either unit can be included in a multitude of microfluidic platforms pointing out distinct applications.

As it is previously mentioned, these microfluidic units are designed for a droplet-based multidrug analysis system which is proposed in Chapter 1 and aims to reveal the efficacy of cancer chemotherapy for personalized treatments. Thus, the ultimate future goal is to achieve the integration of designed microchannel network with the electrostatically actuated microvalves. In order to actualize the concept of integrated multidrug effect analysis LOC platform, the relevant mask layouts are drawn (Figure 8.1 (a)), and fabrication of initial prototypes are completed by following the same

microfabrication steps used for valve characterization devices. The electrostatically driven diaphragms are fabricated by conventional MEMS technology on a glass wafer (Figure 8.1 (b)). Then, PDMS soft-lithography is applied for microchannel fabrication after fabricating the silicon mold by photolithography with AZ® 40 XT (Figure 8.1 (c)). Both substrates are sealed with oxygen plasma treatment at die level to achieve a complete platform (Figure 8.1 (d)).

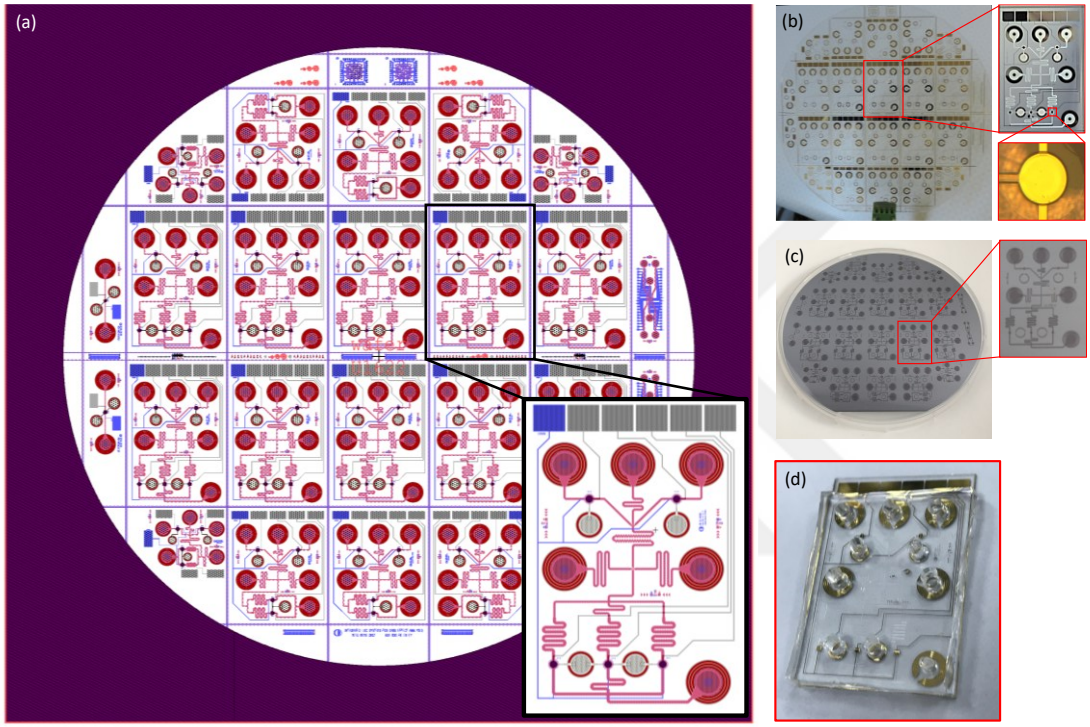

Figure 8.1. (a) Complete mask layout for multidrug effect analysis platform. (b) Micromachined glass wafer which comprises electrostatically actuated moving diaphragms. (c) Silicon-based mold wafer to perform PDMS soft-lithography for microchannel network fabrication. (d) The complete multidrug analysis LOC device after plasma-assisted PDMS/glass bonding.

The complete LOC platform is at the testing stage for in vitro cytotoxicity screening. Experimental validation will be completed after enhancing the current test setup by designing a microfluidic holder for an easy-to-use electric and fluidic interface and a pressure chamber to be able to drive several inlets simultaneously with a single source. After validating the proper functioning of the complete system, the multidrug effect analysis platform can be integrated with enrichment platforms rendering circulating tumor cell (CTC) separation; thus, it will be possible to quickly diagnose and present

potential cancer treatments on the same chip simultaneously. Moreover, an interesting application of the complete system could be the evaluation of the efficiency of potential antimicrobial therapies after providing fast infection of cells with multiple bacteria or virus gradients.

An important prospective challenge is to enable the platform to perform autonomous discovery itself in order to provide non-experts with easy use. Here, electrical impedance measurements can be utilized to detect viable cells confined in droplets [153]; however, electrical sensing is not feasible for the proposed analysis system. Since the droplets are stationary during the viability screening, the exact locations of droplets should be predefined, and the number of sensing electrode pairs should be equal to the number of drops. Here, the integration of on-chip imaging techniques based on CMOS image sensors with the microfluidic chip platform could provide a lens-free fully automated system from sample handling to high-throughput screening and the analyzing of drug-cell interaction.

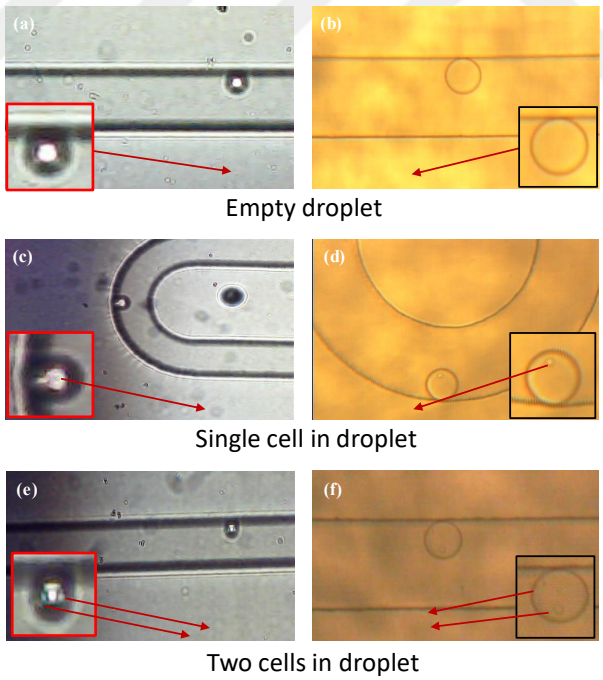

Figure 8.2. Bright light images of the generated drops. (a) CMOS and (b) microscope image of an empty droplet, (c) CMOS and (d) microscope image of a drop containing a single cell, (e) CMOS and (f) microscope image of a droplet containing two cells [154].

An initial proof-of-concept is presented where the cells confined in drops are monitored in the bright field by integrating a commercial CMOS image sensor to a PDMS-based microfluidic droplet generator [154]. The images acquired through the image sensor are streamed and processed via an Android-based application on smartphone and compared with the microscopic images (Figure 8.2). In addition, a thin-film absorption filter deposited on the CMOS sensor can be utilized for fluorescence imaging [155]. Thus, an integrated chip-scale CMOS imager can be considered as a potential solution to achieve fully automated viability screening of cancer cells in chemosensitivity assays which can be employed to decide an effective personalized cancer therapy after completing the post-processing and analysis of obtained images.

REFERENCES

[1] P. S. Dittrich and A. Manz, “Lab-on-a-chip: Microfluidics in drug discovery,” *Nat. Rev. Drug Discov.*, vol. 5, no. 3, pp. 210–218, 2006.

[2] D. Di Carlo, L. Y. Wu, and L. P. Lee, “Dynamic single cell culture array,” *Lab Chip*, vol. 6, no. 11, pp. 1445–1449, 2006.

[3] Z. Long *et al.*, “Microfluidic chemostat for measuring single cell dynamics in bacteria,” *Lab Chip*, vol. 13, no. 5, pp. 947–954, 2013.

[4] L. Lin, Y.-S. Chu, J. P. Thiery, C. T. Lim, and I. Rodriguez, “Microfluidic cell trap array for controlled positioning of single cells on adhesive micropatterns,” *Lab Chip*, vol. 13, no. 4, p. 714, 2013.

[5] R. D. Sochol, M. E. Dueck, S. Li, L. P. Lee, and L. Lin, “Hydrodynamic resettability for a microfluidic particulate-based arraying system,” *Lab Chip*, vol. 12, no. 23, pp. 5051–5056, 2012.

[6] Y. Wang *et al.*, “A microfluidic digital single-cell assay for the evaluation of anticancer drugs,” *Anal. Bioanal. Chem.*, vol. 407, no. 4, pp. 1139–1148, 2015.

[7] R. S. Thomas, H. Morgan, and N. G. Green, “Negative DEP traps for single cell immobilisation,” *Lab Chip*, vol. 9, no. 11, pp. 1534–1540, 2009.

[8] J. Voldman, M. L. Gray, M. Toner, and M. A. Schmidt, “A microfabrication-based dynamic array cytometer,” *Anal. Chem.*, vol. 74, no. 16, pp. 3984–3990, 2002.

[9] D. S. Gray, J. L. Tan, J. Voldman, and C. S. Chen, “Dielectrophoretic registration of living cells to a microelectrode array,” *Biosens. Bioelectron.*, vol. 19, no. 7, pp. 771–780, 2004.

[10] M. Donolato *et al.*, “Magnetic domain wall conduits for single cell

applications," *Lab Chip*, vol. 11, no. 17, pp. 2976–2983, 2011.

[11] D. Nawarathna *et al.*, "Shrink-induced sorting using integrated nanoscale magnetic traps," *Appl. Phys. Lett.*, vol. 102, no. 6, pp. 1–5, 2013.

[12] H. C. Lai, C. H. Wang, T. M. Liou, and G. Bin Lee, "Influenza A virus-specific aptamers screened by using an integrated microfluidic system," *Lab Chip*, vol. 14, no. 12, pp. 2002–2013, 2014.

[13] A. Chen *et al.*, "On-chip magnetic separation and encapsulation of cells in droplets," *Lab Chip*, vol. 13, no. 6, p. 1172, 2013.

[14] F. Guo *et al.*, "Three-dimensional manipulation of single cells using surface acoustic waves," *Proc. Natl. Acad. Sci.*, vol. 113, no. 6, pp. 1522–1527, 2016.

[15] C. Liberale *et al.*, "Integrated microfluidic device for single-cell trapping and spectroscopy," *Sci. Rep.*, vol. 3, 2013.

[16] A. Ashkin, J. M. Dziedzic, and T. Yamane, "Optical trapping and manipulation of single cells using infrared laser beams," *Nature*, vol. 330, no. 6150, pp. 769–771, Dec. 1987.

[17] X. Wang *et al.*, "Enhanced cell sorting and manipulation with combined optical tweezer and microfluidic chip technologies," *Lab Chip*, vol. 11, no. 21, pp. 3656–3662, 2011.

[18] P. Y. Chiou, A. T. Ohta, and M. C. Wu, "Massively parallel manipulation of single cells and microparticles using optical images," *Nature*, vol. 436, no. 7049, pp. 370–372, 2005.

[19] Š. Selimović, F. Piraino, H. Bae, M. Rasponi, A. Redaelli, and A. Khademhosseini, "Microfabricated polyester conical microwells for cell culture applications," *Lab Chip*, vol. 11, no. 14, p. 2325, 2011.

[20] J. R. Rettig and A. Folch, "Large-Scale Single-Cell Trapping And Imaging Using Microwell Arrays," *Anal. Chem.*, vol. 77, no. 17, pp. 5628–5634, Sep.

2005.

[21] L. Li, Q. Wang, J. Feng, L. Tong, and B. Tang, “Highly sensitive and homogeneous detection of membrane protein on a single living cell by aptamer and nicking enzyme assisted signal amplification based on microfluidic droplets,” *Anal. Chem.*, vol. 86, no. 10, pp. 5101–5107, 2014.

[22] J. Clausell-Tormos *et al.*, “Droplet-Based Microfluidic Platforms for the Encapsulation and Screening of Mammalian Cells and Multicellular Organisms,” *Chem. Biol.*, vol. 15, no. 5, pp. 427–437, 2008.

[23] S. Köster *et al.*, “Drop-based microfluidic devices for encapsulation of single cells,” *Lab Chip*, vol. 8, no. 7, pp. 1110–1115, 2008.

[24] Z. Gong *et al.*, “Drug effects analysis on cells using a high throughput microfluidic chip,” *Biomed. Microdevices*, vol. 13, no. 1, pp. 215–219, 2011.

[25] J. J. Agresti *et al.*, “Ultrahigh-throughput screening in drop-based microfluidics for directed evolution,” *Proc. Natl. Acad. Sci.*, vol. 107, no. 9, pp. 4004–4009, 2010.

[26] E. J. Fox and L. A. Loeb, “One cell at a time,” *Nature*, vol. 512, no. 7513, pp. 143–144, 2014.

[27] “Advantages of personalized cancer therapy | DNA Research Center.” [Online]. Available: http://personalizedtherapy.eu/advantages. [Accessed: 21-Dec-2018].

[28] N. Nguyen and Z. Wu, “Micromixers — a review,” *J. Micromechanics Microengineering*, vol. 15, no. 2, 2004.

[29] A. Cosentino, H. Madadi, P. Vergara, R. Vecchione, F. Causa, and P. A. Netti, “An efficient planar accordion-shaped micromixer: From biochemical mixing to biological application,” *Sci. Rep.*, vol. 5, no. November, pp. 1–10, 2015.

[30] N.-T. Nguyen, “Fundamentals of mass transport in the microscale,” in

Micromixers, 2012, pp. 9–72.

[31] B. J. Kirby, *Micro- and Nanoscale Fluid Mechanics: Transport in Microfluidic Devices*. Cambridge, 2010.

[32] P.-H. Huang *et al.*, "An acoustofluidic micromixer based on oscillating sidewall sharp-edges," *Lab Chip*, vol. 13, no. 19, p. 3847, 2013.

[33] X. Ding *et al.*, "On-chip manipulation of single microparticles, cells, and organisms using surface acoustic waves," *Proc. Natl. Acad. Sci.*, vol. 109, no. 28, pp. 11105–11109, 2012.

[34] W. K. Tseng, J. L. Lin, W. C. Sung, S. H. Chen, and G. Bin Lee, "Active micro-mixers using surface acoustic waves on Y-cut 128° LiNbO3," *J. Micromechanics Microengineering*, vol. 16, no. 3, pp. 539–548, 2006.

[35] J. Shi, X. Mao, D. Ahmed, A. Colletti, and T. J. Huang, "Focusing microparticles in a microfluidic channel with standing surface acoustic waves (SSAW)," *Lab Chip*, vol. 8, no. 2, pp. 221–223, 2008.

[36] A. R. Rezk, A. Qi, J. R. Friend, W. H. Li, and L. Y. Yeo, "Uniform mixing in paper-based microfluidic systems using surface acoustic waves," *Lab Chip*, vol. 12, no. 4, pp. 773–779, 2012.

[37] K. S. Ryu, K. Shaikh, E. Goluch, Z. Fan, and C. Liu, "Micro magnetic stir-bar mixer integrated with parylene microfluidic channels," *Lab Chip*, vol. 4, no. 6, pp. 608–613, 2004.

[38] G. P. Zhu and N. T. Nguyen, "Rapid magnetofluidic mixing in a uniform magnetic field," *Lab Chip*, vol. 12, no. 22, pp. 4772–4780, 2012.

[39] F. Cheaib, G. Kekejian, S. Antoun, M. Cheikh, and I. Lakkis, "Microfluidic mixing using pulsating flows," *Microfluid. Nanofluidics*, vol. 20, no. 5, pp. 1–19, 2016.

[40] A. Afzal and K. Y. Kim, "Convergent-divergent micromixer coupled with

pulsatile flow," *Sensors Actuators, B Chem.*, vol. 211, pp. 198–205, 2015.

[41] M. Sigurdson, D. Wang, and C. D. Meinhart, "Electrothermal stirring for heterogeneous immunoassays," *Lab Chip*, vol. 5, no. 12, pp. 1366–1373, 2005.

[42] C. K. Harnett, J. Templeton, K. A. Dunphy-Guzman, Y. M. Senousy, and M. P. Kanouff, "Model based design of a microfluidic mixer driven by induced charge electroosmosis," *Lab Chip*, vol. 8, no. 4, pp. 565–572, 2008.

[43] C. Y. Lee, G. Bin Lee, L. M. Fu, K. H. Lee, and R. J. Yang, "Electrokinetically driven active micro-mixers utilizing zeta potential variation induced by field effect," *J. Micromechanics Microengineering*, vol. 14, no. 10, pp. 1390–1398, 2004.

[44] R. J. Yang, C. H. Wu, T. I. Tseng, S. B. Huang, and G. B. Lee, "Enhancement of electrokinetically-driven flow mixing in microchannel with added side channels," *Japanese J. Appl. Physics, Part 1 Regul. Pap. Short Notes Rev. Pap.*, vol. 44, no. 10, pp. 7634–7642, 2005.

[45] J. T. Coleman, J. McKechnie, and D. Sinton, "High-efficiency electrokinetic micromixing through symmetric sequential injection and expansion," *Lab Chip*, vol. 6, no. 8, pp. 1033–1039, 2006.

[46] W. Y. Ng, S. Goh, Y. C. Lam, C. Yang, and I. Rodríguez, "DC-biased AC-electroosmotic and AC-electrothermal flow mixing in microchannels," *Lab Chip*, vol. 9, no. 6, pp. 802–809, 2009.

[47] J. H. Tsai and L. Lin, "Active microfluidic mixer and gas bubble filter driven by thermal bubble micropump," *Sensors Actuators, A Phys.*, vol. 97–98, pp. 665–671, 2002.

[48] A. N. Hellman *et al.*, "Laser-induced mixing in microfluidic channels," *Anal. Chem.*, vol. 79, no. 12, pp. 4484–4492, 2007.

[49] S. C. S. Lin, X. Mao, and T. J. Huang, "Surface acoustic wave (SAW)

acoustophoresis: Now and beyond," *Lab Chip*, vol. 12, no. 16, pp. 2766–2770, 2012.

[50] M. S. Munson and P. Yager, "Simple quantitative optical method for monitoring the extent of mixing applied to a novel microfluidic mixer," *Anal. Chim. Acta*, vol. 507, no. 1, pp. 63–71, 2004.

[51] Seok Woo Lee, Dong Sung Kim, S. S. Lee, and Tai Hun Kwon, "Split and recombination micromixer based on PDMS three-dimensional micro structure," *J. Micromechanics Microengineering*, vol. 16, no. 5, pp. 1067–1072, 2006.

[52] J. Cha *et al.*, "A highly efficient 3D micromixer using soft PDMS bonding," *J. Micromechanics Microengineering*, vol. 16, no. 9, pp. 1778–1782, 2006.

[53] J. Clark, M. Kaufman, and P. S. Fodor, "Mixing enhancement in serpentine micromixers with a non-rectangular cross-section," *Micromachines*, vol. 9, no. 3, 2018.

[54] H. Le The, B. Q. Ta, H. Le Thanh, T. Dong, T. N. Thoi, and F. Karlsen, "Geometric effects on mixing performance in a novel passive micromixer with trapezoidal-zigzag channels," *J. Micromechanics Microengineering*, vol. 25, no. 9, 2015.

[55] S. Jain and H. N. Unni, "Design and Simulation of Microfluidic Passive Mixer With Geometric Variation," *Int. J. Res. Eng. Technol.*, no. i, pp. 2319–2322, 2016.

[56] M. G. Lee, S. Choi, and J. Park, "Rapid laminating mixer using a contraction-expansion array microchannel," *Appl. Phys. Lett.*, vol. 95, no. 5, p. 051902, 2009.

[57] M. G. Lee, S. Choi, and J. Park, "Rapid multivortex mixing in an alternately formed contraction-expansion array microchannel," *Biomed. Microdevices*, vol. 12, no. 6, pp. 1019–1026, 2010.

[58] A. Stroock, Abraham D. Dertinger, Stephan K.W. Ajdari, I. Mezic, H. A. Stone, and G. M. Whitesides, “Chaotic_mixer_for_microchannel.PDF,” vol. 295, no. January, pp. 647–652, 2002.

[59] E. Yıldırım, “Analysis and testing of a contraction - and - expansion micromixer for micromilled microfluidics,” *Microsyst. Technol.*, vol. 23, no. 10, pp. 4797–4804, 2017.

[60] “Microfluidics Module User’s Guide, version 5.3a,” *COMSOL, Inc*, 2017.

[61] N. Nivedita, P. Ligrani, and I. Papautsky, “Dean Flow Dynamics in Low-Aspect Ratio Spiral Microchannels,” *Sci. Rep.*, vol. 7, no. 1, pp. 1–10, 2017.

[62] J. B. Wacker, I. Lignos, V. K. Parashar, and M. A. M. Gijs, “Controlled synthesis of fluorescent silica nanoparticles inside microfluidic droplets,” *Lab Chip*, vol. 12, no. 17, pp. 3111–3116, 2012.

[63] L. L. Lazarus, C. T. Riche, B. C. Marin, M. Gupta, N. Malmstadt, and R. L. Brutchey, “Two-phase microfluidic droplet flows of ionic liquids for the synthesis of gold and silver nanoparticles,” *ACS Appl. Mater. Interfaces*, vol. 4, no. 6, pp. 3077–3083, 2012.

[64] M. Chau *et al.*, “Microfluidic generation of composite biopolymer microgels with tunable compositions and mechanical properties,” *Biomacromolecules*, vol. 15, no. 7, pp. 2419–2425, 2014.

[65] W. H. Tan and S. Takeuchi, “Monodisperse alginate hydrogel microbeads for cell encapsulation,” *Adv. Mater.*, vol. 19, no. 18, pp. 2696–2701, 2007.

[66] H. N. Joensson *et al.*, “Detection and analysis of low-abundance cell-surface biomarkers using enzymatic amplification in microfluidic droplets,” *Angew. Chemie - Int. Ed.*, vol. 48, no. 14, pp. 2518–2521, 2009.

[67] P. Kumaresan, C. J. Yang, S. A. Cronier, R. G. Blazej, and R. A. Mathies, “High-throughput single copy DNA amplification and cell analysis in

engineered nanoliter droplets," *Anal. Chem.*, vol. 80, no. 10, pp. 3522–3529, 2008.

[68] F. Eduati *et al.*, "A microfluidics platform for combinatorial drug screening on cancer biopsies," *Nat. Commun.*, vol. 9, no. 1, 2018.

[69] A. Kulesa, J. Kehe, J. E. Hurtado, P. Tawde, and P. C. Blainey, "Combinatorial drug discovery in nanoliter droplets," *Proc. Natl. Acad. Sci.*, vol. 115, no. 26, pp. 6685–6690, 2018.

[70] S. Abraham *et al.*, "Microfluidics assisted synthesis of well-defined spherical polymeric microcapsules and their utilization as potential encapsulants," *Lab Chip*, vol. 6, no. 6, pp. 752–756, 2006.

[71] V. Srinivasan, V. K. Pamula, and R. B. Fair, "An integrated digital microfluidic lab-on-a-chip for clinical diagnostics on human physiological fluids," *Lab Chip*, vol. 4, no. 4, pp. 310–315, 2004.

[72] H. Song, H. W. Li, M. S. Munson, T. G. V. Ha, and R. F. Ismagilov, "On-chip titration of an anticoagulant argatroban and determination of the clotting time within whole blood or plasma using a plug-based microfluidic system," *Anal. Chem.*, vol. 78, no. 14, pp. 4839–4849, 2006.

[73] S. Jakiela, T. S. Kaminski, O. Cybulski, D. B. Weibel, and P. Garstecki, "Bacterial growth and adaptation in microdroplet chemostats," *Angew. Chemie - Int. Ed.*, vol. 52, no. 34, pp. 8908–8911, 2013.

[74] S. Neethirajan, I. Kobayashi, M. Nakajima, D. Wu, S. Nandagopal, and F. Lin, "Microfluidics for food, agriculture and biosystems industries," *Lab Chip*, vol. 11, no. 9, pp. 1574–1586, 2011.

[75] P. Zhu and L. Wang, "Passive and active droplet generation with microfluidics: a review," *Lab Chip*, vol. 17, no. 1, pp. 34–75, 2017.

[76] T. Thorsen, R. W. Roberts, F. H. Arnold, and S. R. Quake, "Dynamic pattern

formation in a vesicle-generating microfluidic device," *Phys. Rev. Lett.*, vol. 86, no. 18, pp. 4163–4166, 2001.

[77] P. B. Umbanhowar, V. Prasad, and D. A. Weitz, "Monodisperse emulsion generation via drop break off in a coflowing stream," *Langmuir*, vol. 16, no. 2, pp. 347–351, 2000.

[78] S. L. Anna, N. Bontoux, and H. A. Stone, "Formation of dispersions using 'flow focusing' in microchannels," *Appl. Phys. Lett.*, vol. 82, no. 3, pp. 364–366, 2003.

[79] H. Gu, M. H. G. Duits, and F. Mugele, "Droplets formation and merging in two-phase flow microfluidics," *Int. J. Mol. Sci.*, vol. 12, no. 4, pp. 2572–2597, 2011.

[80] S. Y. Teh, R. Lin, L. H. Hung, and A. P. Lee, "Droplet microfluidics," *Lab Chip*, vol. 8, no. 2, pp. 198–220, 2008.

[81] P. Garstecki, M. J. Fuerstman, H. A. Stone, and G. M. Whitesides, "Formation of droplets and bubbles in a microfluidic T-junction - Scaling and mechanism of break-up," *Lab Chip*, vol. 6, no. 3, pp. 437–446, 2006.

[82] A. S. Utada, A. Fernandez-Nieves, H. A. Stone, and D. A. Weitz, "Dripping to jetting transitions in coflowing liquid streams," *Phys. Rev. Lett.*, vol. 99, no. 9, pp. 1–4, 2007.

[83] S. L. Anna and H. C. Mayer, "Microscale tipstreaming in a microfluidic flow focusing device," *Phys. Fluids*, vol. 18, no. 12, 2006.

[84] P. Zhu, T. Kong, Z. Kang, X. Tian, and L. Wang, "Tip-multi-breaking in capillary microfluidic devices," *Sci. Rep.*, vol. 5, pp. 1–8, 2015.

[85] P. Day, A. Manz, and Y. Zhang, *Microdroplet technology: Principles and emerging applications in biology and chemistry*. 2012.

[86] H. Ganapathy, E. Al-Hajri, and M. M. Ohadi, "Phase Field Method for

Simulation of Multiphase Flow," *Vol. 6 Fluids Therm. Syst. Adv. Process Ind. Parts A B*, no. January, pp. 1309–1319, 2011.

[87] F. Bai, X. He, X. Yang, R. Zhou, and C. Wang, "Three dimensional phase-field investigation of droplet formation in microfluidic flow focusing devices with experimental validation," *Int. J. Multiph. Flow*, vol. 93, pp. 130–141, 2017.

[88] M. Nekouei and S. A. Vanapalli, "Volume-of-fluid simulations in microfluidic T-junction devices: Influence of viscosity ratio on droplet size," *Phys. Fluids*, vol. 29, no. 3, 2017.

[89] M. M. Lamine Diouf and O. J. Romero, "Numerical study of droplet formation in a Y-junction microchannel," *J. Theor. Appl. Mech.*, no. 2006, p. 317, 2017.

[90] V. L. Wong, K. Loizou, P. L. Lau, R. S. Graham, and B. N. Hewakandamby, "Numerical studies of shear-thinning droplet formation in a microfluidic T-junction using two-phase level-SET method," *Chem. Eng. Sci.*, vol. 174, pp. 157–173, 2017.

[91] W. Lan, S. Li, Y. Wang, and G. Luo, "CFD simulation of droplet formation in microchannels by a modified level set method," *Ind. Eng. Chem. Res.*, vol. 53, no. 12, pp. 4913–4921, 2014.

[92] J. Liu and N. Trung Nguyen, "Numerical Simulation of Droplet-Based Microfluidics - A Review," *Micro Nanosyst.*, vol. 2, no. 3, pp. 193–201, 2010.

[93] B. S. Mirjalili, S. S. Jain, and M. S. Dodd, "Interface-capturing methods for two-phase flows : An overview and recent developments," *Annu. Res. Briefs*, no. 1, pp. 117–135, 2017.

[94] J. W. H. Cahn John E., J. W. Cahn, and J. E. Hilliard, "Free Energy of a Nonuniform System. I. Interfacial Free Energy," *J. Chem. Phys.*, vol. 28, no. 1958, pp. 258–267, 1958.

[95] P. Yue, J. J. Feng, C. Liu, and J. Shen, "A diffuse-interface method for

simulating two-phase flows of complex fluids," *J. Fluid Mech.*, vol. 515, pp. 293–317, 2004.

[96] S. Engblom, M. Do-Quang, G. Amberg, and A. K. Tornberg, "On diffuse interface modeling and simulation of surfactants in two-phase fluid flow," *Commun. Comput. Phys.*, vol. 14, no. 4, pp. 879–915, 2013.

[97] P. Yue and J. J. Feng, "Wall energy relaxation in the Cahn-Hilliard model for moving contact lines," *Phys. Fluids*, vol. 23, no. 1, pp. 1–8, 2011.

[98] J. Kim, "A continuous surface tension force formulation for diffuse-interface models," *J. Comput. Phys.*, vol. 204, no. 2, pp. 784–804, 2005.

[99] G. N. Wells, E. Kuhl, and K. Garikipati, "A discontinuous Galerkin method for the Cahn-Hilliard equation," *J. Comput. Phys.*, vol. 218, no. 2, pp. 860–877, 2006.

[100] H. Bruus, "Theoretical Microfluidics. 2008," *New York Oxford Univ. Press*, 2008.

[101] K. W. Oh, K. Lee, B. Ahn, and E. P. Furlani, "Design of pressure-driven microfluidic networks using electric circuit analogy," *Lab Chip*, vol. 12, no. 3, pp. 515–545, 2012.

[102] M. Rhee *et al.*, "Pressure stabilizer for reproducible picoinjection in droplet microfluidic systems," *Lab Chip*, vol. 14, no. 23, pp. 4533–4539, 2014.

[103] H. Ding and P. D. M. Spelt, "Wetting condition in diffuse interface simulations of contact line motion," *Phys. Rev. E - Stat. Nonlinear, Soft Matter Phys.*, vol. 75, no. 4, pp. 1–8, 2007.

[104] P. Yue, C. Zhou, and J. J. Feng, "Sharp-interface limit of the Cahn-Hilliard model for moving contact lines," *J. Fluid Mech.*, vol. 645, pp. 279–294, 2010.

[105] "Two-Phase Flow Modeling Guidelines - 1239 - Knowledge Base." [Online]. Available: https://www.comsol.com/support/knowledgebase/1239/?setlang=1.

[Accessed: 08-Dec-2018].

[106] P. K. Periyannan Rajeswari, H. N. Joensson, and H. Andersson-Svahn, “Droplet size influences division of mammalian cell factories in droplet microfluidic cultivation,” *Electrophoresis*, vol. 38, no. 2, pp. 305–310, 2017.

[107] K. Ahn, C. Kerbage, T. P. Hunt, R. M. Westervelt, D. R. Link, and D. A. Weitz, “Dielectrophoretic manipulation of drops for high-speed microfluidic sorting devices,” *Appl. Phys. Lett.*, vol. 88, no. 2, pp. 1–3, 2006.

[108] J. C. Baret *et al.*, “Fluorescence-activated droplet sorting (FADS): Efficient microfluidic cell sorting based on enzymatic activity,” *Lab Chip*, vol. 9, no. 13, pp. 1850–1858, 2009.

[109] J. Nam, H. Lim, C. Kim, J. Yoon Kang, and S. Shin, “Density-dependent separation of encapsulated cells in a microfluidic channel by using a standing surface acoustic wave,” *Biomicrofluidics*, vol. 6, no. 2, pp. 1–10, 2012.

[110] Q. Zhang, T. T. Wang, M. L. Yang, and B. Ma, “A Droplet Sorting Based Single-Cell Isolation and Dispensing Platform With a Chip-To-World Interface,” pp. 796–798, 2014.

[111] T. Jing, R. Ramji, M. E. Warkiani, J. Han, C. T. Lim, and C. H. Chen, “Jetting microfluidics with size-sorting capability for single-cell protease detection,” *Biosens. Bioelectron.*, vol. 66, pp. 19–23, 2015.

[112] M. Chabert and J.-L. Viovy, “Microfluidic high-throughput encapsulation and hydrodynamic self-sorting of single cells,” *Proc. Natl. Acad. Sci.*, vol. 105, no. 9, pp. 3191–3196, Mar. 2008.

[113] D. J. Collins, A. Neild, A. deMello, A. Q. Liu, and Y. Ai, “The Poisson distribution and beyond: Methods for microfluidic droplet production and single cell encapsulation,” *Lab Chip*, vol. 15, no. 17, pp. 3439–3459, 2015.

[114] A. R. Abate, C. H. Chen, J. J. Agresti, and D. A. Weitz, “Beating Poisson

encapsulation statistics using close-packed ordering," *Lab Chip*, vol. 9, no. 18, pp. 2628–2631, 2009.

[115] E. W. M. Kemna, R. M. Schoeman, F. Wolbers, I. Vermes, D. A. Weitz, and A. Van Den Berg, "High-yield cell ordering and deterministic cell-in-droplet encapsulation using Dean flow in a curved microchannel," *Lab Chip*, vol. 12, no. 16, pp. 2881–2887, 2012.

[116] J. Zhang *et al.*, "Fundamentals and applications of inertial microfluidics: A review," *Lab Chip*, vol. 16, no. 1, pp. 10–34, 2016.

[117] J. M. Martel and M. Toner, "Inertial Focusing in Microfluidics," *Annu. Rev. Biomed. Eng.*, vol. 16, no. 1, pp. 371–396, 2014.

[118] J. P. Matas, J. F. Morris, and E. Guazzelli, "Lateral Forces on a Sphere," *Oil Gas Sci. Technol. IFP*, vol. 59, no. 1, pp. 59–70, 2004.

[119] P. G. Saffman, "The lift on a small sphere in a slow shear flow," *J. Fluid Mech.*, vol. 22, no. 02, p. 385, Jun. 1965.

[120] L. Zeng, F. Najjar, S. Balachandar, and P. Fischer, "Forces on a finite-sized particle located close to a wall in a linear shear flow," *Phys. Fluids*, vol. 21, no. 3, 2009.

[121] D. Di Carlo, J. F. Edd, K. J. Humphry, H. A. Stone, and M. Toner, "Particle segregation and dynamics in confined flows," *Phys. Rev. Lett.*, vol. 102, no. 9, 2009.

[122] B. P. Ho and L. G. Leal, "Migration of rigid spheres in a two-dimensional unidirectional shear flow of a second-order fluid," *J. Fluid Mech.*, vol. 76, no. 4, pp. 783–799, 1976.

[123] G. Segré and A. Silberberg, "Behaviour of macroscopic rigid spheres in Poiseuille flow Part 2. Experimental results and interpretation," *J. Fluid Mech.*, vol. 14, no. 01, p. 136, Sep. 1962.

[124] J. Zhou and I. Papautsky, “Fundamentals of inertial focusing in microchannels,” *Lab Chip*, vol. 13, no. 6, pp. 1121–1132, 2013.

[125] A. Mechanics *et al.*, “Migration of a sphere in tube flow,” *J. Fluid Mech.*, vol. 540, no. 1, p. 109, 2005.

[126] C. Liu, C. Xue, J. Sun, and G. Hu, “A generalized formula for inertial lift on a sphere in microchannels,” *Lab Chip*, vol. 16, no. 5, pp. 884–892, 2016.

[127] D. Di Carlo, “Inertial microfluidics,” *Lab Chip*, vol. 9, no. 21, pp. 3038–3046, 2009.

[128] J. M. Martel and M. Toner, “Particle focusing in curved microfluidic channels,” *Sci. Rep.*, vol. 3, pp. 1–8, 2013.

[129] E. S. Asmolov, “The inertial lift on a spherical particle in a plane Poiseuille flow at large channel Reynolds number,” *J. Fluid Mech.*, vol. 381, p. S0022112098003474, Feb. 1999.

[130] K. ichi Sugioka and T. Tsukada, “Direct numerical simulations of drag and lift forces acting on a spherical bubble near a plane wall,” *Int. J. Multiph. Flow*, vol. 71, pp. 32–37, 2015.

[131] H. Söderqvist, “Modeling and simulation of particle dynamics in microfluidic channels,” 2017.

[132] M. H. Madsen, N. A. Feidenhans’l, P. E. Hansen, J. Garnæs, and K. Dirscherl, “Accounting for PDMS shrinkage when replicating structures,” *J. Micromechanics Microengineering*, vol. 24, no. 12, 2014.

[133] J. C. Baret, “Surfactants in droplet-based microfluidics,” *Lab Chip*, vol. 12, no. 3, pp. 422–433, 2012.

[134] M. Hashimoto, P. Garstecki, H. A. Stone, and G. M. Whitesides, “Interfacial instabilities in a microfluidic Hele-Shaw cell,” *Soft Matter*, vol. 4, no. 7, pp. 1403–1413, 2008.

[135] O. Wagner *et al.*, “Biocompatible fluorinated polyglycerols for droplet microfluidics as an alternative to PEG-based copolymer surfactants,” *Lab Chip*, vol. 16, no. 1, pp. 65–69, 2016.

[136] E. Brouzes *et al.*, “Droplet microfluidic technology for single-cell high-throughput screening,” *Proc. Natl. Acad. Sci.*, vol. 106, no. 34, pp. 14195–14200, Aug. 2009.

[137] B. R. Knudsen *et al.*, “Synthesis of Fluorosurfactants for Emulsion-Based Biological Applications,” *ACS Nano*, no. 4, pp. 3913–3920, 2014.

[138] L. Mazutis, J. Gilbert, W. L. Ung, D. A. Weitz, A. D. Griffiths, and J. A. Heyman, “Single-cell analysis and sorting using droplet-based microfluidics,” *Nat. Protoc.*, vol. 8, no. 5, pp. 870–891, 2013.

[139] M. Rosenberg, N. F. Azevedo, and A. Ivask, “Propidium iodide staining underestimates viability of adherent bacterial cells,” pp. 1–14, 2018.

[140] K. W. Oh and C. H. Ahn, “A review of microvalves,” *J. Micromechanics Microengineering*, vol. 16, no. 5, 2006.

[141] Y. Song, D. Cheng, and L. Zhao, *Microfluidics: Fundamental, Devices and Applications*, vol. 32, no. 3. Weinheim, Germany: Wiley-VCH Verlag GmbH & Co. KGaA, 2018.

[142] M. A. Unger, M. A. Unger, H. Chou, T. Thorsen, A. Scherer, and S. R. Quake, “Monolithic Microfabricated Valves and Pumps by Multilayer Soft Lithography,” *Science*, vol. 113, no. 2000, pp. 113–116, 2013.

[143] Dan E. Angelescu, *Highly Integrated Microfluidics Design (Integrated Microsystems)*. Artech House, 2011.

[144] T. L. Sounart, T. A. Michalske, and K. R. Zavadil, “Frequency-dependent electrostatic actuation in microfluidic MEMS,” *J. Microelectromechanical Syst.*, vol. 14, no. 1, pp. 125–133, 2005.

[145] M. P. Chang and M. M. Maharbiz, “Electrostatically-driven elastomer components for high density microfluidics,” *Lab Chip*, vol. 9, no. 9, 2009.

[146] C. R. Neagu, J. G. E. Gardeniers, M. Elwenspoek, and J. J. Kelly, “An electrochemical active valve,” *Electrochim. Acta*, vol. 42, no. 20–22, 1997.

[147] N.-T. Nguyen and S. T. Wereley, *Fundamentals And Applications of Microfluidics*, Second Edi. Artech Print, 2006.

[148] E. Yildirim, M. A. S. Arikan, and H. Külah, “A normally closed electrostatic parylene microvalve for micro total analysis systems,” *Sensors Actuators, A Phys.*, vol. 181, pp. 81–86, 2012.

[149] F. Yu, J. C. H. Lin, P. J. Chen, and Y. C. Tai, “Parylene stiction,” *Proc. IEEE Int. Conf. Micro Electro Mech. Syst.*, vol. 2, pp. 408–411, 2010.

[150] B. Lin, *Microfluidics Technologies: Technologies and Applications*, vol. 304. Heidelberg: Springer, 2011.

[151] Y. Zhang and H. R. Jiang, “A review on continuous-flow microfluidic PCR in droplets: Advances, challenges and future,” *Anal. Chim. Acta*, vol. 914, 2016.

[152] R. K. Vadivelu, H. Kamble, M. J. A. Shiddiky, and N. T. Nguyen, “Microfluidic technology for the generation of cell spheroids and their applications,” *Micromachines*, vol. 8, no. 4, pp. 1–23, 2017.

[153] E. W. M. Kemna, L. I. Segerink, F. Wolbers, I. Vermes, and A. Van Den Berg, “Label-free, high-throughput, electrical detection of cells in droplets,” *Analyst*, vol. 138, no. 16, pp. 4585–4592, 2013.

[154] M. D. Özkan, M. K. Aslan, A. C. Atik, E. Özgür, E. Yıldırım, and H. Külah, “Droplet Based Cell Screening System Integrated with CMOS Image Sensor and Android-Based Application,” in *MicroTAS*, 2017.

[155] H. Takehara *et al.*, “On-chip cell analysis platform: Implementation of contact fluorescence microscopy in microfluidic chips,” *AIP Adv.*, vol. 7, no. 9, 2017.

APPENDICES

A. Process Flow

Table A.1. *Detailed fabrication flow of normally-closed electrostatically actuated microvalves.*

Step	Process		Comment
MEMS Fabrication of Electrostatically-Driven Diaphragms on Glass			
1	**Substrate – Glass**	Size: 150mm (6“) Thickness: 525µm +/- 25µm	
2	**Cr/Au Metal Sputtering**	1. Dehydration at 110 °C for 20 min. 2. Cr sputtering (Bestec) at 300 W (Thickness: 30 nm). 3. Au sputtering (Bestec) at 300 W (Thickness: 300 nm).	Metal deposition as a masking layer during wet glass etching.
3	**Photolithography** Mask: Actuation Chambers and Air Vents	1. Dehydration at 110 °C for 20 min. 2. Spin coat HMDS at 1000 rpm for 7 sec, and at 3000 rpm for 30 sec. 3. Spin coat AZ 5124 at 1000 rpm for 7 sec, and at 3000 rpm for 30 sec. 4. Soft bake at 110 °C for 120 sec. 5. Exposure at 22 mW/sec for 3.5 sec and wait for 15 min. 6. Post exposure bake at 120 °C for 120 sec and wait for 15 min. 7. Flood Exposure at 22 mW/sec for 13 sec and wait for 15 min. 8. Development using MF319 for 45 sec. 9. Rinse (2x90 sec) and dry. 10. Hard Bake at 110 °C for 30-40 min.	For patterning of bimetallic mask layer to define of actuation chambers and air vent channels.
4	**Wet Metal Etch**	1. Descum for (2x2 min) at Nanoplus. 2. Etch Au layer using commercial gold etchant (Transene TFA) for 40 sec. 3. Rinse 3 cycles at baker, dry and inspect. 4. Descum for (2x2 min) at Nanoplus. 5. Etch Cr using commercial Transene Chromium Etchants 1020 for 50 sec. 6. Immerse wafer in 2% H_2SO_4 solution (7000 ml H_2O + 150 ml H_2SO_4) for 15 sec to clean residues off. 7. Rinse 3 cycles at baker and dry and inspect.	Depending on the inspections, the etch steps can be repeated for appropriate durations.
5	**Wet Glass Etch**	1. Etch glass for 1 min in HF solution (49%) while stirring at 300 rpm on a hotplate. 2. Rinse and dry. 3. Strip sacrificial photoresist in PRS2000 Stripper (2x15 min) at 80 °C.	1 min to achieve a recess depth of approximately 8 µm.

6	**Wet Metal Etch**	1. Completely remove Au layer using commercial gold etchant (Transene TFA) 2. Rinse 3 cycles at baker, dry and inspect. 3. Completely etch Cr using commercial Transene Chromium Etchants 1020. 4. Rinse 3 cycles at baker, dry and inspect. 5. Immerse in BHF (1:7) for 3 min to smooth sharp edges.	The etch duration can be extended to completely remove bimetallic layer.
7	**PECVD Oxide Deposition**	1. Deposit 0.2 μm-thick SiO_2 layer onto wafer.	It facilitates plasma bonding.
8	**Bottom Electrode Metallization**	1. Dehydration at 110 °C for 20 min. 2. Ti sputtering (Bestec) at 300 W (Thickness: 20 nm). 3. Au sputtering (Bestec) at 300 W (Thickness: 200 nm).	
9	**Photolithography** Mask: Bottom Electrode	1. Dehydration at 110 °C for 20 min. 2. Spin coat HMDS at 500 rpm for 15 sec, and at 3000 rpm for 40 sec. 3. Spin coat SPR 220-3 at 500 rpm for 15 sec, and at 3000 rpm for 40 sec. 4. Soft bake at 115 °C for 3 min. 5. Edge Bead Removal at 2000 rpm. 6. Exposure at 22 mW/sec for 30 sec. 7. Development using MF24-A for 70 sec. 8. Rinse (2x90 sec) and dry. 9. Hard Bake at 120 °C for 30 min.	For patterning of bimetallic mask layer to define of bottom electrodes, pads and connection wires.
10	**Wet Metal Etch**	1. Descum for (2x2 min) at Nanoplus. 2. Etch Au layer using commercial gold etchant (Transene TFA) for 30 sec. 3. Rinse 3 cycles at baker, dry and inspect. 4. Etch Ti layer by immersing the wafer in $HF:H_2O_2:H_2O$ (1:1:200) mixture for 35 sec. 5. Rinse 3 cycles at baker and dry and inspect. 6. Strip sacrificial photoresist in acetone.	Depending on the inspections, the etch steps can be repeated for appropriate durations.
11	**Parylene Deposition**	1. Coat 1 μm-thick parylene-C layer (2 g) with Silane A-174 for electrical insulation	For stiction prevention.
12	**Photolithography** Mask: Actuation Chambers and Air Vents	1. Inspect with Dektak surface profilometer to measure recess depth. 2. Dehydration at 90 °C for 10 min. 3. Spin coat HMDS at 500 rpm for 15 sec, and at 3500 rpm for 40 sec. 4. Spin coat SPR 220-7 at 500 rpm for 15 sec, and at 3500 rpm for 40 sec (for ~7 μm). 5. Soft bake at 115 °C for 3 min. 6. Edge Bead Removal at 2000 rpm. 7. Exposure at 22 mW/sec for 30 sec. 8. Development using MF24-A for 60 sec. 9. Rinse (2x90 sec) and dry. 10. Hard Bake at 90 °C for 8 hours.	Filling of the actuation chambers and air vents with sacrificial photoresist.

13	**Parylene Deposition**	1. Coat 2.5 µm-thick parylene-C layer (5 g) without Silane A-174.	Diaphragm definition.
14	**Top Electrode Metallization**	1. Dehydration at 110 °C for 20 min. 2. Ti sputtering (Bestec) at 300 W (Thickness: 20 nm). 3. Au sputtering (Bestec) at 100 W (Thickness: 200 nm).	
15	**Photolithography** Mask: Top Electrode	1. Dehydration at 90 °C for 10 min. 2. Spin coat HMDS at 500 rpm for 7 sec, and at 2000 rpm for 30 sec. 3. Spin coat SPR 220-3 at 500 rpm for 7 sec, and at 2000 rpm for 30 sec. 4. Soft bake at 115 °C for 2.30 min. 5. Edge Bead Removal at 2000 rpm! 6. Exposure at 22 mW/sec for 5 sec. 7. Development using MF24-A for 35 sec. 8. Rinse (2x90 sec) and dry. 9. Hard Bake at 90 °C for 30-40 min.	For patterning of bimetallic mask layer to define of top electrodes, pads and connection wires.
16	**Wet Metal Etching**	1. Descum for (2x2 min) at Nanoplus. 2. Etch Au layer using commercial gold etchant (Transene TFA) for 30 sec. 3. Rinse 3 cycles at baker, dry and inspect. 4. Etch Ti layer by immersing the wafer in $HF:H_2O_2:H_2O$ (1:1:200) mixture for 35 sec. 5. Rinse 3 cycles at baker and dry and inspect. 6. Strip sacrificial photoresist in acetone.	Depending on the inspections, the etch steps can be repeated for appropriate durations.
17	**Parylene Deposition**	1. Coat 1 µm-thick parylene-C layer (2 g) without Silane A-174.	Electrolysis prevention.
18	**Photolithography** Mask: Parylene RIE	1. Dehydration at 90 °C for 20 min. 2. Spin coat HMDS at 500 rpm for 10 sec, and at 2800 rpm for 30 sec. 3. Spin coat AZ® 40 XT at 500 rpm for 10 sec, and at 2800 rpm for 30 sec (for ~20 µm). 4. Wait horizontally for 2 hours. 5. Soft-bake at 126 °C for 2+2+2+2+7 min, initially in air, vertical teflon, horizontal teflon, tweezer for each 2 min, and continue with soft-bake on hot plate for 7 min. 6. Exposure at 22 mW/sec for 21 sec. 7. Post exposure bake at 105°C for 1.30 min. 8. Development using AZ 826-MIF for 2 min. 9. Rinse (2x90 sec) and dry.	For masking of diaphragms, microchannel, and wire locations during parylene RIE.
19	**Parylene RIE**	1. Etch 4.5 µm-thick parylene-C under O2 and CF4 flow for 45 min (3x15 min). 2. Prepare diluted Aqua regia solution at a ratio of 3:1:6 ($HCI:HNO_3:H_2O$). A short treatment of 7-8 sec is appropriate for removing gold particles residing on wafer surface after parylene RIE.	

20	**Dicing and PR Strip**	1. Coat S1813 for protect structures during dicing. 2. Dicing 3. Immerse dies in acetone for 10 min. 4. Immerse dies in IPA for another 10 min. 5. Leave dies to dry by exposure to the air.	The diaphragms will be released after completing plasma bonding.
Mold Wafer and PDMS Microchannel Fabrication			
1	**Substrate – Silicon**	Size: 150mm (6“) Thickness: 525µm +/- 25µm	
2	**Photolithography** Mask: Microchannel	1. Dehydration at 110 °C for 20 min. 2. Spin coat HMDS at 500 rpm for 10 sec, and at 1200 rpm for 30 sec. 3. Spin coat AZ® 40 XT at 500 rpm for 10 sec, and at 1200 rpm for 30 sec (for ~50 µm). 4. Wait horizontally for 2 hours. 5. Soft-bake at 126 °C for 2+2+2+2+7 min, initially in air, vertical teflon, horizontal teflon, tweezer for each 2 min. Then, continue with soft-bake on hot plate for 7 min. 6. Exposure at 22 mW/sec for 32 sec. 7. Post exposure bake at 105°C for 1.30 min. 8. Development using AZ 826-MIF for 3 min. 9. Rinse (2x90 sec) and dry.	Fabrication of silicon master for soft-lithography.
3	**PDMS Soft-Lithography**	1. Silanize the mold by keeping in a desiccator together with a few drops of PFOTS for a couple of hours (for easy peeling of PDMS). 2. Mix 10 unit of PDMS prepolymer with 1 unit of curing agent. 3. The mixture is degassed in a desiccator, 4. Pour the mixture on the silicon mold, 5. Cure PDMS at room temperature. 6. The individual devices are cut by a razor blade, and inlet/outlet ports are opened using a biopsy punch.	Curing is done at room temperature to prevent shrinkage of PDMS.
Integration of Microchannel and Electrostatically-Driven Diaphragm			
1	**PDMS/Glass Bonding**	1. Expose bonding surfaces to oxygen plasma at 100 W for 90 sec. 2. Align under microscope after adding a drop of water between the glass and PDMS. 3. Leave bonded device on a hot plate at 80 °C until water fully evaporates.	
2	**Release of Diaphragms**	1. Immerse device in acetone and wait for 2 days. 2. Immerse device in IPA and wait for 1 day. 3. Leave bonded device to dry by exposure to the air.	